A 3D Framework for the Musculoskeletal Segmentation of Magnetic Resonance Images

By

Seyed Mehdi Moghadas Tabatabaei Zavareh

A THESIS SUBMITTED IN PARTIAL FULFILLMENT OF

THE REQUIREMENTS FOR THE DEGREE OF

MASTER OF ELECTRICAL AND COMPUTER ENGINEERING

In

School of Electrical Engineering and Computer Science

Faculty of Engineering

UNIVERSITY OF OTTAWA

uOttawa

March 2015

Publication based on this thesis

Seyed Mehdi Moghadas, Won-Sook Lee, “A 3D segmentation framework for an accurateextraction of the spongy and cortical bones from the MRI data”, IEEE international conference in bioinformatics and biomedicine, BIBM 2013.

Acknowledgement

I would like to express my sincere and deep appreciation and thanks to my supervisor professor WonSook Lee for giving this opportunity to me to work with her as a graduate student and mentoring me through the ups and downs of this research project. I would also like to thank Dr. Kawan Rakhra from the Ottawa General Hospital for giving me valuable medical information and advises that could truly help me for finishing this work.

Table of Contents

List of Figures

List of tables

Abstract

In this thesis a new framework is proposed for obtaining the spongy bone, cortical bone, muscle and adipose tissue from MRI data. The method focuses on the accurate extraction of the edges of the target tissues, which is the main drawback of previous works. In this framework six new methods, as listed in section 1.3, are utilized together for improving the result of the segmentation by detecting the relational position of the tissues, acquiring the best possible contribution from the operator in terms of time and efficiency, forward and backward transfer of the segmented tissues at the seed slice and using the newly proposed Deformable Kernel Fuzzy-C Mean (DKFCM) method for improving the result of segmentation on the edges. This method first limits the searching area for the voxels of the target tissue from the whole data to a small strip around the edges of the target tissue. Then, it applies a very accurate segmentation on the searching area, using a deformable kernel, which is capable of adapting itself with the shape of the edge. Comparing the results of this work with some popular MRI segmentation methods like active contour, watershed, FCM and also some heuristic methods, which are proposed in literature for segmenting the MRI to four tissues, demonstrates the superiority of the proposed method especially on the edges.

Keywords—MRI; Segmentation; Fuzzy C-Means; Spongy bone; Cortical bone;

CHAPTER 1

Introduction

1.1 . Motivation and Purposes

Magnetic resonance imaging (MRI) is currently a useful method for exploring body's organs [152]. MRI gives us a 3D image of the body's internal organs, which can be used for 3D modeling of the organs after segmentation. 3D modeling of organs has various applications like surgery assistance [141], simulating the surgery [153], designing the implants [154], diagnosing the cartilage degradation [133, 137] and diagnosing the musculoskeletal disorders [128], like the Femoroacetabular impingement (FAI), in a specific patient.

There are several problems associated with MRI: Intensity inhomogeneity (IIH) [4] can result in same tissues with different intensity levels even in one slice. Partial volume effect (PVE) [156] affects the characteristics of one pixel by more than one tissue types. High volume of noise can eliminates the visible edge between different tissues. As a result of these problems, segmenting the MRI data and extracting the target tissue is the most challenging step for exploiting the MRI data, in order to model body's internal organs. So, robustness against the noise, correct detection of the tissues and accurate segmentation of the edges of each tissue are the most challenging tasks for any MRI segmentation method. So far, some different methods have been developed for segmenting the MRI data. Deformable models [132, 149], active contours [21 - 24], graph cut [139], watershed [26 - 34] and Fuzzy C-Means (FCM) [131, 140, 147&145] are some of the most popular ones. However, it seems that none of them is capable of accurate segmentation of the tissues especially on the edges, which is very important in using the acquired models from the segmentation in various medical purposes. As an example, in diagnosing the Femoroacetabular impingement by modeling, it is very important to have accurate segmentation on the edges of the

femur and acetabulum because the purpose of the modeling is pinpointing the area that causes the impingement, which is usually a small area at the femur and acetabulum meeting point.

In the case of designing medical implants, it is also very important to have an accurate segmentation as well in order to design the implant based on the specific shape of each patient's internal organs, which could be slightly different from the others.

So, one of the goals of this thesis is improving the quality of the segmentation of MRI, especially on the edges, compare to the available methods, in order to make it more reliable for some applications that needs an accurate modeling of body's organs.

Moreover, because of the high quantity of noise and intensity inhomogeneity (IIH) on the MRI data, the participation of a skilled operator could be very helpful in the segmentation process and this is the reason that the quality of the semi-automatic segmentation methods is usually higher than the automatic ones but since the MRI data is a 3D data, which usually consists of multiple slices for a region of the body, the participation from the operator is usually very time consuming because this participation has to be done on each slice individually. So, the other motivation of this work is decreasing the participation time by the operator and increase the efficiency of it as much as possible. Therefore backward and forward transfer of the segmentation at the seed slice is proposed in chapter four.

Finally, the majority of the research efforts on MRI segmentation are done on brain MRIs. Between those which are targeting the other areas of the body, most of them are designed for extracting the bone and there are only few methods which are capable of segmenting the MRI to the cortical bone, spongy bone, muscle and the adipose tissue. While in some applications like simulating the surgery for a specific patient, it is very important to have a complete model of the patient's body in order to have an accurate anticipation from the possible obstacles and problems during the surgery. So, another goal of this thesis is having an accurate segmentation to 4 tissues (cortical bone, spongy bone, muscle and the adipose tissue) at the same time.

To address the problem of musculoskeletal segmentation, H. Kang et al. [129] proposed a framework for considering expert knowledge about the placement of different tissues in

segmenting the MRI of thigh to muscle, adipose tissue, spongy bone and cortical bone. Implementing this method and testing it with our dataset in Chapter 5 for extracting the cortical and spongy bones showed that although this method could correct many of the missegmented parts in comparison with the segmentation by the FCM but the results still contain some misclassified parts of the other tissues and the result of the segmentation on the edges is not accurate. In another effort for the musculoskeletal segmentation of the MRI Benjamin Gilles et al. [132] made use of simplex meshes discrete model. This method doesn't have the misclassification problem on the main body of the tissues but it is still not accurate on the edges and it can't separate the cortical bone from the spongy bone.

FCM was proposed by J. C. Bezdek [115], as a clustering method and proves to be efficient in image segmentation. The main drawback of this method is that it only considers the intensity of the pixels for clustering them. To address this deficiency, some methods [130, 131, 148] added the spatial information to the objective function of the FCM. So, the cluster of each pixel is decided based on the main pixel and the neighboring pixels around it. This extension of FCM, which is known as spatial FCM or SFCM improves the robustness of the FCM against the noise. However, it doesn't improve the segmentation results on the edges of the tissues. The other problem is the misclassification of some parts on the main body of one tissue as another tissue because of the intensity overlapping between the tissues. To overcome the above-mentioned problems in this thesis, we propose a framework that limits the segmentation area from the whole slice to a strip around the contour of the specific tissue. As a result, most of the unwanted pixels which have intensity overlap with the pixels of the target tissue are omitted. For increasing the segmentation accuracy on the edges of target tissues, we propose the DKFCM method. In this method by deforming a 3 dimensional kernel around the main pixel, which shows the neighboring pixels, in an iterative mode the quality of the segmentation on the edges is improved.

Considering the relative position of the tissues in respect to each other is another useful method which is proposed for increasing the robustness of the method against the noise and Intensity inhomogeneity.

1.2. Structure of the Thesis

The thesis is organized in 6 chapters. In Chapter 2, we present some general information about the MR imaging, the physiology of the hip and some problems that can be solved by segmenting and modeling MRI data. In Chapter 3, the available segmentation methods, which are commonly used for segmenting MRI data, are explained. In Chapter 4, the proposed method is explained. In Chapter 5, the evaluation methods and validation results of the proposed method are presented and finally in Chapter 6, the conclusion is provided and some possible feature research methods are proposed.

1.3. Contributions

Six new contributions are proposed, implemented and evaluated in this thesis as listed

1- Deformable Kernel Fuzzy-C Mean (DKFCM) which is a newly developed method that is proposed in this thesis. This method is specifically designed for improving the segmentation results on the edges.

2- The proposed method for employing the operator in the segmentation process. This method is designed for getting the list time consuming and most useful cooperation from the operator.

3- Forward and backward transfer of the segmented tissues, which takes advantage of the close connection between the tissues in successive MRI slices for restricting the searching region for the target tissue and improving the segmentation result.

4- Relative position detection of the spongy bone

5- Relative position detection of the cortical bone

6- Relative position detection of the adipose tissue

The last three contributions improve the segmentation by detecting the position of the target tissue in respect to the other tissues and using expert knowledge about the place of each tissue.

CHAPTER 2

Background and applications of MRI segmentation

2.1. Magnetic Resonance Imaging (MRI)

Magnetic resonance imaging is a medical imaging method applied in order to obtain images of body structure taking benefit from a combination of radiology, magnetic fields and algorithms. The scanner is constructed from a tube located inside a big round magnet (Figure 2.1). Magnetic resonance imaging was built based on the fact that more than 70% of the human body is composed of water. So, by magnetizing the water molecules of a patient, it is possible to magnetize his body. At the magnetizing process the water molecules first absorb the radio wave energy and then emit it. The emitted radio waves from the patient body can be used for forming a 3D image from the internal organ. Afterwards, a preprocessing and post processing is applied on the image information exploiting various algorithms, such as un-noising, inhomogeneity correction and image segmentation algorithms.

Figure 2.1. MRI device [142]

Figure 2.2 shows the hardware block diagram of the MRI system. In contrast to X-ray imaging, that uses the X-ray frequency range, magnetic resonance imaging needs the absorption and emission of the radio frequency, which makes it a safe imaging method for the human body. [158]

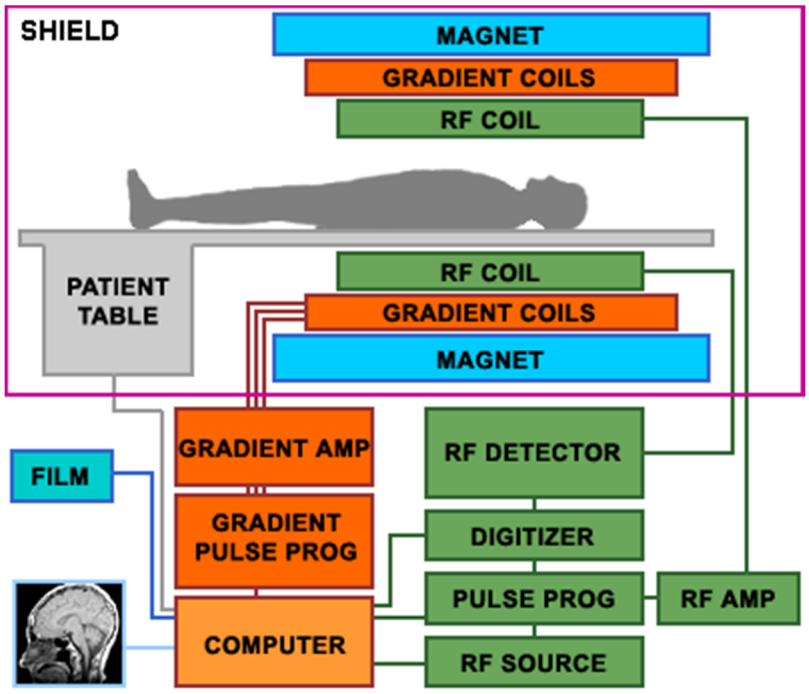

Figure 2.2. Block diagram of the MRI hardware system [1]

2.1.1. Contrast in Magnetic Resonance Images

The water protons in various tissues inside the body have various relaxation times. This difference for two tissues shows itself as the contrast. For example in figure 2.3, which shows a MR image of brain, the contrast between different tissues can be observed.

This contrast can be changed with the change in the water rate in different tissues which can cause a big problem for any type of image segmentation algorithm.

2.1.2. Intensity Change in MRI

Intensity change or intensity inhomogeneity (IIH) is one of the main problems occurring in magnetic resonance imaging. It happens when a smooth intensity change is observed for the same tissue which actually should have the same intensity values.

IIH may be caused by some reasons such as unfixed patient, static field inhomogeneity, radio-frequency problems, metal implants, etc. [2 -4] Some studies for different inhomogeneity correction methods have been performed in literature. [5- 8]
Figure 2.3 shows the inhomogeneity field and the corrected image in the MRI of the brain

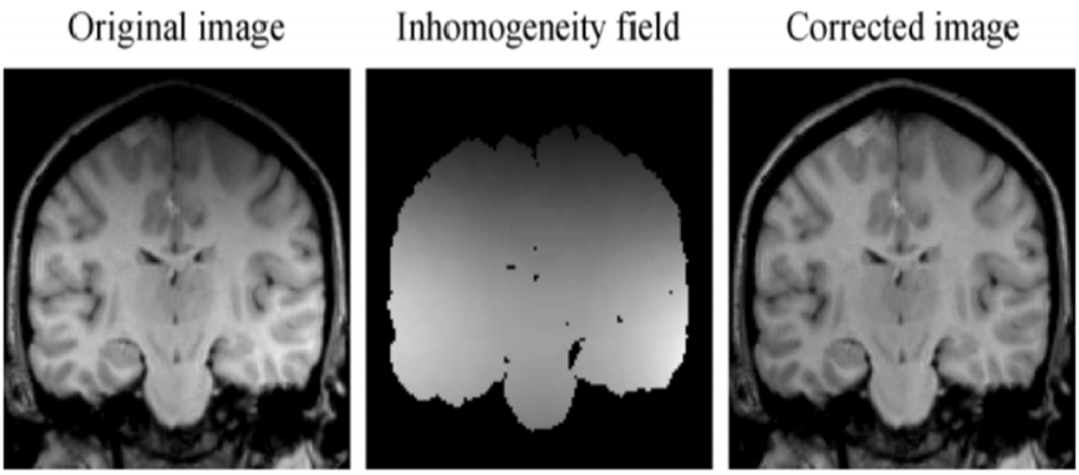

Figure 2.3. Intensity inhomogeneity correction [5]

2.2. Physiology of the Hip

Since the final result of this research is tested on the MRI of the hip, some basic knowledge about the hip is presented in this section in order to familiarize the readers with the physiology of this part of the body. The most vulnerable part of the hip is the hip joint, which can be easily affected by various diseases. Hip joint is the place where femur connects to pelvis. A hip joint consists from these main tissues: [127]

- Ligaments
- Bones
- Muscle
- Cartilage

In addition to these four tissues, there are some other tissues like the adipose tissue, blood vessels and nerves at the hip area. Figure 2.4 shows a horizontal cross section of the hip area.

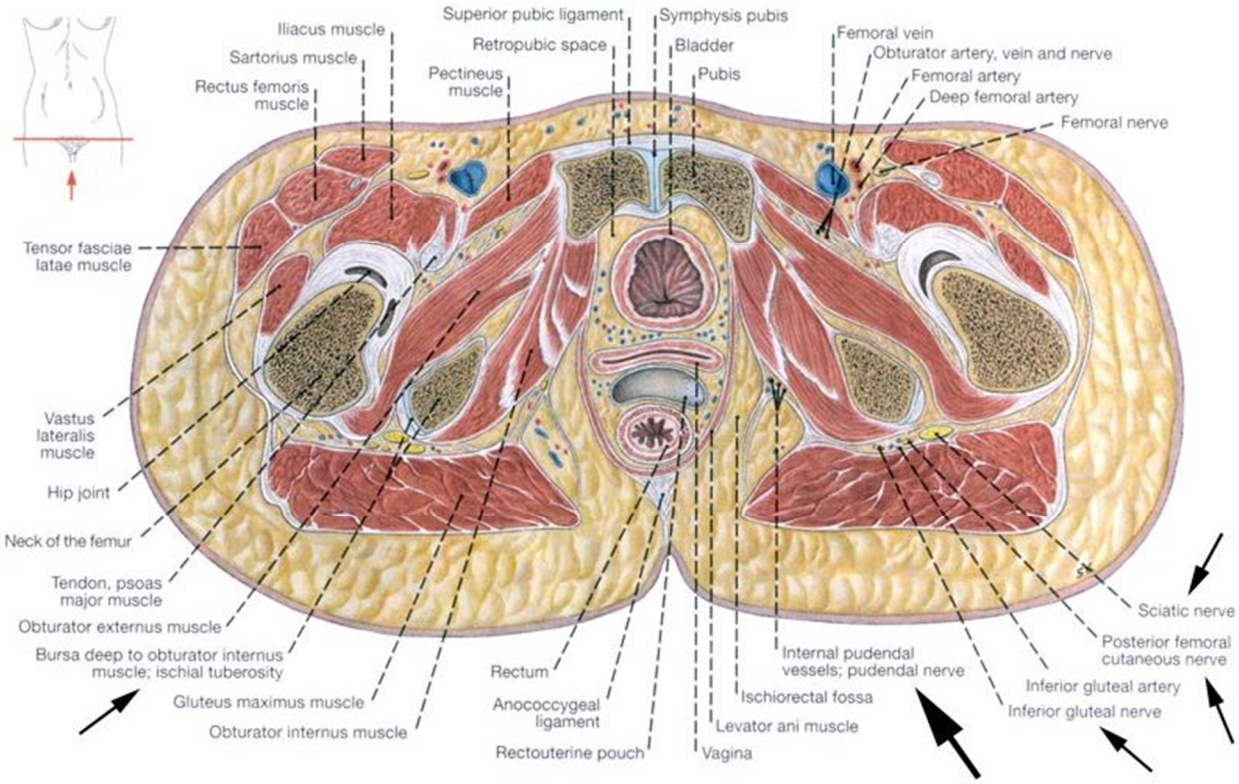

Figure 2.4. Full horizontal cross section of the hip (female) [143]

2.2.1. Hip Ligaments

The arrangement of ligaments that establishes a connection between femur and the pelvis are needed for stability and keeping the hip from going outside from its general position. Figure 2.5 shows the ligaments at the posterior hip area.

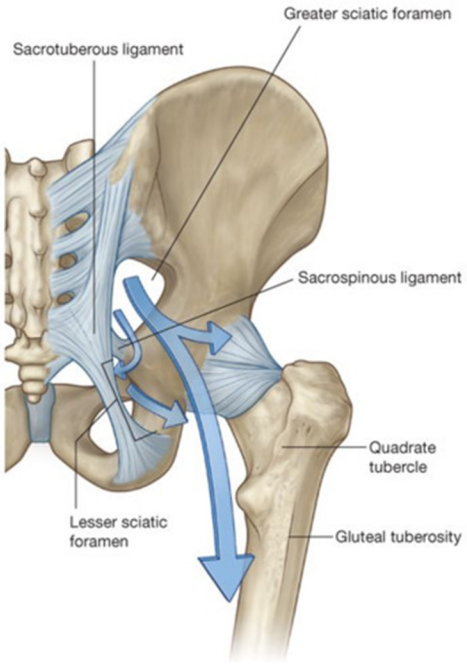

Figure 2.5. Hip ligaments [144]

2.2.2. Hip Bones

Hip joint consists of a ball and also a socket, connecting two bones, the femur with the pelvis. The femur head locates inside the acetabulum, and shapes the hip joint. Due to this, the leg can move simply in every direction. Figure 2.6 shows the hip joint bones.

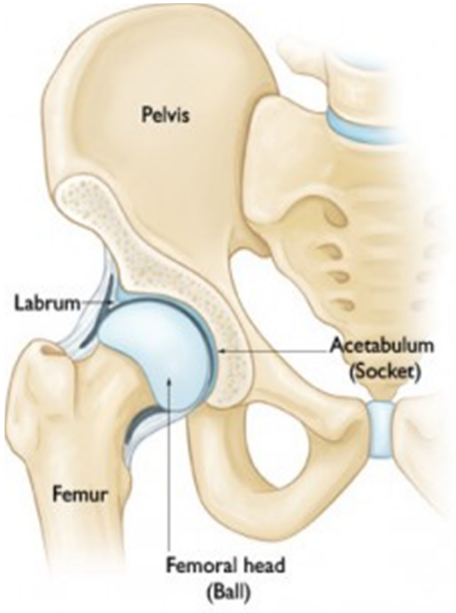

Figure 2.6. Hip joint bones [9]

Every bone inside the body is made of cortical bone and spongy bone tissues. Cortical bone (compact bone) is the hard tissue which wraps the outside of the bone and the spongy bone also called the trabecular or cancellous bone is the softer part that exists inside the bones. Spongy bone is more responsible for absorbing the shocks. [146] Figure 2.7 shows the spongy and cortical bone at the femur head and their microscopic structure.

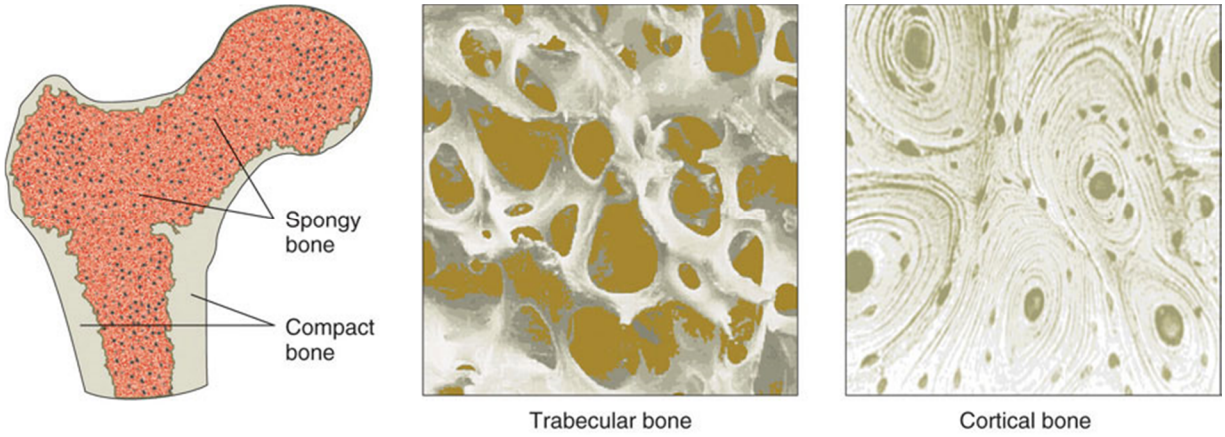

Figure 2.7. Spongy (trabecular) and cortical (compact) bone tissues at the femur head and their different microarchitecture and porosity shown at the microscopic view [146]

2.2.3. Hip Muscles

Hip muscles have two functionalities; fixing the whole lower extremity in time of movements as well as powering the hip joint to move freely in different situations. There are several different muscles at the hip area to enable the hip joint to move in different directions. Figures 2.8 and 2.9 show the deep and superficial hip muscles respectively.

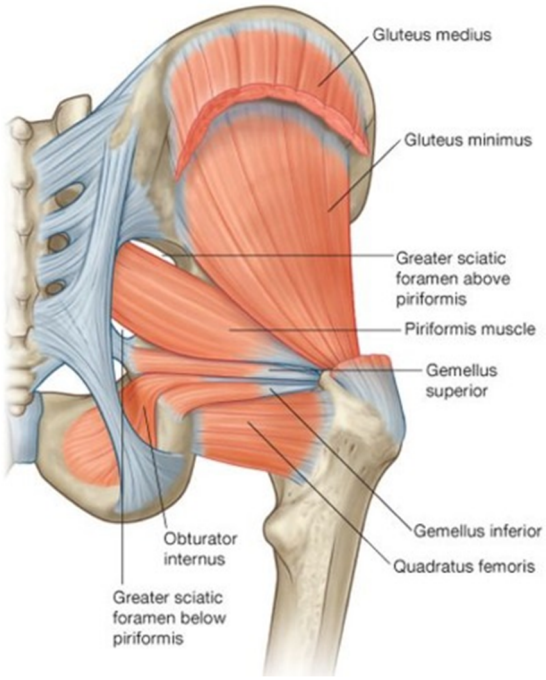

Figure 2.8. Hip muscles (deep view) [144]

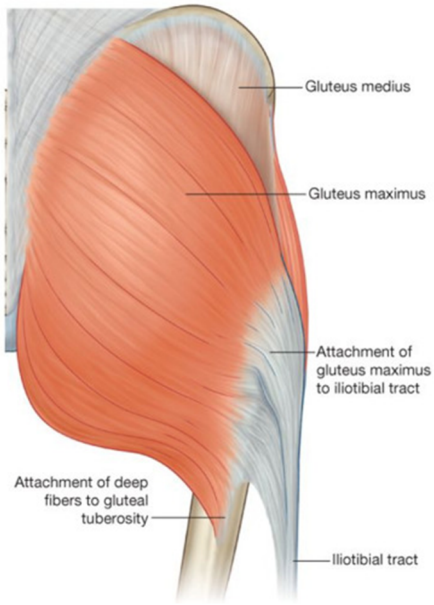

Figure 2.9. Hip muscles (superficial view) [144]

2.2.4. Hip Cartilage

The cartilage acts as a substructure for the bones when performing activities. It lets the joint to turn freely in every direction and therefore supports the bones with low friction. The most

important cartilage at the hip area is located at the femur and acetabulum meeting point. Any damage to this cartilage could result in serious problems in moving the thigh. Figure 2.10 shows a healthy cartilage between the femoral head and acetabulum.

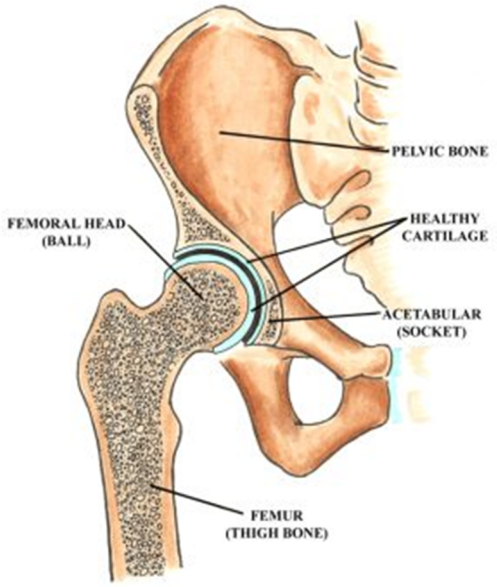

Figure 2.10. Cartilage between the femoral head and acetabulum [138]

2.3 Femur Bone

The upper leg has just one bone named Femur. Femur is the tallest bone inside the human body. This bone connects many muscles and ligaments in the body. Actually, it is acting like an origin point and its principal functionality is transferring the forces from tibia to the hip joint.

Femur is constructed from 3 main areas: [10]

- Proximal
- Shaft
- Distal

The whole femur bone is shown in Figure 2.11.

Since the hip region only covers the proximal area of the femur, this part is explained in detail in the following

.

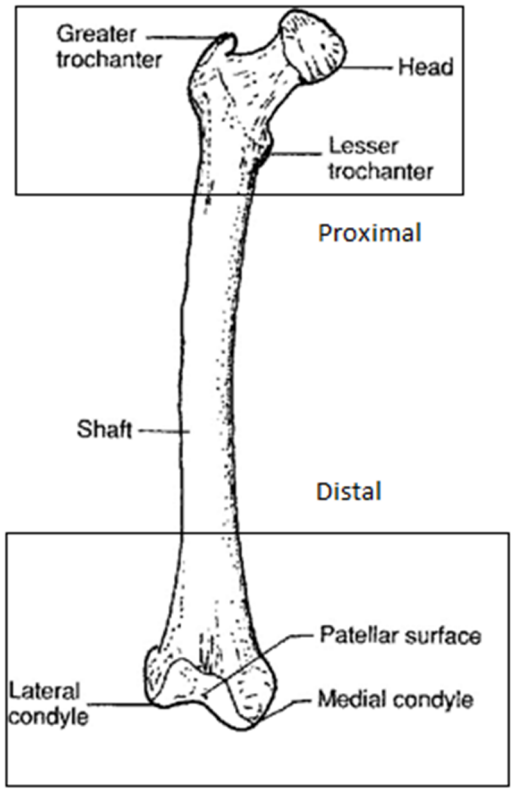

Figure 2.11. Femur [11]

2.3.1 Proximal

As mentioned previously, the Hip joint consists from proximal area of femur together with the pelvis. Proximal consists from three following parts:

- Neck
- Head
- Trochanters

Neck is the cylindrical area which establishes a junction between the shaft and the femur head. It can project in a medial and superior orientation. Due to this wide projection ability, hip joint is able to obtain multi-dimensional movement [150].

The femoral head is shown from the anterior and posterior views in Figures 2.12 and 2.13 respectively. A ligament is connected to the head of femur, where there is a level surface with a concavity on the medial area. Acetabulum articulates with the femur head at the hip joint.

Greater trochanter is a projection of bone starting from the anterior shaft. It is transversal to the connecting point of the neck. It is located on the anterior and posterior sides of the femur and is angled superiorly and posteriorly. The abductor and lateral rotator muscles of the leg are also connected at this place.

Lesser trochanter is located in the lower region of the neck-shaft junction where the Psoas major and Iliacus muscles are connected. This part is tinier than the greater trochanter.

Intertrochanteric line attaches the two trochanters to each other. The Iliofemoral ligament, which is a very strong ligament of the hip joint, is connected in this region. When Intertrochanteric line passes the lesser trochanter on the posterior surface, it is called the pectineal line.

Intertrochanteric crest is a ridge of bone placed on the posterior surface of the femur and analogous to the intertrochanteric line. This is a ridge of bone that attaches the two trochanters together. It is located on the posterior surface of the femur.

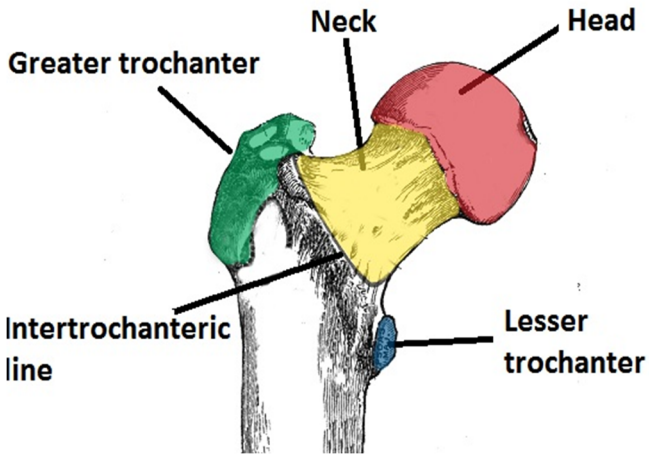

Figure 2.12. Anterior, proximal femur.[12]

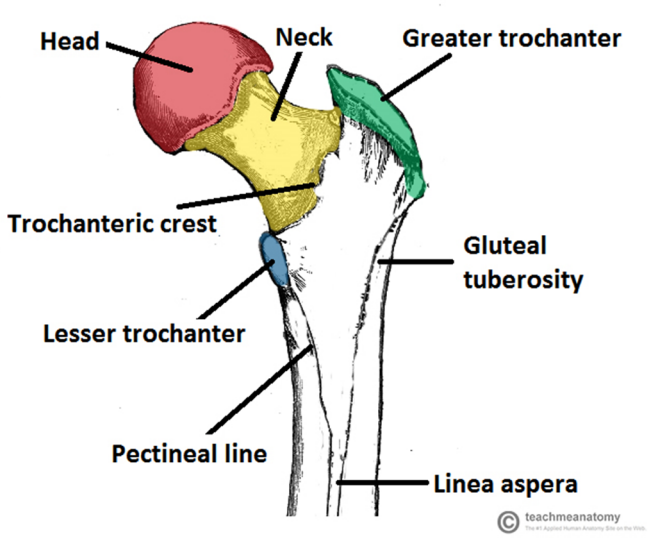

Figure 2.13. Posterior, proximal femur [12]

2.4ImpingementDisease at the Hip Joint

Femoroacetabular impingement (FAI) is a reason for hip pain and dysfunction. The disease was explained in 1990s for the first time. Ganz et al. [13] mentioned iterative abutment of a morphologically abnormal proximal femur and/or acetabulum in hip terminal range-of-motion period as the reason for Femoroacetabular impingement. This will finally result in damage to the labrum and Acetabular cartilage. This damage is also associated to the region where osseous abnormally has happened [13].

The osseous abnormalities reasoning in the FAI are customarily categorized in two types;

- Loss of the normal femoral head-neck offset
- Acetabular over-coverage

The first type causes cam impingement and the second type causes pincer impingement.

Also there is a third type which occurs when the 2 first types are merged together.

2.4.1. Cam Impingement

Cam Impingement is known as the most popular FAI which is usually occurring in young men in ages between 20 and 30 [13 - 18].

In cam Impingement Normal femoral head-neck contour is lost because of an abnormal extension of the proximal femoral epiphysis, short or long femoral neck or residual deformity from femoral neck fracture.

2.4.2. Pincer Impingement

Pincer Impingement is usual in women in ages between 30 and 40 [19, 20]. It causes because of an extra growth in the upper lip of the acetabulum.

The reasons for acetabular over coverage are determined as:

- Relative anterior over coverage (acetabular retroversion)
- Focal over coverage at the anterosuperior acetabular rim
- Global over coverage (coxaprofunda, protrusioacetabuli)

Cam and pincer impingements are both depicted in Figure 2.14. The effected region by each disease is shown in red in this figure.

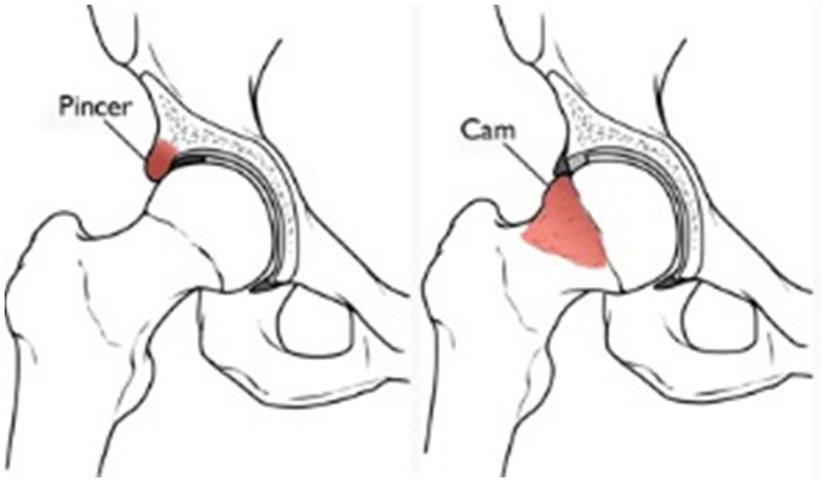

Figure 2.14. Pincer impingement (left)and cam impingement (right) [155]

CHAPTER 3

A Review on Available MRI Segmentation Methods

The applications of Medical image processing have increased in recent years. So far, several methods have been developed and exploited in order to perform Magnetic Resonance Image segmentation. Delicate segmentation of medical images is a very important and hard step because images are mostly suffering from inhomogeneity, noise and some deviations.

In this chapter a review on various image segmentation techniques which are commonly used in MRI segmentation is presented. As these methods also incorporate some drawbacks, some modifications to each approach is also proposed. In some cases a combination of different methods may be used to take advantage of various benefits and reduce the problems with each method.

3.1 Snake

Kass et al. [21] developed the snake method in 1987, which is also called as active contour. This algorithm is popular in image processing and segmentation tasks particularly when it comes to identifying boundaries of the object. [22]

Snakes are splines guided by external forces and influenced by image forces used in order to minimize the energy function by deforming a deformable model to the contour of a target object in a process which will lead to a convergence to the minimum of the energy function of the active contour. [21]

Equation 3.1 shows the parametric curve which represents the classical snake

$$v(s) = (x(s), y(s)) \tag{3.1}$$

where x and y denote the coordinates on the contour and S is a normalized parameter. The equation of the snake's energy can be written as

$$E_{snake} = \int_0^1 [E_{snake}(v(s))]ds \tag{3.2}$$

$$= \int_0^1 [E_{constraints}(v(s)) + E_{image}(v(s)) + E_{internal}(v(s))]ds$$

where $E_{constraints}$ denotes the energy of constraints which enforces the snake to or from the objects. $E_{internal}$ denotes the internal snake energy and E_{image} denotes the energy of image which orients the snake. The energy constraints are obtained from the external constraints and $E_{internal}$ is defined as:

$$E_{internal} = \frac{\beta(s)|v_{ss}(s)|^2 + \alpha(s)|v_s(s)|^2}{2} \tag{3.3}$$

where $v_{ss}(s)$ denotes the bending force and $v_s(s)$ denotes the stretching force. Finally, E_{image} consists from three terms and their weights as the following.

$$E_{image} = E_{edge} W_{edge} + E_{term} W_{term} + E_{line} W_{line} \tag{3.4}$$

where the edge, termination and line energy terms are added. The algorithm is always updating the contour inside the iteration in order to obtain the object boundary with minimal energy.

There are some disadvantages with the classical snake, for example the convergence procedure does not converge to real objects , this problem happens specifically in MRI data , actually the first contour must be not so much far from the final contour . Also, it is hard for classical snakes to progress into boundary concavities[23]. To solve the mentioned drawbacks, C. Xu et al. introduced gradient vector flow (GVF) [24]. The GVF snake is commonly used in

medical image segmentation. However, GVF has also some problems by determining the region of interest properties. Anthony Yezzi et al. [25] introduced a geometric snake model for the medical image segmentation, which works based on defining feature-based metrics for converging faster to the desired feature. Figure 3.1 shows the deformation process in the snake method.

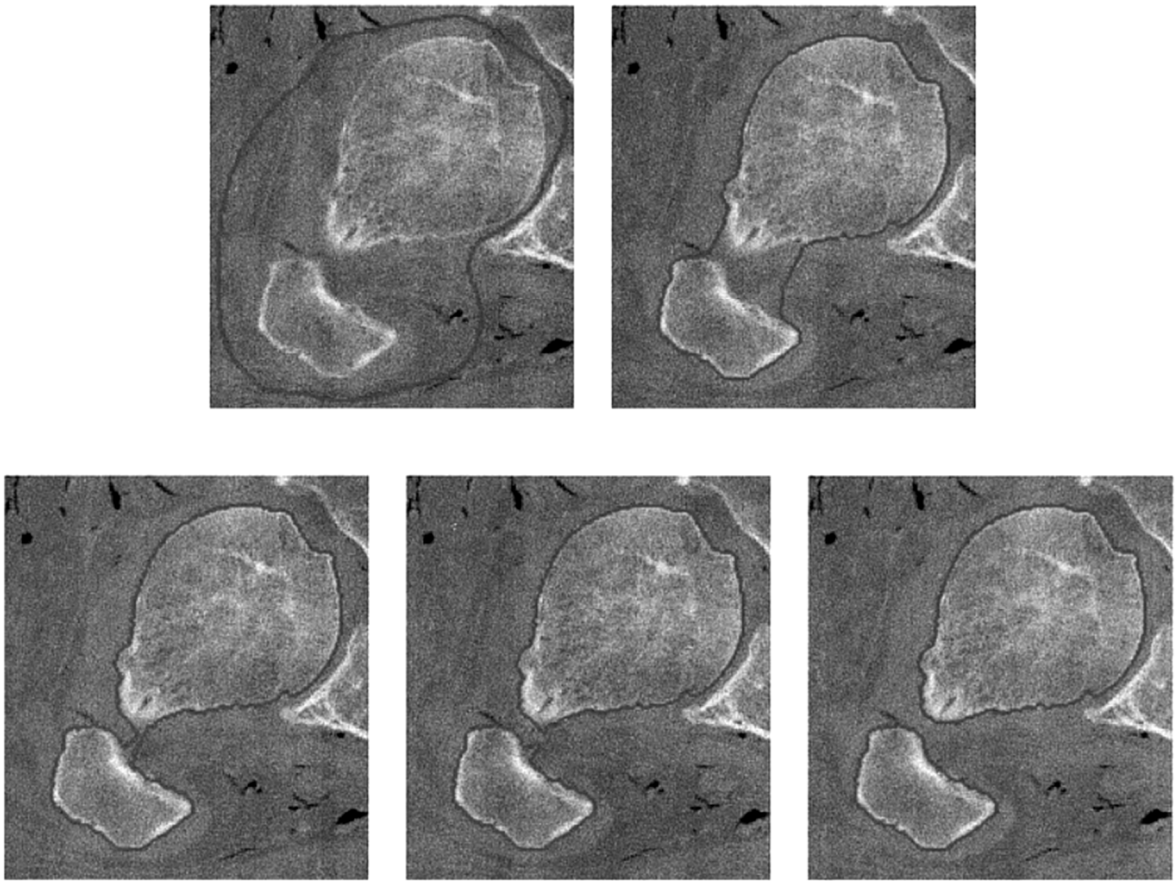

Figure 3.1. Results of applying snake on a CT image [25]

3.2. Watershed Segmentation Method

The watershed transform is a morphological gradient-based segmentation methodology which has opened its way in medical image segmentation. In this method various gradient values denote different heights. Watershed lines are functions of contrast or gradient. [28]

Watershed has been used in various medical applications as a segmentation method. Mancas et al.[26] worked on an iterative watershed method in order to segment tumors existing inside the neck. Also Salman et al. [27] exploited watershed in order to segment tumors in data obtained from the brain.

For performing Watershed transformation, the very first step is the marker delegacy which can be done manually or automatically. Then, the process starts and the topographic surface floods from this step. [28, 29, 30]. Figure 3.2 shows the result of applying the watershed method on the MR image.

As a main drawback, watershed transform is very impressionable to noise, extra-segmentation and impotence in slim structure segmentation [30]. Hence, watershed algorithm is usually integrated with other methods. [31, 32, 33, 34].

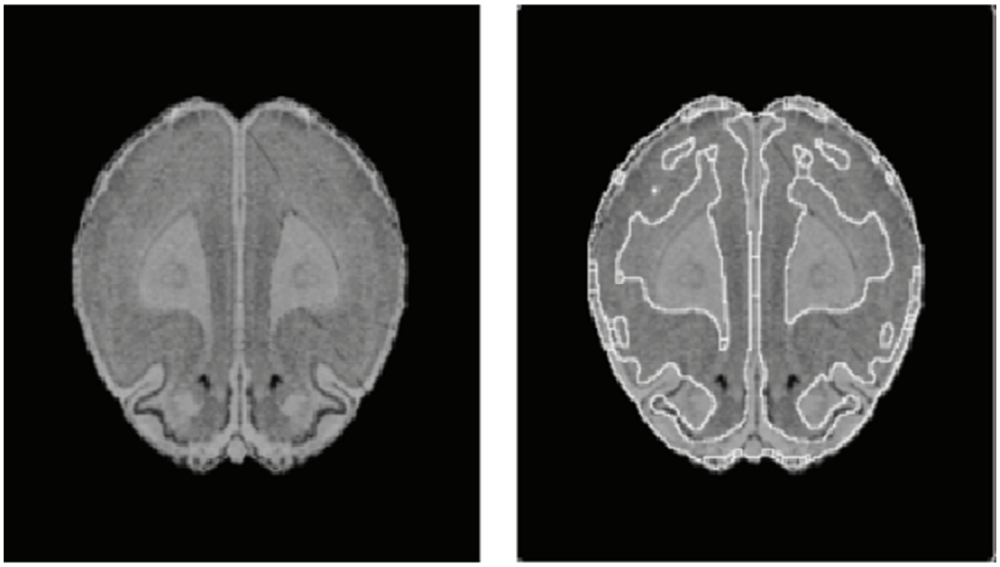

Figure 3.2. Watershed segmentation on MRI image of brain (left: original ,right: segmented)[35]

3.3. Region-Based Image Segmentation Methods

One of the other segmentation techniques is region growing. The very first step in the region growing technique is defining a group of pixels as the seed points. The mentioned group of pixels is always prolonged by a scrutiny procedure, in which the homogeneity status is verified on the neighbors of the current group of pixels. In the case that verification result is positive for the homogeneity status. The neighboring pixels are added to the group. Due to the information which is obtained previously from the application, the thresholds are determined and used in order to determine the updated connectivity relationships. [37]

Figure 3.3 shows the result of applying the region growing on the short axis image.

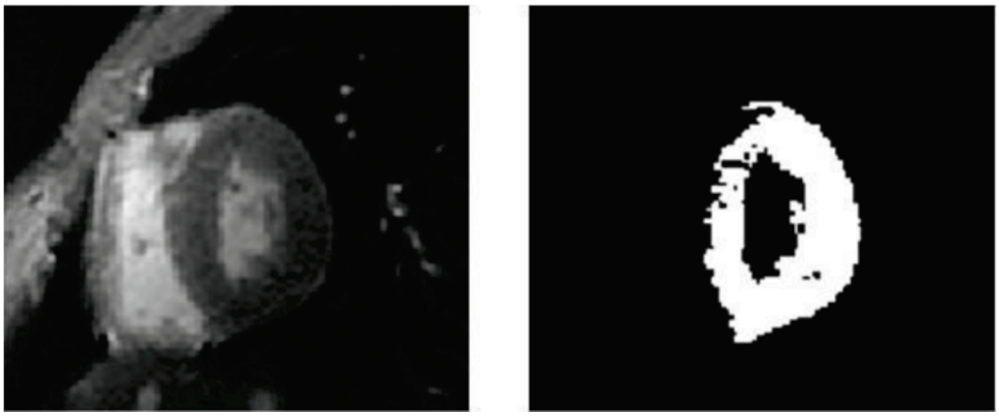

Figure 3.3. Result of region growing(right) on short axis image(left) [36]

The following types of region growing methods have been developed due to the homogeneity measure [37]:

- Isolated Connection
- Confidence Connection
- Connected Threshold
- Neighborhood Connected

Isolated Connected Region Growing (ICRG) has been applied in a large number of medical purposes. Chang et al. exploited ICRG in order to perform colon segmentation [39]. Mešanović et al. took benefit from histogram erosion in order to find thresholds for lung images [38].

Isolated Connected method processes seed points and thresholds to obtain the result. A binary quest is applied to determine the upper threshold.

However, region growing is experiencing some problems with over or under segmentation when facing noisy or blurred images. Hence ICRG is used as a mixture with other methods. Sivaperumal et al. mixed ICRG with Pulse-Coupled Neural Network for obtaining the parameterization [40]. ICRG also was integrated with the watershed and level sets in order to solve the mentioned problems [41, 42]. Extensions have also been applied by occupying Genetic algorithm for choosing the best thresholds [43].

Confidence Connection Region Growing (CCRG)is another iterative method from region based methods, in this method thresholds are updated continuously, for this sake the pixels inside

the Region of interest (ROI) are processed and a standard deviation and mean value of ROI are calculated. Equation 3.5 shows the formula for calculating the lower and upper thresholds

$$lt = m - f\boldsymbol{\sigma} \qquad (3.5)$$

$$up = m + f\boldsymbol{\sigma}$$

whereσdenotes the standard deviation, m denotes the ROI mean and f is a constant.

Another region-based method is the connected threshold region growing (CTRG). This method is the simplest of its kind. In this method, the thresholds are defined clearly then the pixels with a defined intensity value are determined and accumulated inside the ROI.

The other available method is the Neighborhood Connected Region Growing (NCRG). In this method, a shaped neighborhood is calculated for all of the pixels in the target image and then the thresholding requirements are checked on the neighboring pixels to keep the surrounding pixels inside the threshold. The checking procedure determines if a pixel is inside the ROI or not.

3.4. Graph-Cut Segmentation Method

In Graph based image segmentation an image is translated to a graph so pixels conform to vertices and the pixel connections conform to edges. Foreground and background vertices are also specified separately. In this method the weight of the edges explains the analogy of the corresponding pixels of that edge. Graph cut approach is a mixed procedure for image processing. There are two group of edges; n links and t links. N link edge establishes a connection between adjacent pixels and t link edges establish a connection between vertices. This is done in order to sample pixels. All of the edges are stored in an edge set of t links and n links respectively.

Thus we have the following optimization problem:

$$E(L) = \sum_{p \in I} Pr(L_p) + \mu \sum_{p,q \in N} V_{pq}(L_p, L_q) \qquad (3.6)$$

where P_r is the penalty of equalizing of L_p to pixel p,L_p is the label for pixel p, L is the labels set and $V_{pq}$is a measure for penalty of equalizing two adjacent pixels to apparent labels.

Min-cut/max-flow is a well-known problem in the optimization theory, several solutions have been proposed for this problem, like the linear programming [44], Orlin's methods [45], push-relabel [46] and augmenting path [47] are some of different proposed solutions in papers. The difference between these methods is in their different computational efforts. Boykov and Jolly [48] have proposed the augmenting path method as a solution. The algorithm has been applied to brain images [49, 50] and also to cardiac images [51]. However, it is not suitable for smooth edges. For solving this problem, Veksler exploited a common star shape for convex cases. He did this by adding a shape term to the energy function [52]. Slabaugh et al. proposed a method for segmenting the vessels with an elliptical solution [53]. Das et al. proposed a method based on realizing a compact shape in the energy function. This method was tested for extracting the eye from MRI data [54]. Zhang et al. combined the graph cut segmentation method with a random template method and also changed the energy function, however in their method the existent shape is already registered [55] Grosgeorgea et al. proposed a method for modeling the shape alterations. This method is tested on the cardiac MR data [56]. Result of applying the graph cut method on a brain MRI is shown in Figure 3.4.

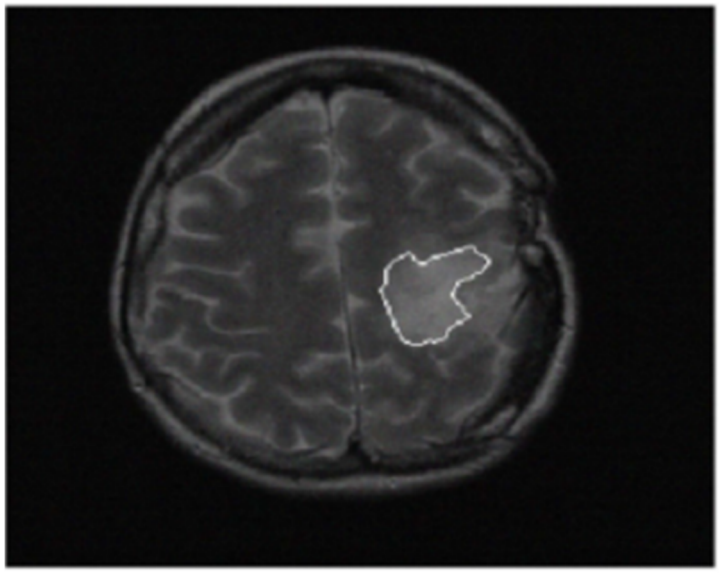

Figure 3.4. Graph cut applied on a brain MRI image[57]

3.5 Intensity Based Thresholding for Separating Different Tissues

One of the other fundamental segmentation methods is Thresholding, in this method some intensity thresholds are defined for the image. These thresholds make different classes for different intensity ranges,

Equation 3.7 shows a thresholding with only one threshold.

$$\begin{aligned} &if\ I(k) < c_0 \qquad then\ T(k) = 0 \\ &if\ I(k) > c_0 \qquad then\ \ T(k) = 1 \end{aligned} \tag{3.7}$$

where c_0 is the threshold value that is depended to the image histogram and T() expresses our threshold image . In this case the pixels are divided in two types called foreground and background pixels.

We may also use different thresholds. This is known as multi-thresholding method, which is shown in equation (3.8).

$$\begin{aligned} &if\ I(k) \le c_0 \qquad then\ T(k) = t_0 \\ &if\ c_0 < I(k) \le c_1 \qquad then\ \ T(k) = \ t_1 \\ &\quad . \\ &\quad . \\ &\quad . \\ &if\ c_{n-1} < I(k) \quad then\ T(k) = t_n \end{aligned} \tag{3.8}$$

Multi-thresholding method is appropriate for the data with high inter-class contrast and coherent intra-class pixels. It is possible to increase thresholding performance with local approaches. In this method the thresholds are identified due to statistical characteristics in particular spots. In the dynamic thresholding restraints are adjusted as functions of pixel attributes or functions of spatial position [58, 59].dynamic thresholding is also called adaptive

thresholding method in some references. Dynamic thresholding works fine for MR image segmentation [60, 61 & 62]. However, the process has a high processing complexity and it is sometimes hard to find the desired correct function for the whole image. Figure 3.5 shows the result of applying thresholding segmentation on brain lesion image.

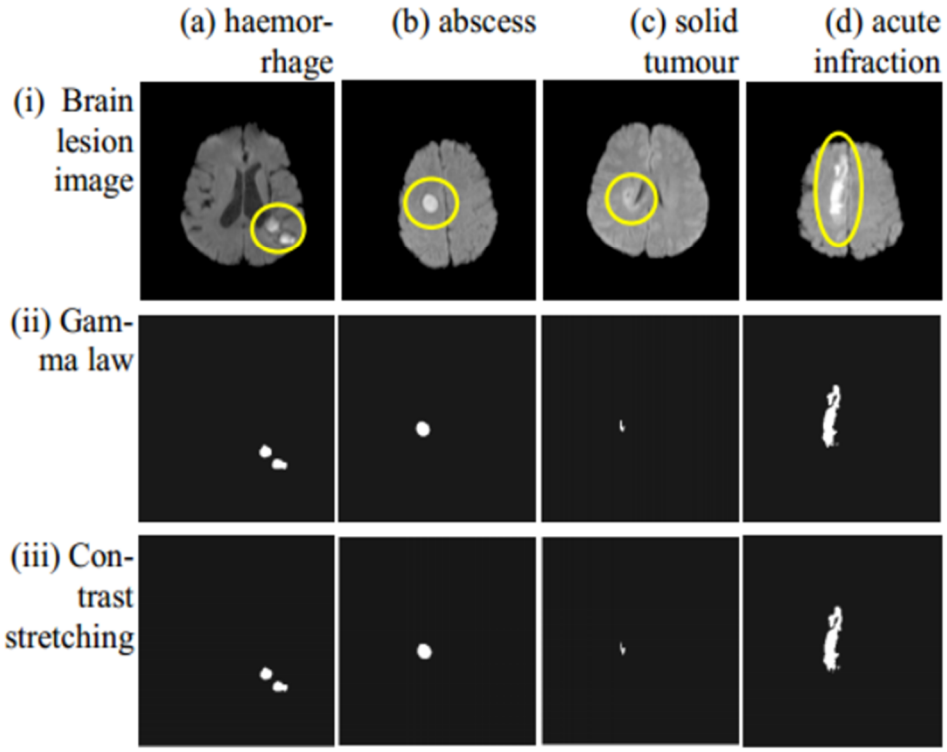

Figure 3.5. Thresholding method on brain lesion [63]

As a drawback thresholding method is not suitable when we are facing noisy images. Moreover it is hard to find appropriate threshold rates for this method. As a solution to this problem N. Ostu has presented a procedure to find the appropriate threshold rates[64]. In order to obtain ideal threshold, intra-class variance should be reduced to its minimal value in this method. Kalavathi exploited Ostu thresholding in order to segment brain images [65]. However, the procedure has some disadvantages; it is time demanding, moreover it cannot process noisy data.

3.6.Model-Based Segmentation

Deformable models are categorized into parametric models [66, 67] and geometric models also known as level set approach [68, 69, 71]. A complete study of the model–based segmentation is covered in [70]. In both methods a dynamic model is developed, but geometric models are implicit and parametric models are explicit.

Evolution equation for the geometric model is:

$$\emptyset_t + F|\nabla\emptyset| = 0 \tag{3.9}$$

where, F is the speed function, which could control the speed of motion.

Different variations of the geometric models have been proposed for segmenting different body's organs in literature.Liver,[72, 73] cardiac [74, 75 and 76] and brain [77, 78, 79 and 80] are some of the examples. The main drawbacks of this method are the high calculation complexity and low segmentation accuracy on the surface.

On the other hand in the parametric deformable models (PDM) approach, a Lagrangian energy function, which is shown in equation 3.10, should be minimized.

$$E(M) = \int E_{int}\big(M(S)\big) + \int E_{ext}(M(S)) \tag{3.10}$$

where, M(s) is the parametric model and E_{int} and E_{ext} are the internal and external energies respectively. For segmentation of high dimensional data, parametric model is preferred to geometric model becauseit is more flexible and adjustable to be adjusted to higher dimensional data. However, parametric deformable model also has some drawbacks like the under-segmentation in the plain areas of the image and high dependency on the location of the initial model, which has to be adjusted very close to the contour of the region of interest. So far, several scientists have exploited deformable models in different medical image segmentation applications[81- 87, 149].Jerome Schmid et al. [160] used this method for the MRI bone segmenting. Figure 3.6 shows the result of applying a model-based segmentation on 2D slices.

Although the model-based methods can extract a delicate organ from MRI data because they begin from a generic model but the final segmentation result is not accurate enough. Because of this drawback it is not possible to use this method for the applications, which need an accurate segmentation on the edges of the target organ.

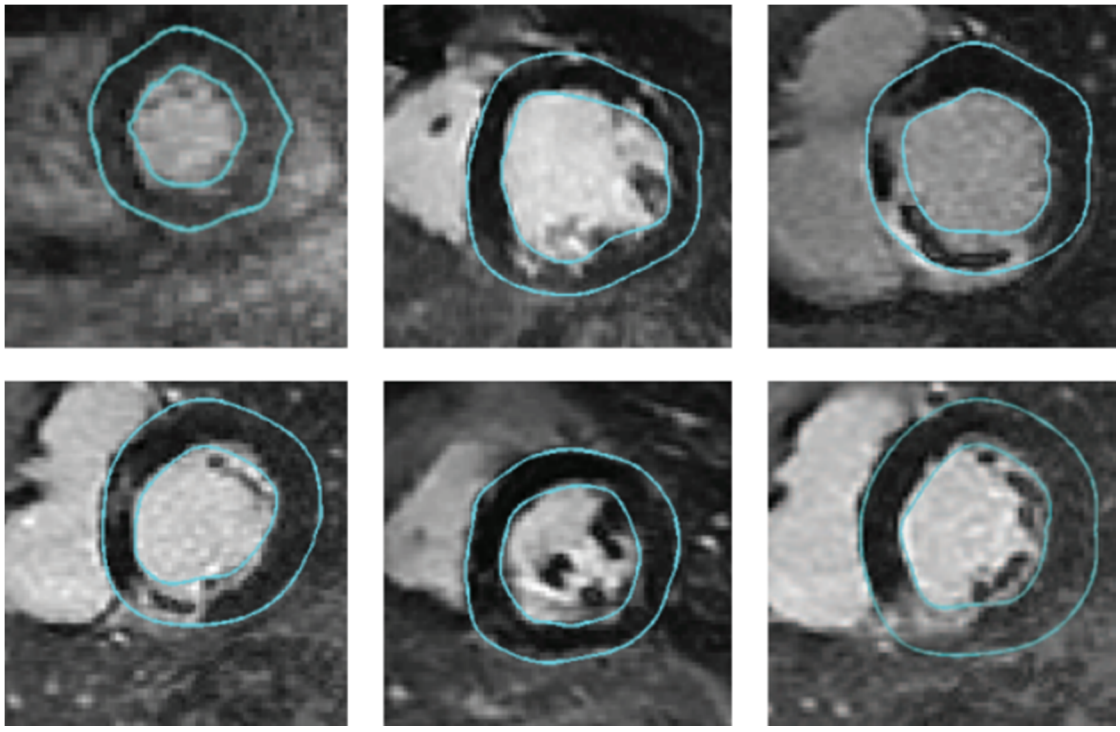

Figure 3.6. Deformable segmentation results on 2D slices. The external line shows the position of the initial model and the internal line shows the result of deformation [88]

3.7.Atlas-Based Segmentation

Atlases are some statistical models containing geometrical and intensity information. As an example Active Appearance Models (AAM) [89] and Active Shape Models (ASM) [90] are two atlases.

A large variation of atlas based image segmentation approaches is available, but a limited number is suitable for medical applications due to the fact that there is a larger variation of anatomies. Atlas-based methods are suitable for conditions where we have not access to adequate intensity information, Hence we can make use of the initial data stored inside atlases. Various atlas-based solutions have been proposed for depiction of images from various organs, works have been done for cardiac data in [91, 92] as well as the breast data in [93, 94] and the brain data in [95-97].

In order to perform Atlas-based MR image segmentation an Atlas should be implemented firstly. For this purpose several solutions exist [98-101]. Afterwards, the image registration is

performed. This process can be done with different possible techniques and determines the segmentation accuracy [102].

In Each image registration method, the following items exist:

- An objective function for comparison
- Optimization procedure
- A mapping between spaces

The above algorithms are discussed in [103 & 104]. The result of atlas-based segmentation is shown in Figure 3.7.

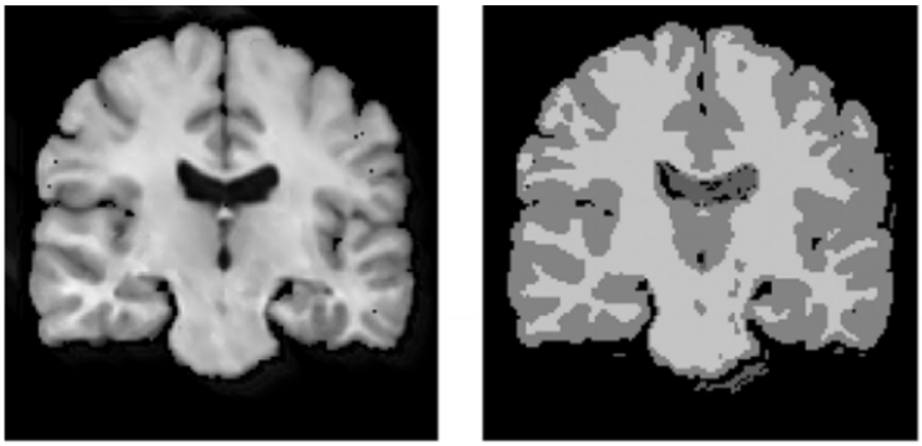

Figure 3.7. Atlas-based segmentation (right) on MRI image (left) [105]

3.8. k-mean and Fuzzy C-mean (FCM)

Clustering methods are a group of unsupervised classifiers which classifies the feature space. Due to this classification, different image areas lie in different classes. Clustering methods are from the common methods used for segmenting MR images [106-108]. Various methods have been proposed so far, two of the most famous ones are [109-112]:

- *K-mean* (kM)
- fuzzy *c*-means (FCM)

K-mean algorithm is one of the famous methods used for MR image segmentation, in which hard segmentation constraints are applied. The intensity of each pixel is analyzed in this algorithm. Afterward, the mentioned pixel will be classified inside an image segment to which

has the nearest mean intensity value. Hence the problem could be explained as a minimization problem:

$$F(S,M) = \sum_{j=1}^{k} \sum_{p_i \in s_j} \|p_i - \mu_j\|^2 \qquad (3.11)$$

where μ_j is the mean value for class j [113-115].

FCM algorithm is one of the other famous algorithms used for MR image segmentation, in which smoother segmentation constraints are applied. FCM algorithm works better for overlapped data. This clustering method allows one vector to belong to one or more clusters and it works based on the minimization of an objective function, which is shown in Equation 3.12.

$$J_m = \sum_{i=1}^{N} \sum_{j=1}^{C} {U_{i,j}}^m \|x_i - c_j\|^2 \quad , \quad 1 < m < \infty \qquad (3.12)$$

where N is the number of vectors, C is the number of clusters, *m* is any real number greater than 1, u_{ij} is the degree of membership of x_i in the cluster j, x_i is the i_{th} vector and c_j is the center of the cluster

Minimizing the objective function happens in an iterative process consisting of four steps as the followings.

1- Initialize *U=[uij]* matrix, *U(0)*

2- At the k-step: calculate the central vectors *C(k)=[c_j]* with the following equation.

$$c_j = \frac{\sum_{i=1}^{N} {U_{i,j}}^m . x_i}{\sum_{i=1}^{N} {U_{i,j}}^m} \qquad (3.13)$$

3- Update *U(k) , U(k+1)*

$$U_{i,j} = \frac{1}{\sum_{k=1}^{c} \left(\frac{\|x_i - c_j\|}{\|x_i - c_k\|} \right)^{\frac{2}{m-1}}} \qquad (3.14)$$

4- If || *U(k+1) - U(k)*||<£ then STOP, otherwise return to step 2.

Classical FCM is suffering from some disadvantages for example the algorithm is very dependent just on intensities , therefore the method results are not suitable for noisy images. Several extensions and improvements have been applied to the basic FCM to resolve the problems with MR image artifacts. Some extensions have improved the objective function to

resolve the problem [116, 117] and some extensions have improved cluster centers to resolve the problem[118, 119] some others have worked on bias field [120, 121]. Ahmed et al. proposed FCM-S method which exploits spatial information [120]. Furthermore, Li has worked on membership degree in FFCM-S method to make FCM-S faster [122]. Krishnapuram et al. worked on Possibilistic c-means (PCM), he has relaxed the normalized membership constraint in PCM but this method is still suffering from its sensitivity to parameterization [123, 124].Fundamental FCM algorithm is time consuming due to its optimization procedure. Therefore several extensions and improvements have been applied to the original FCM algorithm in order to make the process more efficient and faster. For example, Al-Zoubi, et al. [125] removed the points with a membership degree smaller than a threshold value in order to make the algorithm faster. Also Li, et al. [122] exploited histogram data in order to decrease the process duration. Result of applying the FCM on the MRI is depicted in Figure 3.8.

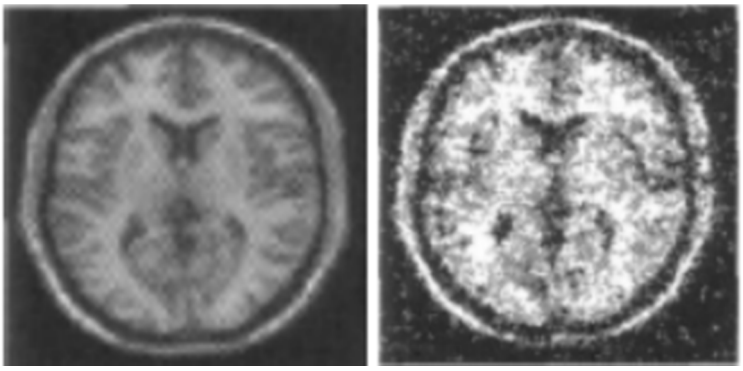

Figure 3.8. FCM segmentation (right) on MRI image(left) [126]

CHAPTER 4

Proposed Method

In this chapter we are about to explain the main framework which is proposed for segmenting MRI data to four tissues (Spongy bone, Cortical bone, Muscle and Adipose tissues). This framework is a combination of newly developed deformable kernel Fuzzy C-Means (DKFCM) algorithm, which is a heuristic algorithm proposed in this thesis specifically for improving the accuracy on the edges of the tissues, a generalized spatial Fuzzy C-Means algorithm (GSFCM) [130], some heuristic algorithms for finding the relational position of one tissue in respect to the other tissues, edge reduction, some heuristic algorithms for finding and fixing the abnormal changes in the slides and some small interaction (less than 30 second) by an operator. These methods are all well adapted and used for each tissue based on the specific qualities of different tissues.

In this chapter the proposed method is divided to four sections. In each section different methods which are used for extracting each tissue and their connection to each other are well explained.

4.1. Extracting The Spongy Bone

In this section the framework, which is exploited for extracting the spongy bone from the MRI is explained. This framework is a combination of a short but effective contribution from the operator (less than 30 seconds on the seed slice), The Proposed deformable Kernel Fuzzy C-Means (DKFCM) for improving the accuracy of segmentation on the edges of the spongy bone and a forward and backward transfer of the segmentation at the seed slice to other slices for utilizing the connection between the spongy bone sections at the successive slices.

Figure 4.1 visualizes the flowchart for extracting the spongy bone from MRI data. First one of the slices is chosen as the seed slice by the operator (step 2). Then, the system applies a pre-segmentation and edge deduction (step 3). Then, the operator corrects the boundaries (step 4) and clicks on the target tissue pieces (step 6). Then, the system removes the extra parts (step 7) and improves the edges by applying the proposed DKFCM method (step 8). After that the system transfers the segmentation to

the next slice. So, from the next slice after the seed, the system doesn't get help from the operator and only the steps 7, 8 and 9 are needed.

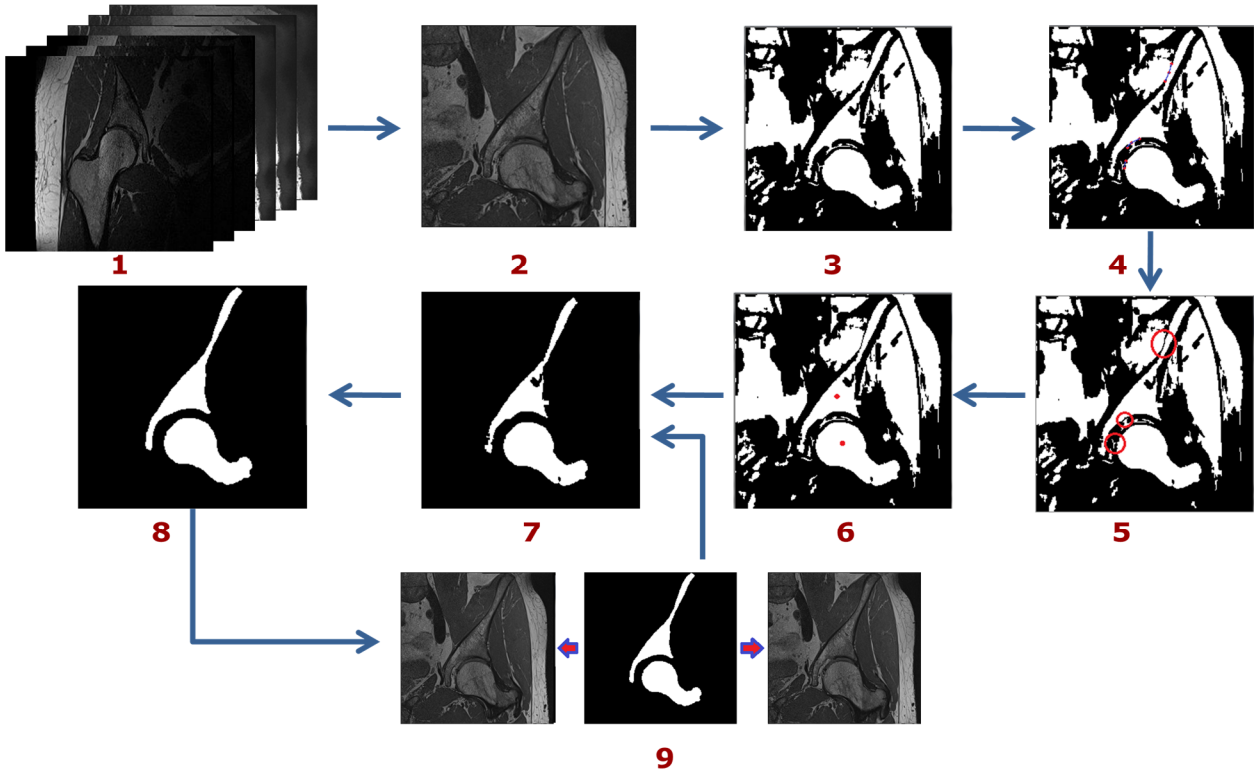

Figure 4.1. Visual flowchart, showing the steps for extracting the spongy bone from MRI data

4.1.1. Contribution from the Operator

The segmentation process begins from the seed slice and continues until the segmentation of the last slice. The seed slice can be selected from any of the slices in the Sagittal, Axial or Coronal views that contain a part of each of the bones in MRI data. If a slice with all of the bone parts doesn't exist, we need to choose more than one seed slice to have all of the bone parts.

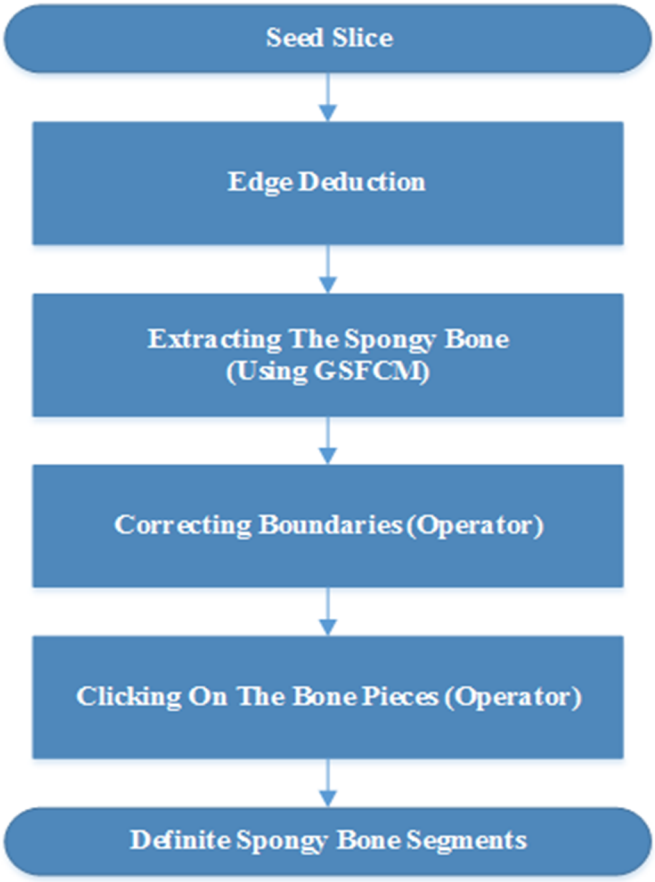

Figure 4.2. Block diagram of the segmentation at the seed slice

The block diagram of the segmentation at the seed slice is shown in Figure 4.2. The very first step is the edge deduction. We know that the spongy bone is surrounded by a thin layer of the cortical bone. A two dimensional slice of the hip joint is shown in Figure4.3 (a). As shown the spongy tissue is bonded with the cortical bone. So, due to the lower intensity of the cortical bone in comparison with the spongy, muscle and adipose tissues, it is possible to separate the spongy bone from other tissues, by finding the edges and deducting them from the image.

For this purpose, first we apply canny edge detection on the seed slice to detect the connected edges and then deduct them from the slice. The high and low thresholds for the hysteresis thresholding at the canny edge detection are set to 190 and 75 respectively. The reason for choosing the mentioned threshold is that due to the high rate of noise and intensity inhomogeneity on the MRI, there's always a lot of intensity gradients inside the spongy bone tissue which could be misdetected as edges. In some

cases this unwanted gradient inside the spongy bone can cut a connected part of the spongy bone to separate pieces after the edge deduction. So, there's always a tradeoff between deducting all of the correct edges and not separating the connected spongy bone areas after the edge deduction. For this reason the hysteresis threshold are chosen in a way to make sure that the misdetected edges cannot split up the connected spongy bone parts. Considering that this is a general algorithm and should answer on every slice, it is obvious that in some slices some of the correct edges are not detected. Figure 4.3 clarifies this problem on an MRI slice. Figure 4.3 (a) shows the original slice and figure 4.3 (b) shows the problematic areas on the slice. The red rectangles show the unwanted edges inside the spongy bone area which are capable of splitting the connected area and the blue ellipses show the faint, correct edges. For solving this problem, after the edge deduction a clustering step and also a small help from the operator are considered for the detection and deduction of the edges which are not detected by the canny edge detection. After deducting the edges for increasing the robustness of the framework to the noise (noise can pierce through some parts of the edges and connect the spongy bone to some pixels of the muscle or adipose tissue) and solving the mentioned problem, the GSFCM method [130] is utilized for detecting the spongy bones and making the pre-segmented image. It should be considered that this is not an accurate segmentation we just need to have separate islands at this step. The next step is a very small interaction from the operator. For this purpose the pre-segmented image is provided to the operator and if there's any connection between the spongy bone and other tissues in that slice the operator should first remove that connection. For removing the connections the operator needs to do some clicks on the area that the connection happens, in a way that the clicks cover the whole connection area. The program automatically connects the position of the clicks together and removes the connection. An example of the pre-segmented image with connection is shown in Figure 4.4. Figure 4.4 (a) is the original image, Figure 4.4 (b) shows the original pre-segmented image, Figure 4.4 (c) shows the position of clicks, done by the operator, with red dots and the cutting line which is generated automatically by the program with blue lines and Figure 4.4 (d) shows the final corrected image.

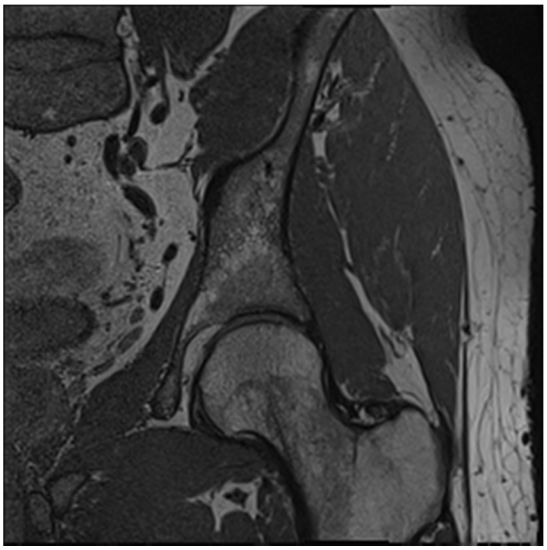

(a)

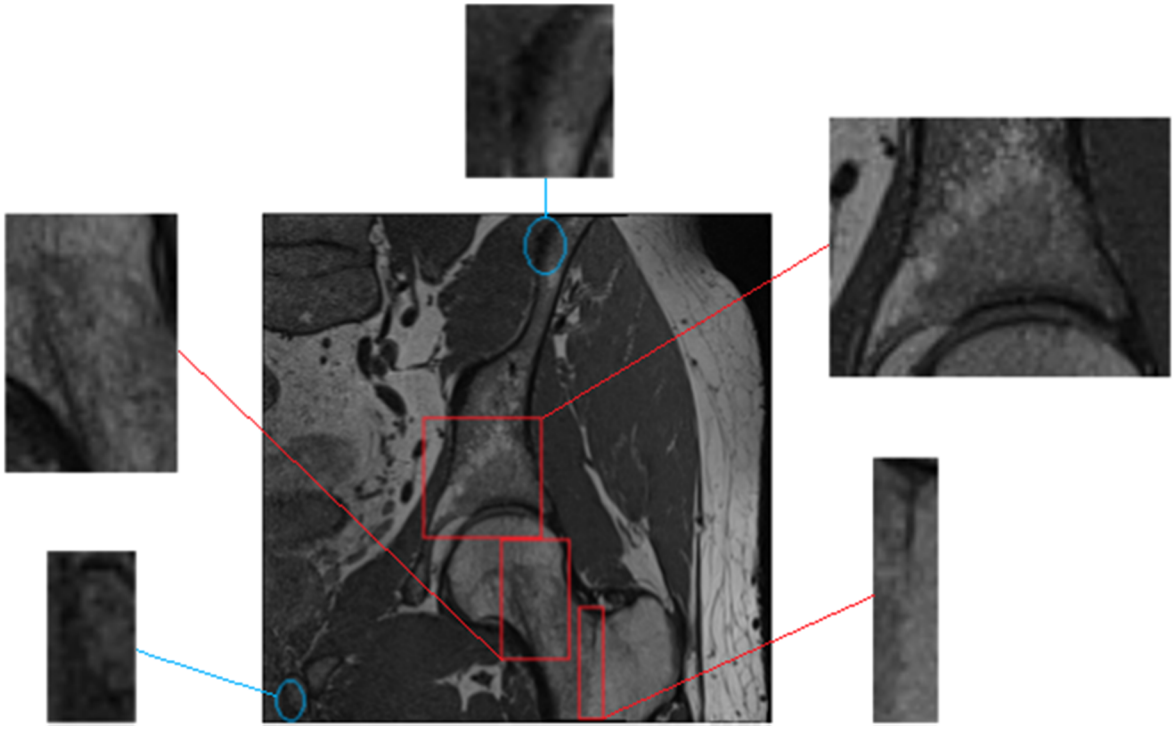

(b)

Figure 4.3. (a) Original slice (b) Problematic areas for the canny edge detection. Red rectangles show the unwanted edges and the blue ellipses show the faint, correct edges

After removing the connections the operator should click on the spongy bone pieces on the image. One click of the mouse on each piece is enough. This interaction, at the worse condition doesn't take more than 30 seconds. Figure 4.5(c) shows the position of clicks by the operator.

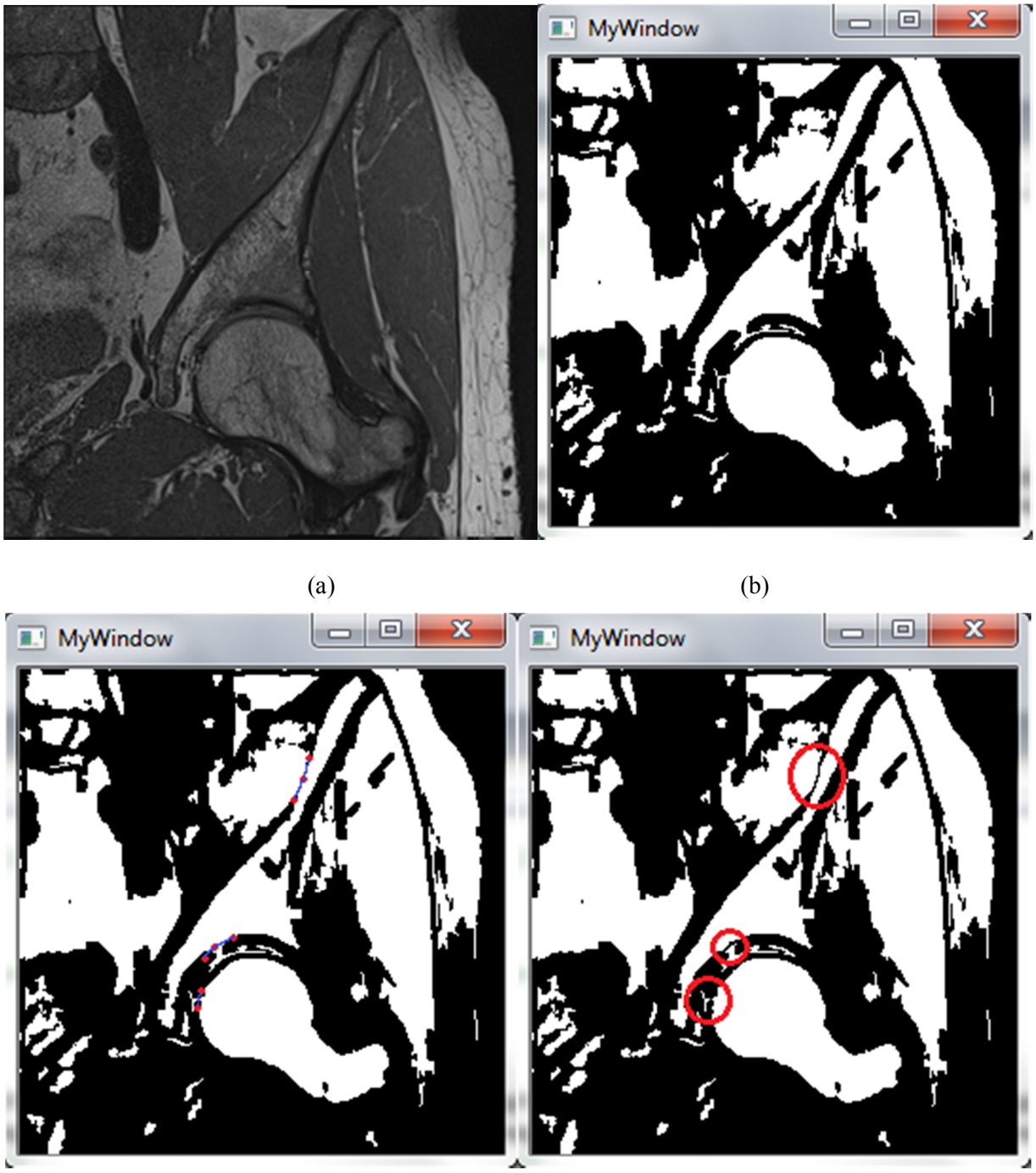

(a) (b)

(c) (d)

Figure 4.4. (a) The original slice, (b) The pre-segmented slice provided to an operator, (c) Boundary corrections by the operator (red dots shows the position of the clicks by the operator and blue line shows the cutting line, which is generated automatically by the program) (d) the final corrected image (red circules specifies the position of corrections)

The final result of this section is acquiring the definite spongy bone areas on the seed slice. This gives us the areas that are definitely spongy bone and no other tissues but with a rough segmentation (figure 4.5 (d)). Now it is possible to continue by improving the accuracy and segmenting the other tissues. As explained at the Section 4.1.4 of this chapter, by using an algorithm which can utilize the connection between the specific tissues in successive slices, clicking on the bone parts on the seed slice is enough for segmenting all of the successive slices and the operator doesn't need to do anything on the other slices.

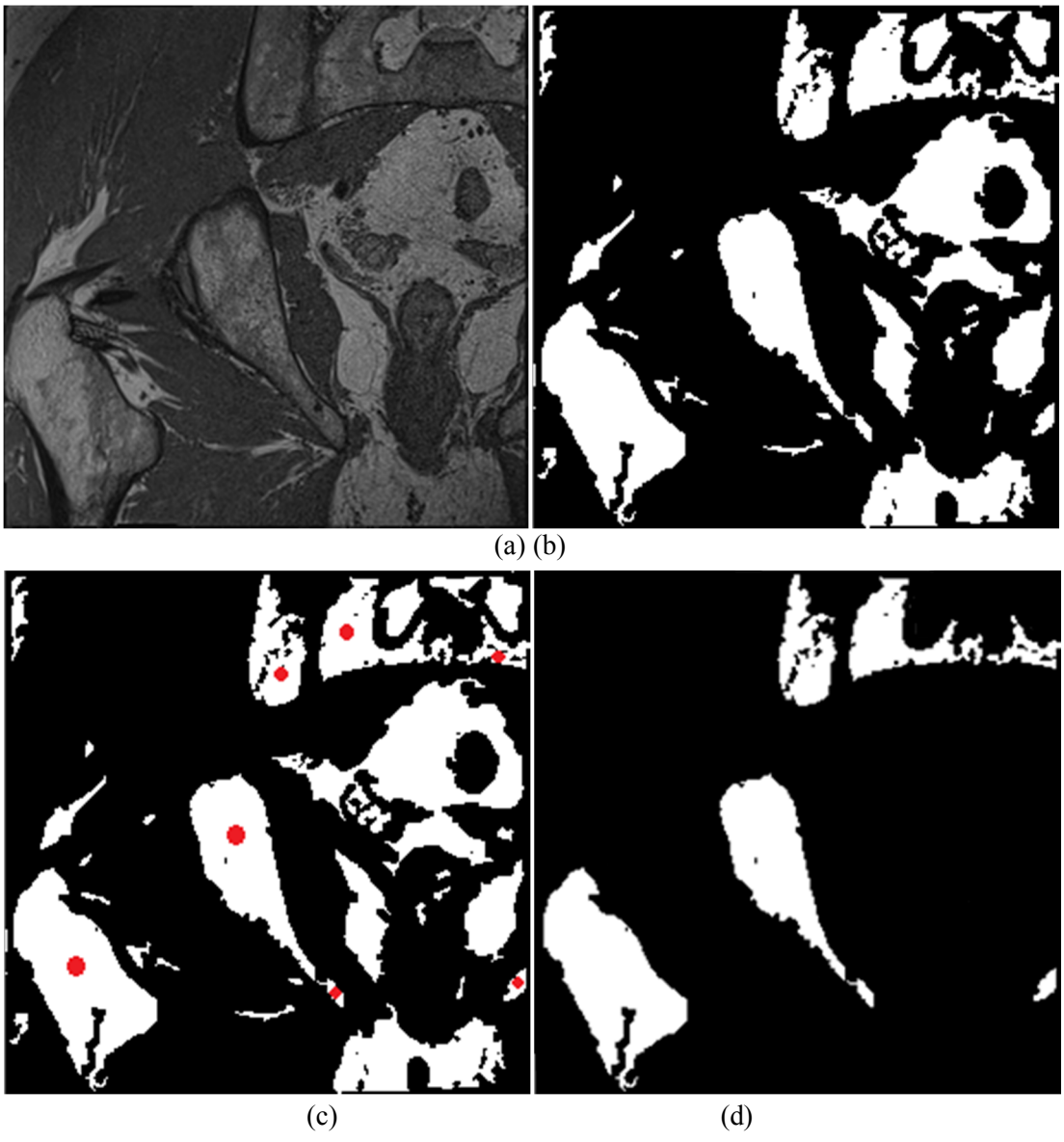

(a) (b)

(c) (d)

Figure 4.5.(a) The original slice, (b) The pre-segmented slice provided to an operator, (c) Places of clicks by the operator (d) definite spongy bone areas

This small but effective interaction by the operator together with the algorithm which is able to find the connection between the specific tissues at the successive slices can improve the accuracy and robustness of the proposed framework against the noise, IIH and overlap between the intensity of the different tissues which is quite common in MRI data.

4.1.2 Improving the Segmentation Results Using the Relative Position

Another method, which is utilized for improving the result of the segmentation, is taking advantage of expert knowledge about the relation between the positions of the different tissues in order to improve the result of the segmentation and making it more robust and resistant to the noise, change in the intensity of tissues in different MRIs and intensity overlap.

According to expert knowledge we know that the spongy bone is always surrounded by a thin layer of the cortical bone. So, the pixels of the spongy bone should be surrounded by the cortical bone pixels. As a result we can remove all of the pixels which are not surrounded by the cortical bone from the spongy bone pixels.

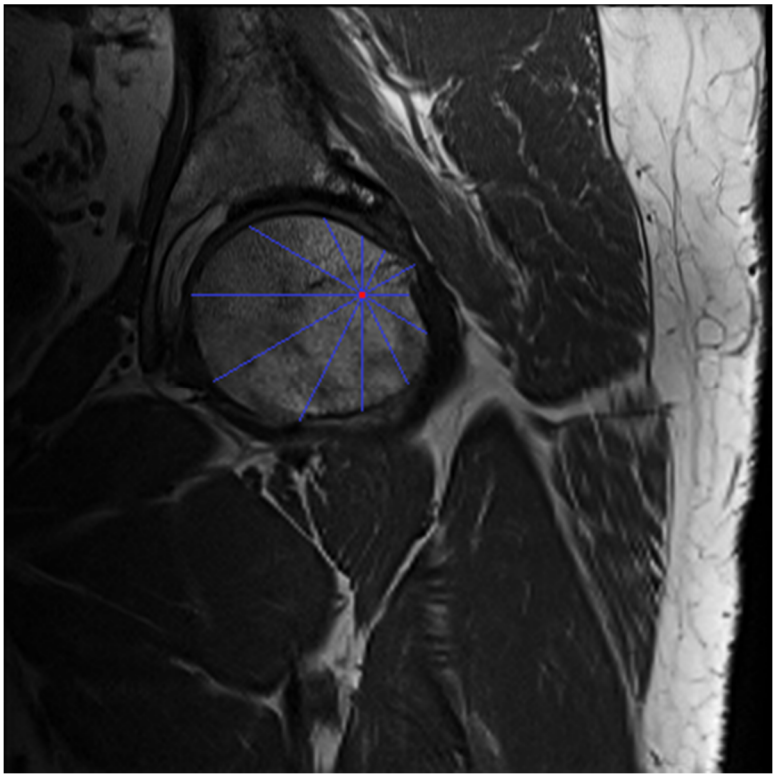

Figure 4.6. Calculating a feature for finding the surrounded pixels by the cortical bone

For obtaining a feature related to this specification, as shown in figure 4.6, the segmenting software draws 6 straight lines in different direction with 30 degree angle from each other that all passes from the pixel under examination (Figure 4.6 is not in real size it is just an example to clarify the idea). Then, the number of lines which are ended to cortical bone pixels at both ends is counted and the ratio of this number to the total number of lines is calculated and used as one of the features for detecting the spongy bone. Equation 4.1 shows this feature.

$$P(s) = \frac{N_{CL}}{T_L} \qquad (4.1)$$

where N_{CL} is the number of lines which are connected to the cortical bone from both ends and T_L is the total number of lines.

4.1.3.Deformable Kernel Fuzzy C-Means (DKFCM)

For an accurate segmentation of the tissues on the edges the newly developed DKFCM method is proposed in this paper. The core of this method is a generalized spatial FCM method. At the spatial FCM the cluster of each pixel is determined based on the intensity of the main pixel and its neighboring pixels. In DKFCM, the neighboring voxels are bounded in a 3 dimensional deformable kernel around the main voxel.

As shown in the flowchart of Figure 4.7, the method begins with initializing the first searching area and neighboring kernel, continues by deforming the neighboring kernel and adjusting the searching area in an iterative mode based on the segmentation obtained at the previous iteration and ends when the result of segmentation converges and satisfies the stop condition.

Figure 4.7. DKFCM algorithm for improving the edges of the spongy bone

As explained, the first step is initializing the searching area and the neighboring kernel. The initialized kernel is a 3×3×3 cube, as shown in Figure 4.8 (a). The initialized searching area is a strip around the chosen bone parts on the current, the next and the previous slices. The width of this strip is equal to the maximum width of the cortical bone in MRI dataset plus three pixels. After initialization, the searching area is segmented with the GSFCM method using the initialized neighboring kernel. GSFCM, which is proposed by Huynh Van Lung et al. [130], is a generalized version of the spatial FCM. This method considers the clusters of the neighboring pixels in addition to their distance from the central pixel. For this purpose, the function P_{ik} is defined as follows.

$$P_{ik} = \sum_{j=0}^{N_k} g(u_{ij}) \left(\sum_{l=0}^{N_k} \frac{d^2(x_k, x_j)}{d^2(x_k, x_l)} \right)^{-1} \quad (4.2)$$

where, N_k is the set of the neighborhood pixels around the central pixel k, which in our method we confine it to our deformable 3D kernel.U_{ij} is the membership value of the neighboring pixel j to cluster ibased on the centroid at each cluster and d() shows the distance between the pixels. Function P_{ik} is then used to calculate the membership function (w_{ik}) and the center of cluster (v_i) as follows. The clustering happens by updating the v_i and w_{ik} in an iterative process same as the process which is explained for FCM in Chapter 3. Based on the experiments on available MRI datasets, the initial centroid for the spongy bone, cortical bone, muscle and adipose tissue are defined as 72, 13, 40 and 175 respectively.

$$w_{ik} = \left[\frac{(d^2(x_k, v_i) f(P_{ik}))^{\frac{1}{m-1}}}{\sum_{j=1}^{c} (d^2(x_k, v_j) f(P_{jk}))^{\frac{1}{m-1}}} \right]^{-1} \quad (4.3)$$

$$v_i = \frac{\sum_{k=1}^{n} {w_{ik}}^m x_k}{\sum_{k=1}^{n} {w_{ik}}^m} \quad (4.4)$$

After segmenting the initialized searching area with the initialized kernel and obtaining the cortical and spongy bone, an iterative process begins for minimizing the segmentation error on the edges of the bone. At each of the iterations we change the searching area and the kernel in 3 dimensions, based on the obtained contour of the bone at the previous iteration and then, repeat the segmentation process. The iteration continues until the stop condition is fulfilled. Equations 4.5 and 4.6 show the stop condition.

$$\sum_{n \in N_r} d\left(SI_n^{(r)} - SI_n^{(r-1)} \right) < \varepsilon_L \quad (4.5)$$

$$d\left(SI_n^{(r)} - SI_n^{(r-1)} \right) = \begin{cases} 1 & SI_n^{(r)} - SI_n^{(r-1)} \neq 0 \\ 0 & SI_n^{(r)} - SI_n^{(r-1)} = 0 \end{cases} \quad (4.6)$$

where, N_r is the set of searching area pixels at the current iteration. SI is the segmented searching area, r shows the current iteration and r-1 shows the last iteration. ε_L is a natural number defined by the user.

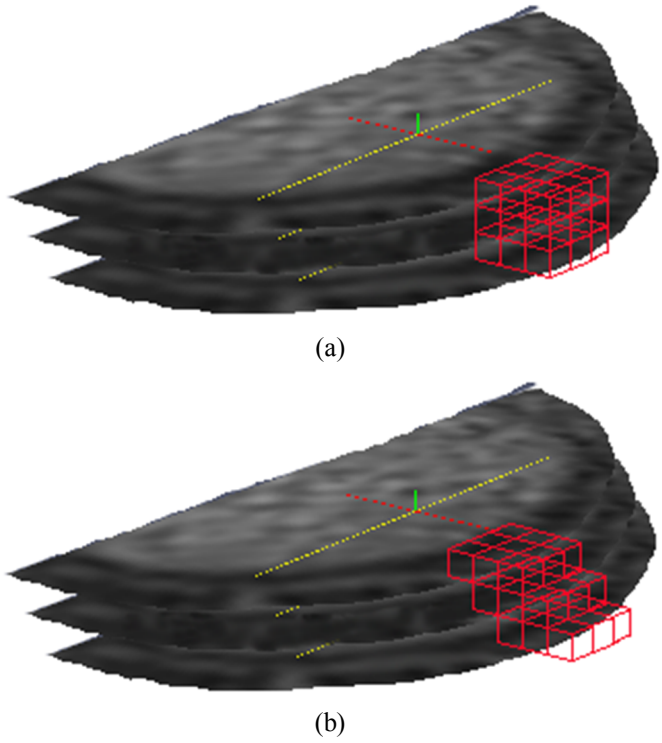

(a)

(b)

Figure 4.8. defororming of the deformablekernel (red cube) during the DKFCM process to take the shape of the edge in three successive slices (a) The deformable kernel (red cube) at the first iteration, (b), The deformed kernel at the second iteration. The green, yellow and red lines shows the direction of the z, x and y axes respectively

Figure 4.8 shows the deforming process of the kernel. Figure 4.8 (a) shows the kernel (red cube) at the first segmentation iteration and Figure 4.8 (b) shows the kernel at the second iteration. The kernel is deformed to adapt itself with the position of the cortical bone (spongy bone edges) in the current, next and previous slices.

The kernel is made of three movable blocks and the new distance between the position of the middle and top blocks and also the middle and bottom blocks in x and y coordinates are calculated by equations 4.7 and 4.8 respectively.

$$d_{ij}^{x} = \sum_{y=-1}^{1} B_y[(f_{jy} + l_{jy}) - (f_{iy} + l_{iy})] \quad (4.7)$$

$$d_{ij}^{y} = \sum_{x=-1}^{1} B_x[(f_{jx} + l_{jx}) - (f_{ix} + l_{ix})] \quad (4.8)$$

d_{ij}^{x} and d_{ij}^{y} are the distance between the blocks at layers i and j in x and y coordinates respectively. X and Y axis are shown with yellow and red line in figure 4.8 respectively. Layers are assumed to be expanded in the Z axis direction. (Green line in figure 4.8) Y and X are the row and column number in the 3×3 block, which is located at the same layer as the main voxel (middle layer). Row and columns are expanded in the y and x axis directions respectively. For the main voxel the row and column number is zero and for the next and previous voxels they are assumed 1 and -1respectively. B_y and B_x are the weight of each row and column respectively. F_{iy} and L_{iy} are the x location of the first and last voxels of the cortical bone which are located at the row y of the layer i. Similarly F_{ix} and L_{ix} are the y location of the first and last voxels of the cortical bone which are located at the column x of the layer i

For updating the searching area at the current iteration, the width of the cortical bone at the previous iteration is calculated. The new searching area is from the (width/2) pixels inside the cortical bone to (width/2) pixels outside it.

4.1.4. Backward and Forward transfer of the segmentation at the seed slice

After the convergence of the algorithm in one slice and finding the spongy and cortical bone regions, an automatic backward and forward transfer of the segmentation at the seed slice for finding the bone regions in the back and forward slices begins. The term backward and forward transfer is used specifically in this thesis for this method because we start by performing an accurate segmentation on the seed slice, using a small help from the operator and then the system propagates this accurate segmentation to the other slices in order to have an accurate segmentation on them as well. In another word, we are propagating the accurate segmentation on the seed slice to the other successive slices. The idea is that, because of the small distance between the slices, there is not a big change in the contour of the bone in successive slices. So, having the boundaries of the bone in one

slice will help us to narrow down our searching area for the bone in the back and forward slices from the whole image to just a strip around the current contour of the bone. In Figure 4.9, a part of the bone at the current slice is marked, the definite spongy bone area at the next slice is bounded with the blue dashed line and the searching area at the next slice is the area between the red and blue dashed lines. In our datasets, which consists of 160 slices in the coronal view, the initialized searching area at the next slice is defined as 5 pixels outside the current contour of the bone and 5 pixels plus the width of the cortical bone inside it. After finding the definite spongy bone area and the initialized searching area at the next slice the process continues by applying DKFCM on the searching area of the next slice. The segmentation process continues until the segmentation of the last slice.

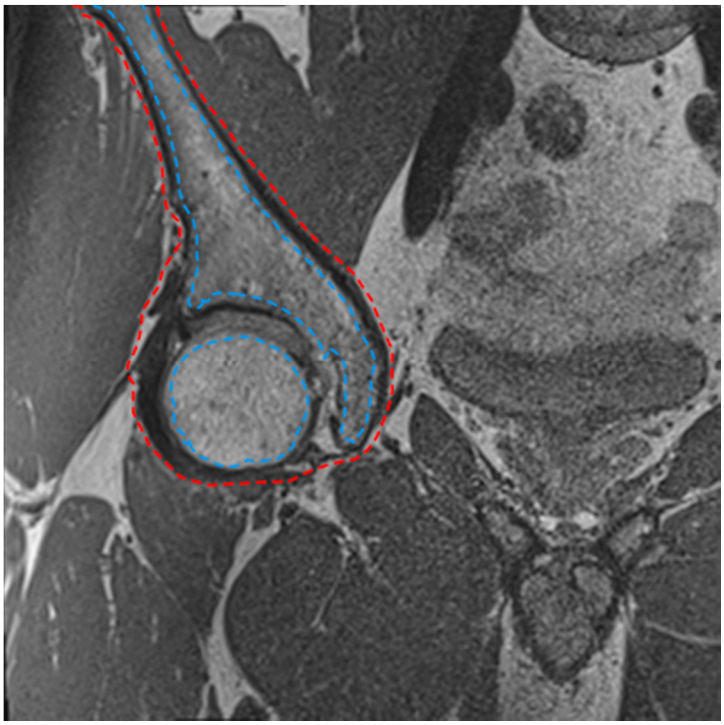

Figure 4.9. The definite spongy bone and the searching areas

For clarifying the idea in figure 4.10 the transfer of the searching area from the seed slice to the back and forward slices are shown. In this image three sucessive slices from a MRI database are shown. It is assumed that the slice b in the middle is chosen as the seed slice. Then, based on the method that was explained at the previous sections by getting help from the operator, the bone parts are segmented accurately.

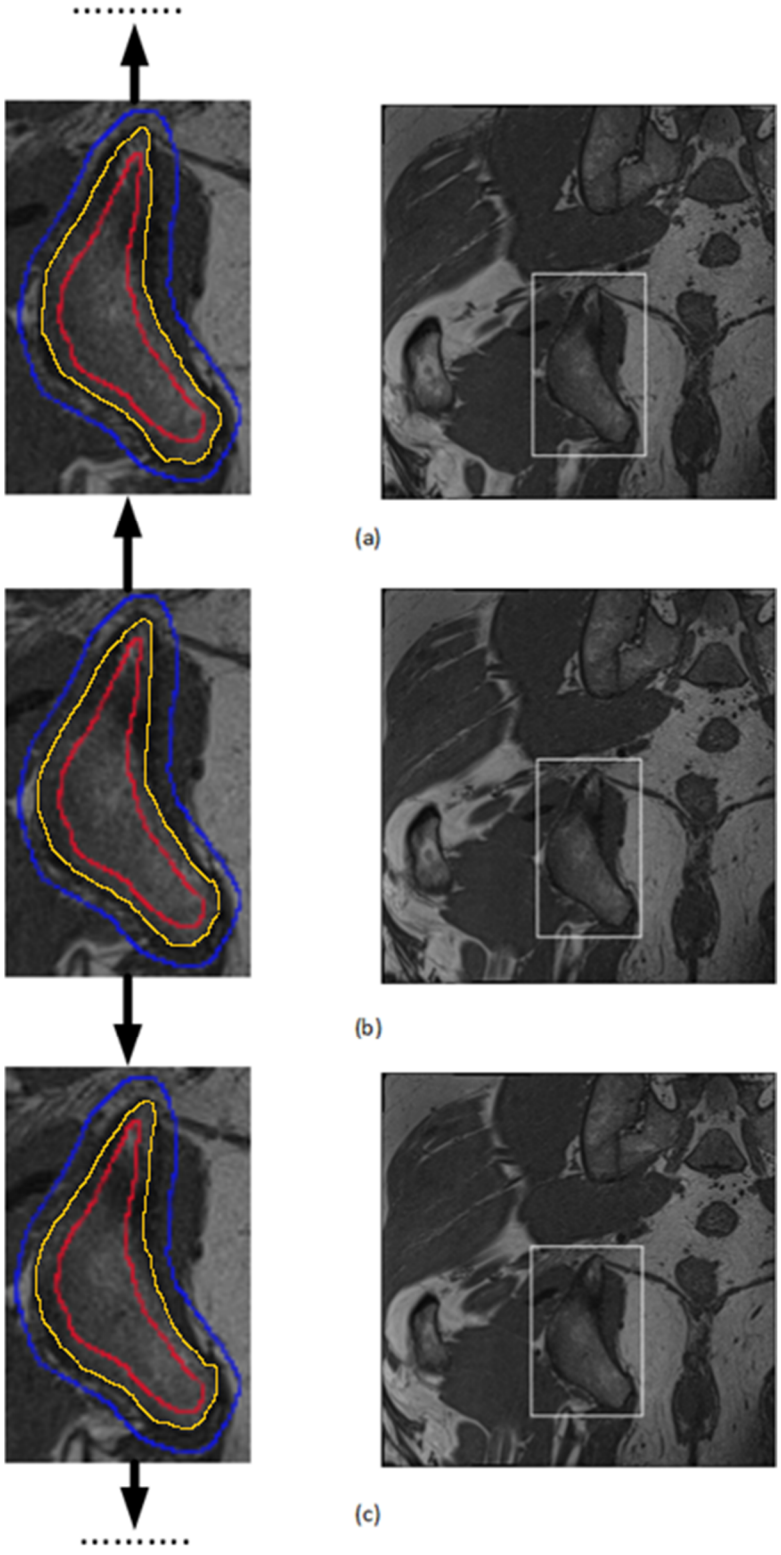

Figure 4.10 Projecting the searching areafrom the seed slice (slice b) to the back and forward slices (slices a and c respectively). Searching area is the area between the the blue and red lines. The yellow line shows the contour of the spongy bone

After the segmentation, the transfer process starts by choosing the searching area for the back and forward slices. In figure 4.10 the searching area is shown for one of the bone parts, which is bounded by the white bounding box on each slice. This area is the area between the blue and red lines at the zoomed area, which is shown on the left side of each slice. After finding the searching area at the seed slice (slice b), it has to be mapped on the back and forward slices (slices a and c respectively). The searching area is the area that has to be segmented on the back and forward slices for finding the spongy and cortical bone tissues. The area inside the red line is the spongy bone and doesn't need to be processed. As shown in the example of figure 4.10 there's no spongy or cortical bone outside of the blue line, everything inside the red line is the spongy bone and between the red and blue lines there's a combination of spongy bone, cortical bone and other possible tissues that has to be segmented. After segmenting the back and forward slices the transfer continues by finding the searching area on each of them and maping it to the next slice in the line.

4.2Extracting the Cortical Bone

In this section the methods and algorithms which are used for extraction the cortical bone out of MRI data are explained. Please note that for extracting the cortical bone some of the methods which are already explained in Section 4.1 like the DKFCM and backward and forward transfer of the segmentation at the seed slice are also used that we don't explain them again at this section.

4.2.1 Removing the Black Margin

The first step in detecting the cortical bone is removing the black margin around the slides, which is actually the empty space around the body and its intensity is completely overlapped with the intensity of the cortical bone in the MRI. The contour of black margin is bounded by the red line in Figure 4.11.

AS explained the intensity of this black margin is overlapped with the cortical bone and another feature is needed for detecting this margin. By referring to expert knowledge about the physiology of the body we can find out that there's a thick layer of adipose tissue under the skin that surrounds the other tissues. So, it is concluded that the black margin which is the free space around the body should be confined between the edges of the MR images and the thick layer of adipose tissue under the skin. As a result two features as the followings are exploited for detecting and removing the black margin.

1- The intensity

2- Placing between the edges of the MRI and a thick layer of the adipose tissue.

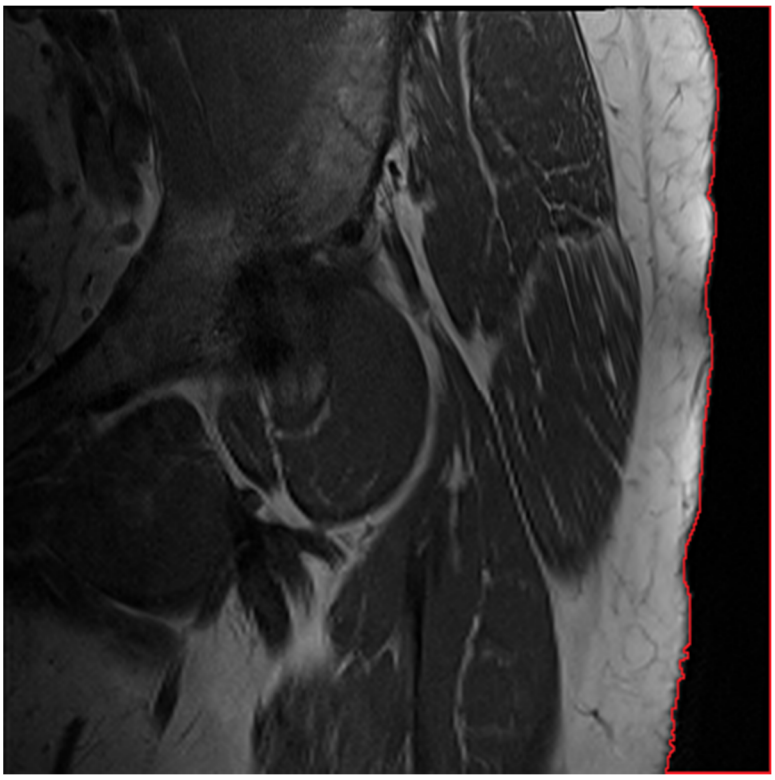

Figure 4.11. The black margin around the MRI

4.2.2 Improving the Segmentation of the Cortical Bone Using the Position Detection

Position detection based on expert knowledge is one of the methods which are utilized in this work for improving the accuracy and robustness of the segmentation. According to expert knowledge we know that the bone consists of the spongy bone and cortical bone. The spongy bone is placed in the middle and it is surrounded by a thin layer of the cortical bone. After pre-segmenting the MRI with GSFCM and finding the potential cortical bone areas the software filters and refines the detected areas using the position detection.

For using the position situation in detecting the cortical bone a feature is needed that takes into account the main specifications of the cortical bone in relation with the other tissues. As explained and

shown in Figure 4.12,the cortical bone forms a narrow strip around the spongy bone. So, if we look at the MRI there are three visual features that we can use for detecting the cortical bone as the followings.

1- Intensity.

2- It is a thin layer.

3- It is around the spongy bone and has a high volume of connection with the spongy bone.

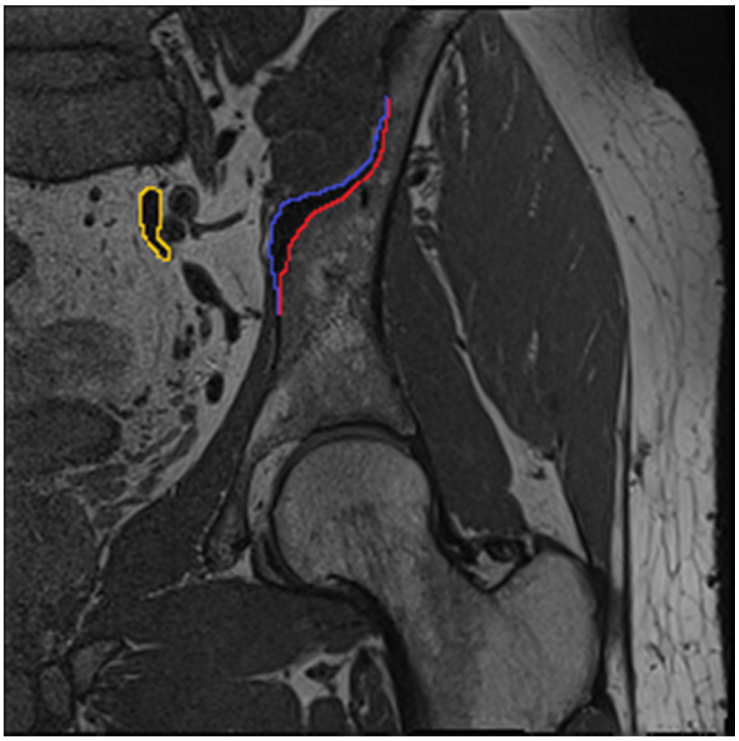

Figure 4.12. Cortical bone and its visual features

The intensity is already used in the GSFCM along with the relational position of the pixels for detecting the cortical bone. For taking into account the two other features as shown in equation 4.9 the ratio of the number of voxels which are connected to the spongy bone to the total volume of the cortical bone is calculated and used as a feature for detecting the cortical bone this feature is called P(c) in this thesis and featured in equation 4.9. As shown in Figure 4.12, since the cortical bone layer is thin and it has a high volume of connection with the spongy bone the P(c) ratio is quite high for the cortical bone in comparison with the other tissues that have intensity overlap with this tissue. So, the proposed feature is very useful for detecting the cortical bone.

In figure 4.12, The area between the red and blue line shows a part of the cortical bone and the red line shows the pixels on this area which are connected to the spongy bone as you can see even on the thick areas of the cortical bone like the one which is shown the ratio of the pixels which are connected to the spongy bone to the total area of the cortical bone (P(c)) is high. The area which is confined by the yellow line is an example of an area which has the same intensity with the cortical bone but it can be easily filtered by the P(c) feature.

$$P(c) = \frac{N_{cp}}{T_A} \qquad (4.9)$$

where N_{CP} is the number of cortical bone pixels which are connected to the spongy bone and T_A is the total number of pixels on the cortical bone area.

4.3 Extracting the Muscle

After extracting the spongy and cortical bone from the MRI what remains in the hip area are the muscles, the adipose tissue and some other organs like ligament, blood vessels, bladder, etc. A model from the horizontal cross section of the hip region is shown in figure 2.4. Bone, muscle and adipose tissue together with the other organs are shown in this figure.

There are some separate muscles at the hip area which together consist a big portion of the muscle mass in the whole body. Figures 2.8 and 2.9 provide a deep and superficial view from the muscles in the hip region respectively.

In this chapter, the algorithms and methods which are used for extracting the muscle from the MRI are explained. Concisely, a combination of edge deduction, GSFCM, a small interaction from the operator, forward and backward transfer and the proposed DKFCM method for improving the segmentation on the edges are utilized together for separating the muscle from other tissues and organs.

The flowchart for extracting the muscle from the MRI is shown in Figure 4.13. As shown the first step is deducting the already segmented spongy and cortical bone from the seed slice. After that a

canny edge deduction applies on the image. The main purpose of the edge deduction at this point is separating the muscle areas from the other areas and having them in separated blobs (connected pixels). After edge deduction by applying the GSFCM segmentation method the muscle sections are extracted and the result is provided to the operator at this point the operator is asked to correct the boundaries of the muscle sections to remove any possible connection between the muscle blobs and other tissues and then click on the separated muscle sections the method for interacting by the operator is exactly same as the method which is used for the spongy bone and explained in Section 4.1.1. Since after removing the spongy and cortical bone from the image the overlap between the intensity of the remaining tissues is quite lower compare to the intensity overlap between the spongy bone, cortical bone and muscle and also the overlap between the adipose tissue and spongy bone, it is possible to totally dismiss the interaction by the operator for segmenting the muscle. However, this interaction can still improve the segmentation quality especially in law quality MRI data. After this step, the non-muscle areas are removed and the segmentation process continues by utilizing the proposed DKFCM method for improving the edges of the extracted muscle areas. The DKFCM algorithm is almost the same as the algorithm which is explained in Section 4.1.3. The only difference is that searching area is defined around the current edges of the muscle instead of the spongy bone. After refining the edges of the muscle areas in the seed slice the segmentation process continues by forward and backward propagating the segmentation as explained in Section 4.1.4 and then again refining the edges using DKFCM.

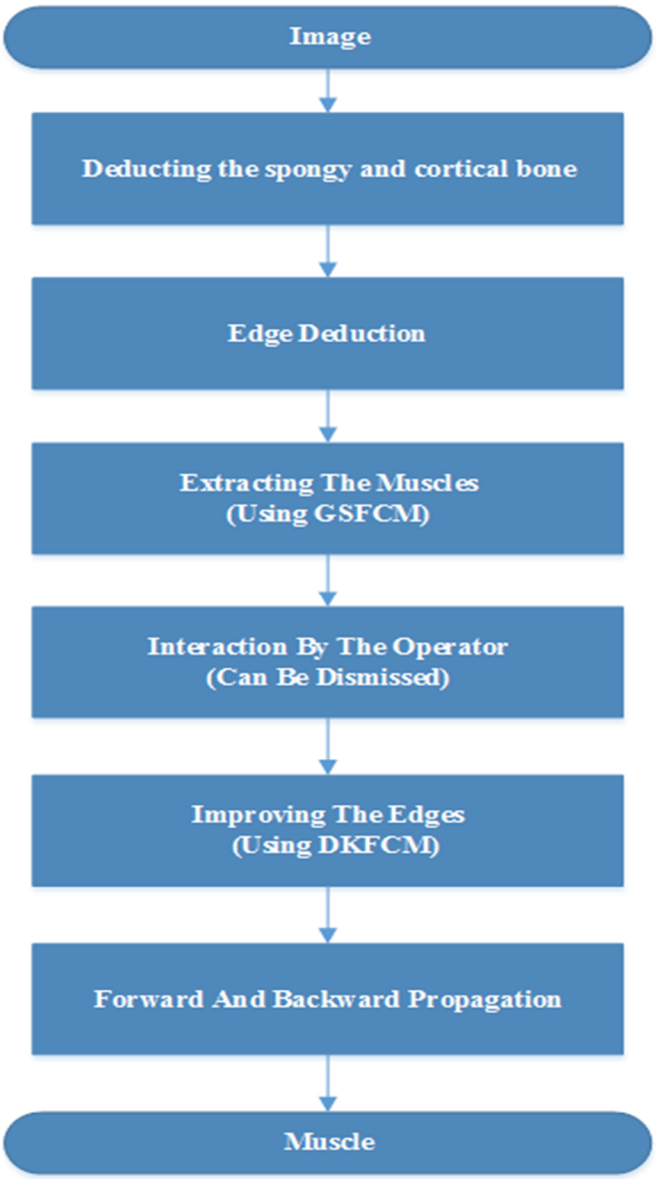

Figure 4.13. Block diagram for extracting the muscle

4.4 Extracting the Adipose Tissue

In this section the algorithm and methods, which are used for extracting the adipose tissue from the MRI are explained.

4.4.1. Overall Algorithm

After extracting the spongy bone, cortical bone, and muscle from the MRI, what remains is a combination of the adipose tissue and some other organs like the blood vessels, ligament, etc. So, a segmentation algorithm is needed for separating the adipose tissue from the available organs. The segmentation algorithm for extracting the adipose tissue is shown in Figure 4.14.

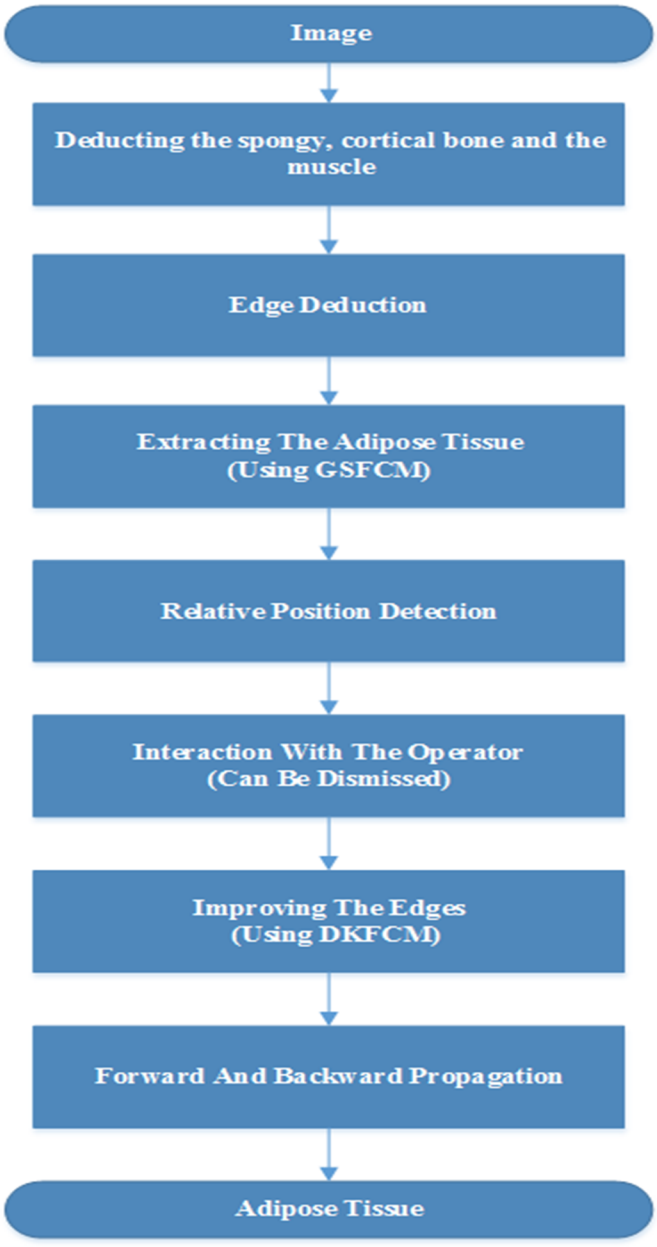

Figure 4.14. The block diagram of the segmentation algorithm for the adipose tissue

As shown in the flowchart, after removing the other segmented tissues from the seed slice a combination of the edge deduction and the GSFCM methods are used for separating the adipose areas. Then, for improving the result of segmentation a relative position detection method is exploited. This method is further explained in Section 4.4.2. After that, an interaction with the operator same as the one which is explained in Section 4.1.1 is performed. Then, DKFCM and forward-backward transfer same as the other tissues are utilized for achieving an accurate extraction of the adipose tissue on the seed slice and propagating it to the other slices. Similar to the algorithm for extracting the muscle, it is possible to dismiss the interaction with the operator because of the lower overlap between the intensity of the remaining tissues. Experimental results proved that the segmentation framework is still accurate even without any interaction with the operator for segmenting the muscle and adipose tissue.

4.4.2. Relative Position Detection of the Adipose Tissue

For improving the result of the segmentation and make it resistant to the noise and intensity inhomogeneity, utilizing the relative position detection of the tissues in respect to the other tissues is one of the effective methods.

Figure 4.15. Missegmented region on the adipose tissue

According to expert knowledge there is a thick layer of adipose tissue under the skin that surrounds the other organs. So, it can be concluded that after the black margin that surrounds the whole body a thick layer of adipose tissue is expected. This can sharply increase the possibility of the existence of the fat in certain rang after the black margin and can be used as a feature in combined with the other features for detecting the adipose tissue. As another result it can be concluded that anything within a certain range after the black margin if it is surrounded by the fat or it is between the fat and the black margin is the fat.

Figure 4.15 shows an example of a region that is missegmented as the muscle without considering the position detection method but can be detected by using the position detection.

CHAPTER 5

Experimental Results and Evaluation

In this chapter the results of applying the proposed method on real MRI data are shown, evaluated and validated by comparing the proposed method with some available methods in literature which are capable of segmenting MRI data to cortical bone, spongy bone, muscle and adipose tissue. For evaluating the proposed method, three different datasets of MRI slices are utilized, which are provided by the Radiology department of the Ottawa General Hospital. The specifications of these datasets are listed in table 5.1

Table 5.1. Testing datasets

Dataset	Gender	Size per voxel	Dimension	Region
Dataset 1	Male	10485760	256×256×160	Right hip
Dataset 2	Male	10485760	256×256×160	Left hip
Dataset 3	Female	3686400	384×384×25	Right hip

This chapter is organized in three main sections in section one the two dimensional results of segmenting the MRI with the proposed method to spongy bone, cortical bone, muscle and adipose tissue are shown. In Section two a three dimensional visualization and modeling of different tissues, which are segmented by the proposed method, are exhibited and in the third section the evaluation methods are explained and the results are compared with some other available methods.

5.1 Two Dimensional Results

MRI data consists of a series of two dimensional slices which are each taken from different depth of the body for showing the performance of the segmentation method the best way is showing the segmentation result on two dimensional slices.

For exhibiting and evaluating the segmentation result of the proposed method the method is applied on three different datasets of MRI to segment them to the spongy bone, cortical bone, Muscle and the adipose tissue. Figure 5.1 shows the extracted spongy bone on three of the slices from three different datasets.

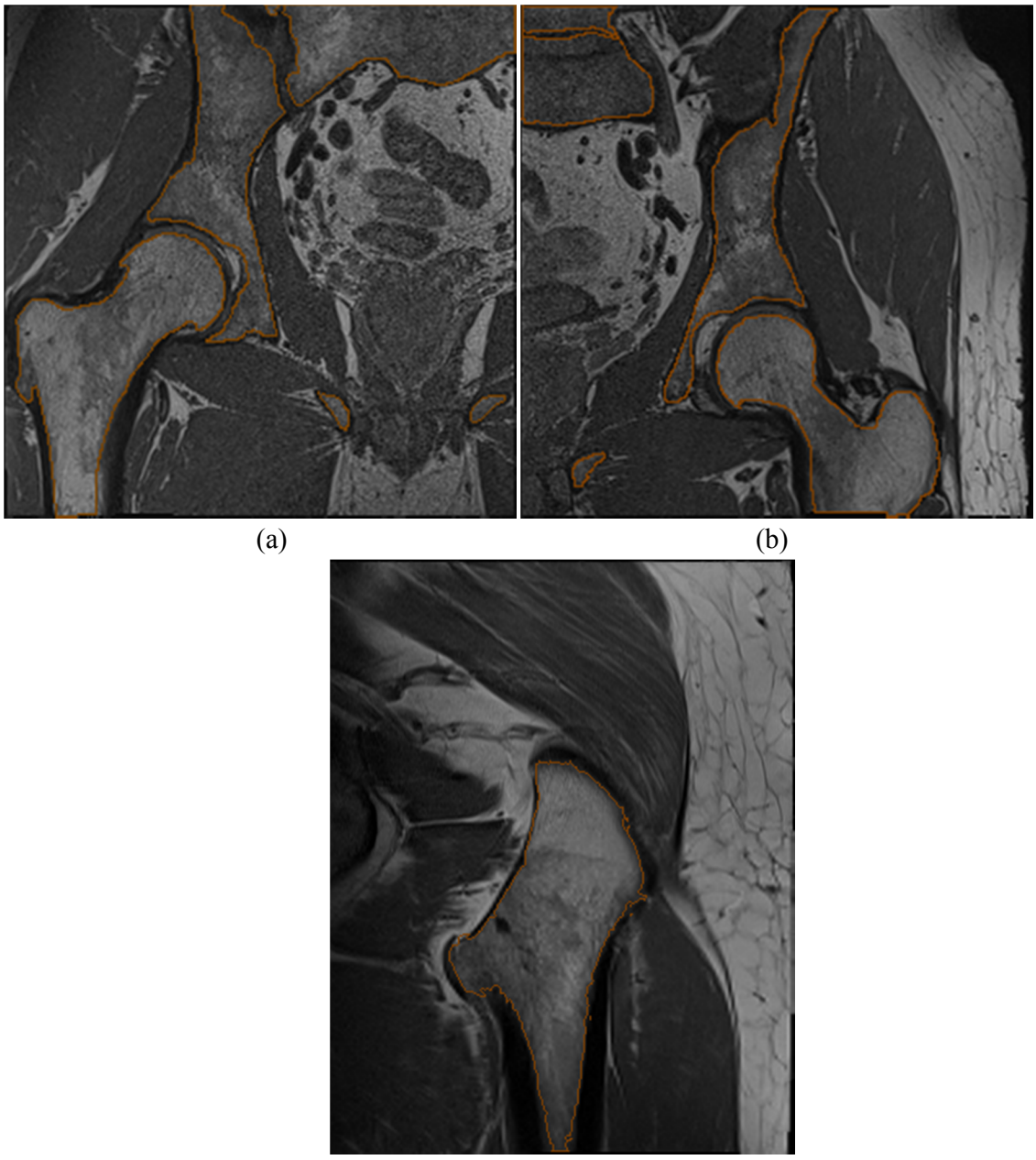

(a) (b)

(c)

Figure 5.1. Contours of the extracted spongy bone from three slices of three different datasets (a) dataset 2, (b) dataset 1 and (c) dataset 3

Figure 5.2 shows the contours of the extracted cortical bone on the same slices.

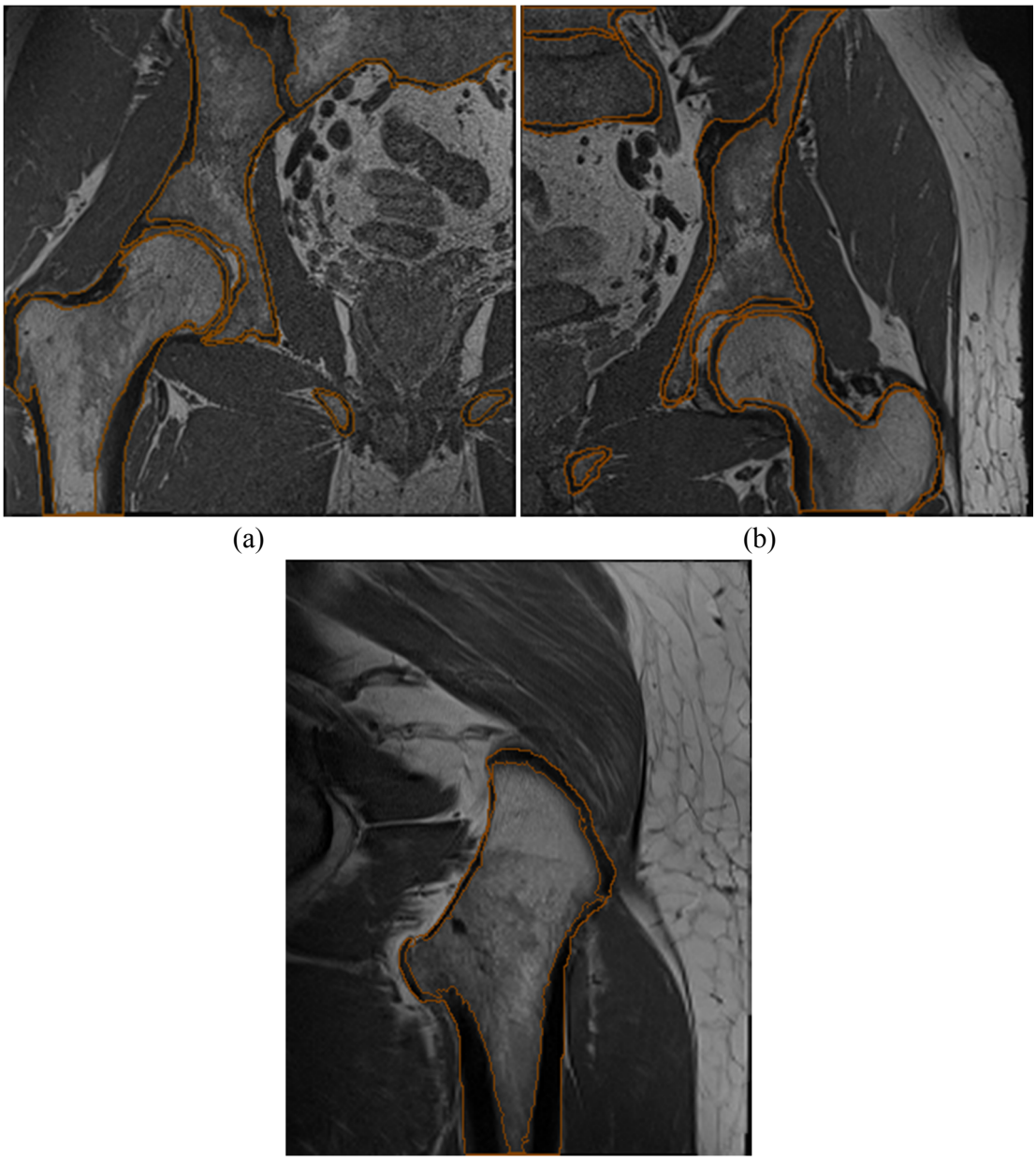

(a) (b)

(c)

Figure 5.2. Contours of the extracted cortical bone from three slices of three different datasets (a) dataset 2, (b) dataset 1 and (c) dataset 3

Figure 5.3 shows the contours of the muscle extracted from the same slices.

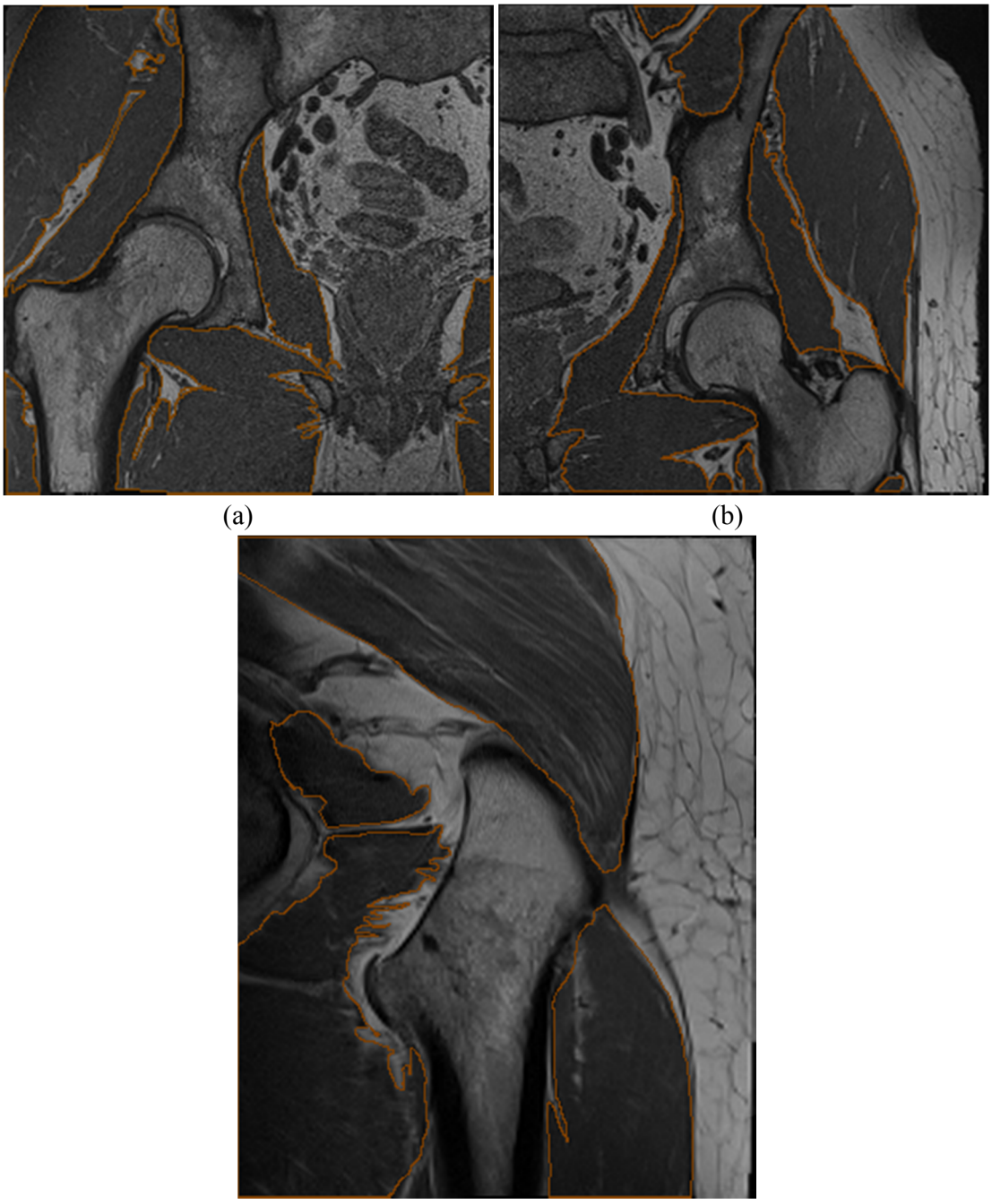

(a) (b)

(c)

Figure 5.3. Contours of the extracted muscle from three slices of three different datasets (a) dataset 2, (b) dataset 1 and (c) dataset 3

The contours of the extracted adipose tissue from the same slices are shown in Figure 5.4.

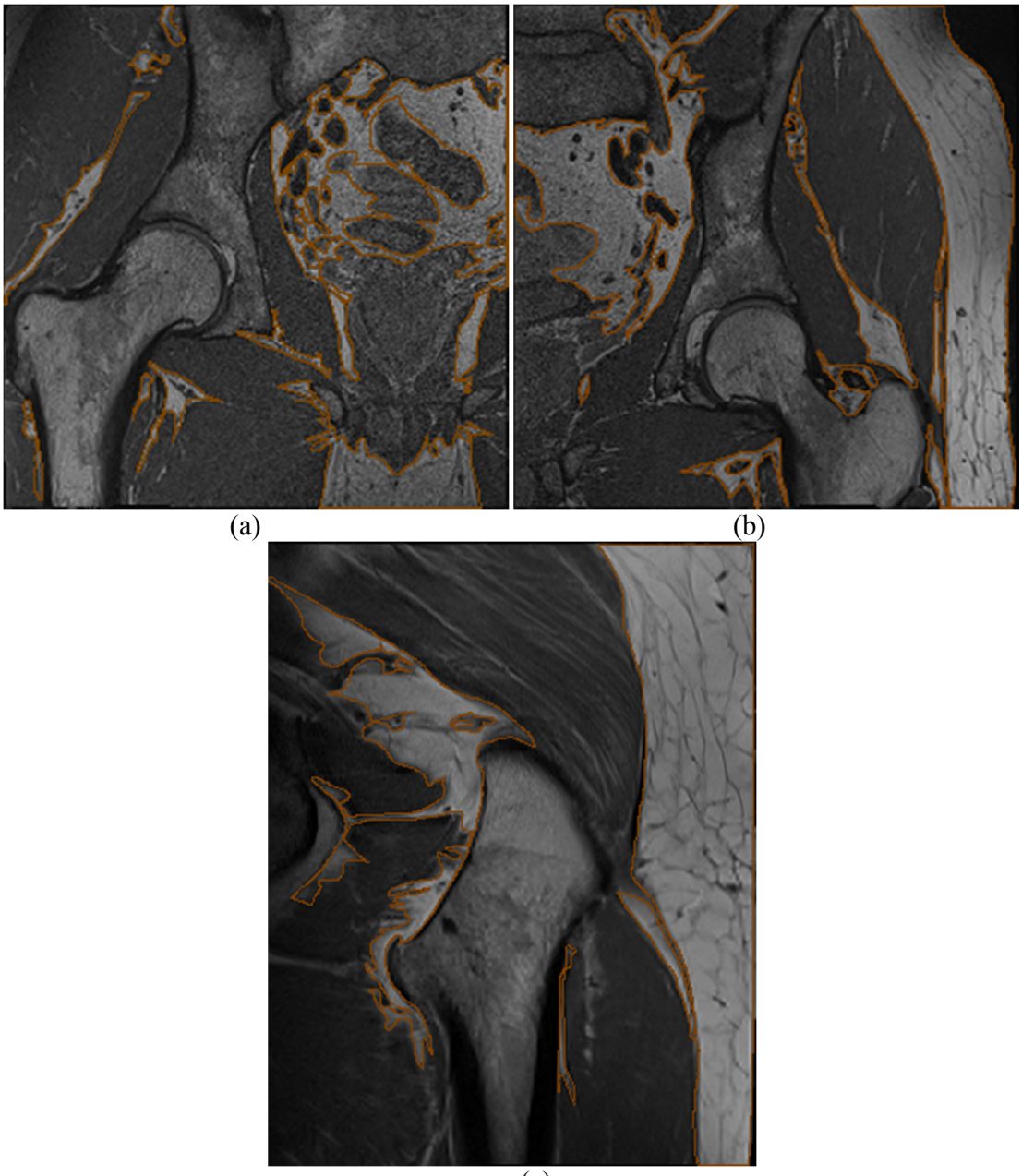

(a) (b)

(c)

Figure 5.4. Contours of the extracted muscle from three slices of three different datasets (a) dataset 2, (b) dataset 1 and (c) dataset 3

5.2 Three Dimensional Visualization and Modeling

As already explained one of the motivations of this work is modeling the body which can help the physicians in detecting some diseases, simulating the surgery and designing implants for a specific patient. After segmentation by putting each slice on its correct position at the MRI volume a 3D

model from the segmented organs of the patient can be obtained. In this section the result of 3D modeling of some of the organs by using the proposed segmentation method are shown.

3D models from the left and right femur, which are extracted from two different datasets, are shown from different views in Figures 5.5 and 5.6 respectively.

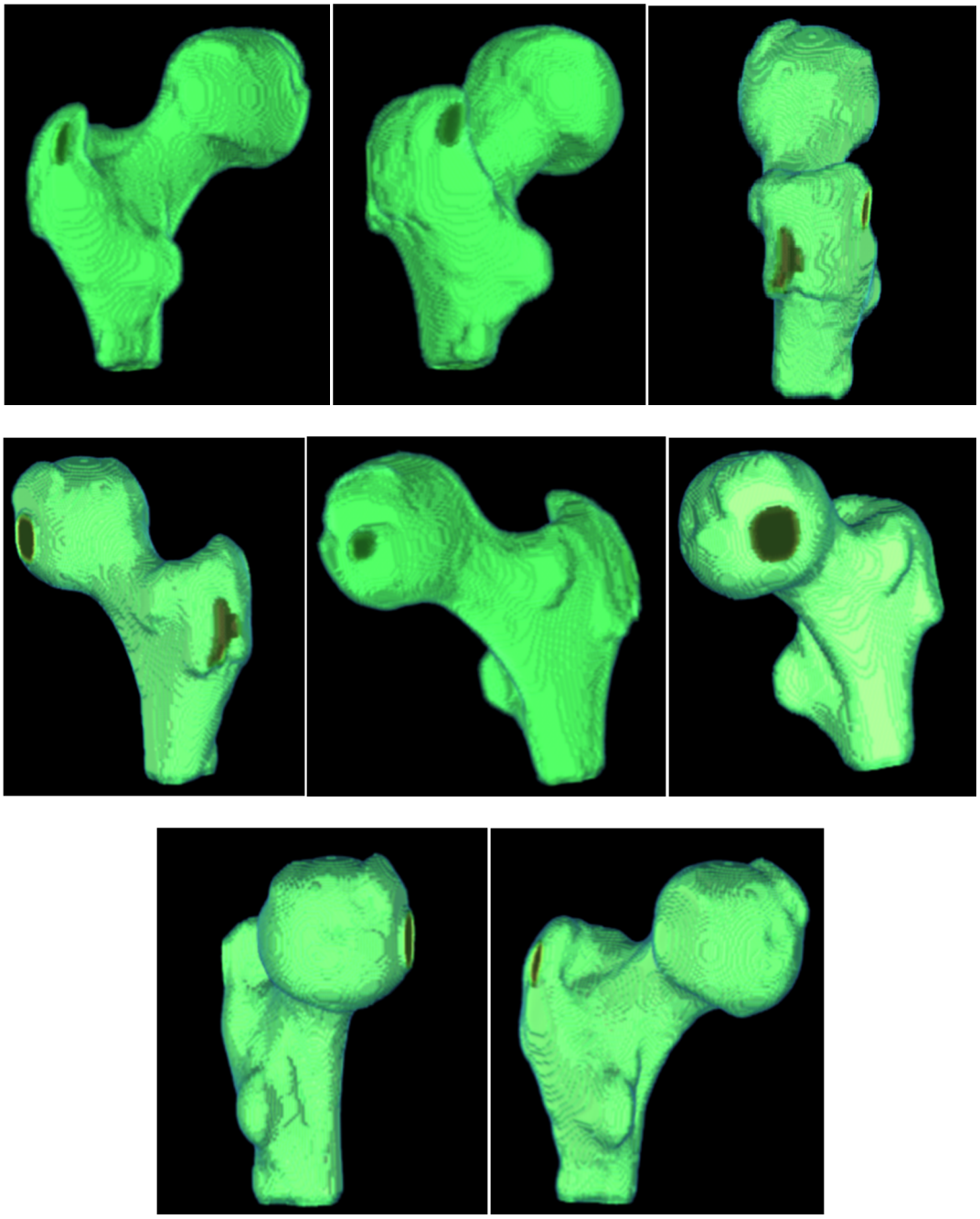

Figure 5.5.3D reconstruction of the Left femur(dataset 2)

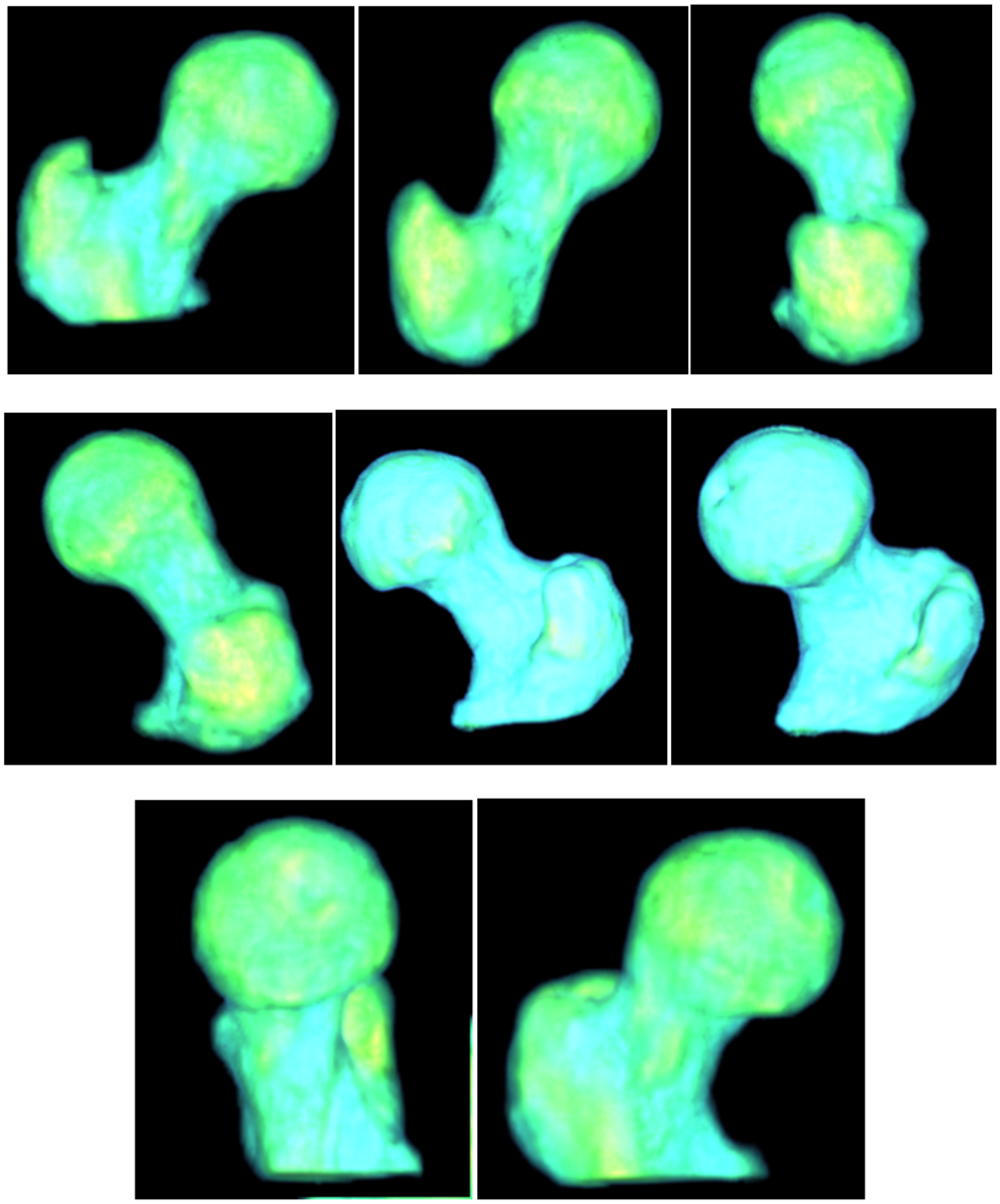

Figure 5.6.3D reconstruction of the right femur head (dataset 1)

Figure 5.7 Shows the three dimensional reconstruction of the pelvis from three different views.

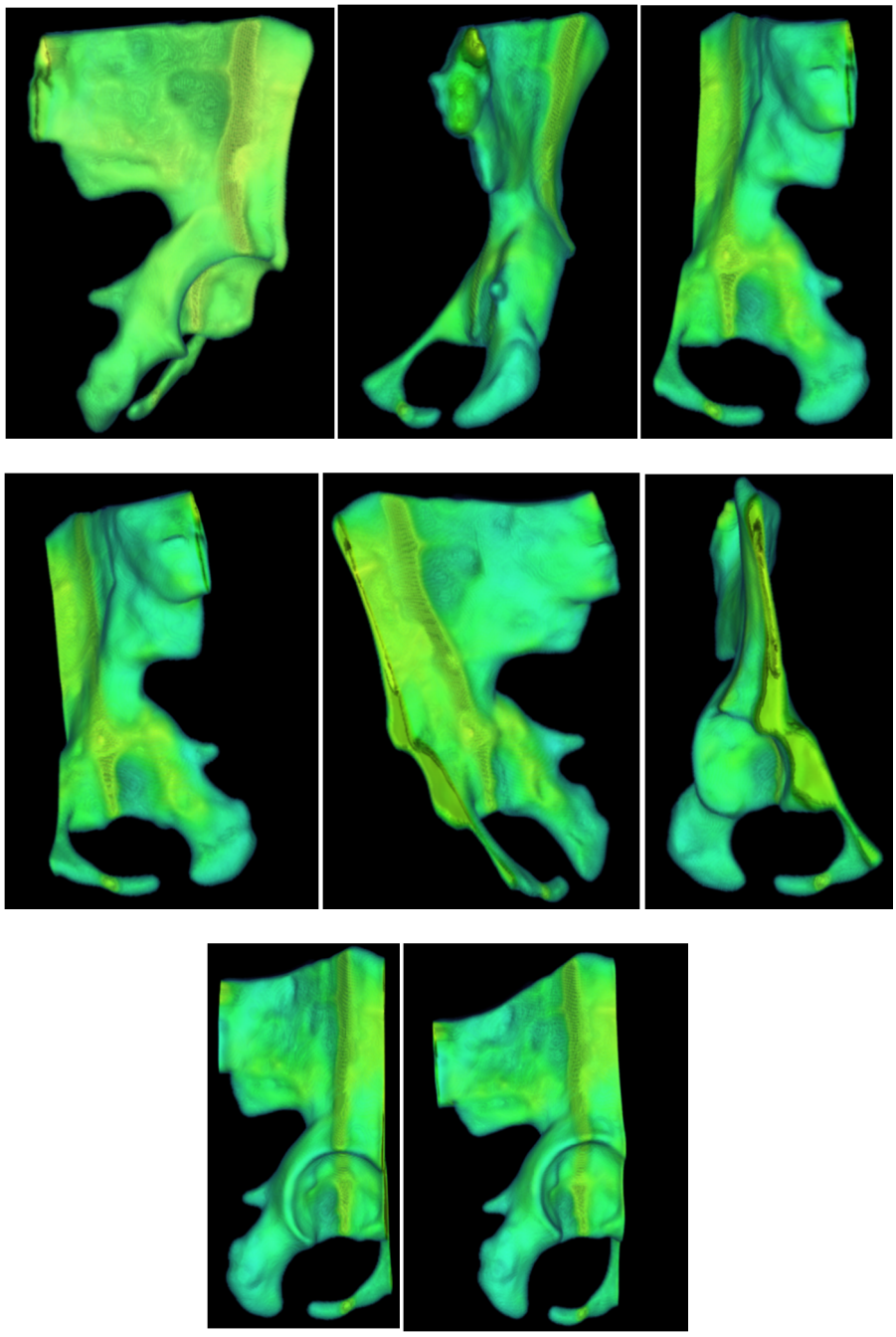

Figure 5.7.3D reconstruction of the pelvis (dataset 1)

The reconstruction of the Gluteus Minimus and Iliacus muscles are shown from different views in Figures 5.8 and 5.9 respectively.

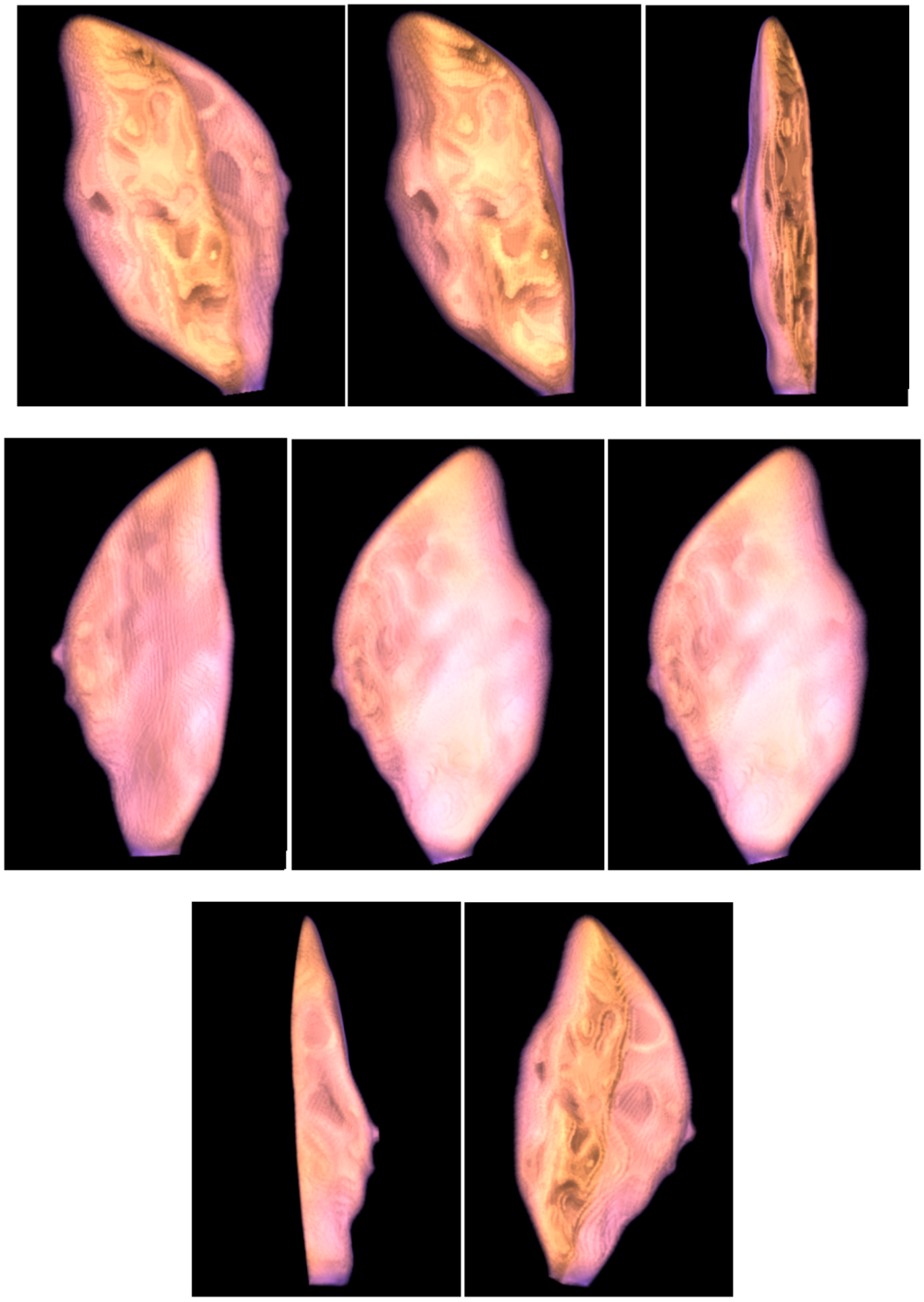

Figure 5.8.3D reconstruction of the Gluteus minimus muscle (dataset 1)

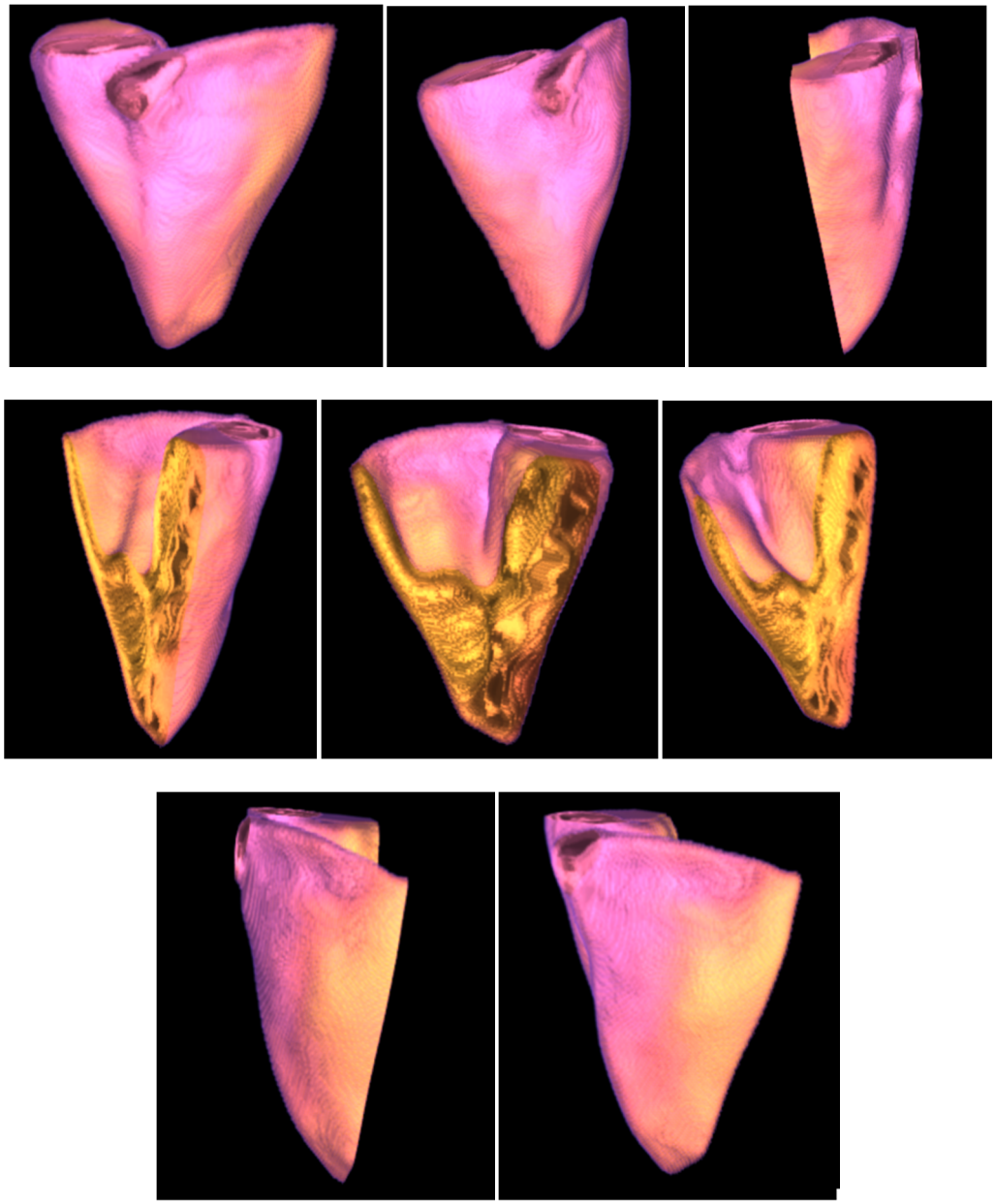

Figure 5.9. 3D reconstruction of the Iliacus muscle (dataset 1)

5.3 Evaluation and Validation

In this section the utilized evaluation methods and the validation results for the proposed method are explained and exhibited

5.3.1 Evaluation Methods

Because of the high rate of noise and intensity overlapping, neither the FCM nor the GSFCM and not even the semi-automatic segmentation methods like the watershed and active contour have acceptable segmentation results on our dataset (less than 70% accuracy). So, we decided to implement the method proposed by H. Kang et al. [129] and compare its results with our method. This method provides a framework for segmenting MRI data of thigh to spongy bone, cortical bone, muscle and fat using expert knowledge about the relative position of the tissues and FCM together. Because of the proven superiority of the GSFCM to FCM, we implemented this method with FCM (as it was proposed originally in the paper) and then this method is improved by using the GSFCM instead of the FCM method.

For the evaluation purposes, three testing datasets of the hip joint MRI data (totally containing 24,657,920 voxels) are prepared from the Ottawa general hospital and the results of segmentation are compared with the ground truth. The accuracy is defined as the ratio of the number of truly segmented voxels of a specific tissue to the total number of the voxels. Equation 5.1 shows the formula for calculating the segmentation accuracy of the target tissue.

$$\frac{\sum_{a=1}^{SL}\sum_{b=1}^{R}\sum_{c=1}^{CL} S(a,b,c) == G(a,b,c)}{SL \times R \times CL} \qquad (5.1)$$

Where SL is the number of slices,R is the number of rows, CL is the number of columns, *S* is the segmented image of the target tissue and *G* is the ground truth. Both *S* and *G* are the binary 3D images and ”==” shows the logical equality between the voxels.

For obtaining the ground truth the available datasets are segmented manually, using the instructions given by Dr. Kavan Rakhra, who is working as a radiology specialist at the Ottawa general hospital. Some of the points that have to be taken into account, when segmenting the MRI manually, are summarized here.

1- The placement of the organs in respect to each other based on the anatomical information should always be considered

2- Since MRI is a 3D data, when trying to segment one slice, it is important to take a look at the previous and next slices as well to detect the organs which are not clear enough in one slice but are clearer in successive slices.

3- Since there are some wide veins which are passing through the hip area and their intensity is same as the cortical bone at MRI, it is important, not to mistaken them with cortical bone. One point that could help in distinguishing them from cortical bone is this fact that the cortical bone is usually placed around the spongy bone.

4- When the cortical bone is connected to veins or ligaments, there's a possibility of missegmenting them, while preparing the ground truth. For avoiding this mistake, considering the shape of the bone and also inspecting the previous and next slices could be very helpful.

5- Considering all the necessary measures, there's always a possibility of 0.5% error in preparing the ground truth.

For a better evaluation of the segmentation results on the edges, the total false positive and negative are also calculated on the edges. These two metrics help us to evaluate if the error of the segmentation method on the edges is balanced between spongy bone and other tissues or not. For calculating the total false positive and negative on the edges, first, an area with the width of 10 pixels is chosen around the contour of the spongy bone in the ground truth, which is called the edge band. Figure 5.10 clarifies the method of choosing the edge band by choosing it around the edges of a square. Considering that The black area pixels outside and inside of the edge band are not considered for calculating the errors at the edge band image, it is clear that by using this method it is possible to calculate the error specifically around the edges and evaluate the efficiency of the proposed method at the correct segmentation of the edges. After choosing the edge band in the ground truth image the same area was mapped and chosen on every segmented image and the accuracy on the edges were calculated only on the chosen area at the segmented images. Total false positive and negative ratios also were calculated on the edge band of the spongy bone. Equations 5.2 and 5.3 are utilized for

calculating the total false positive and negative ratios on the edge band of the spongy bone respectively.

$$TFPR = \frac{FS_p(S)}{EA_p} \qquad (5.2)$$

$$T\,FNR = \frac{FS_p(NS)}{EA_p} \qquad (5.3)$$

where, TFPR is the total false positive ratio, TFNR is the total false negative ratio, $FS_p(S)$ is the number of pixels which are segmented wrongly as the spongy bone at the edge band, $FS_p(NS)$ is the number of pixels at the edge band, which are actually spongy bone but they are wrongly not segmented as the spongy bone and EA_p is the total number of pixels at the edge band of the spongy bone. The term total at TFPR and TFNR comes from this fact that the total number of pixels at the edge band is used at the denominator of both formulas.

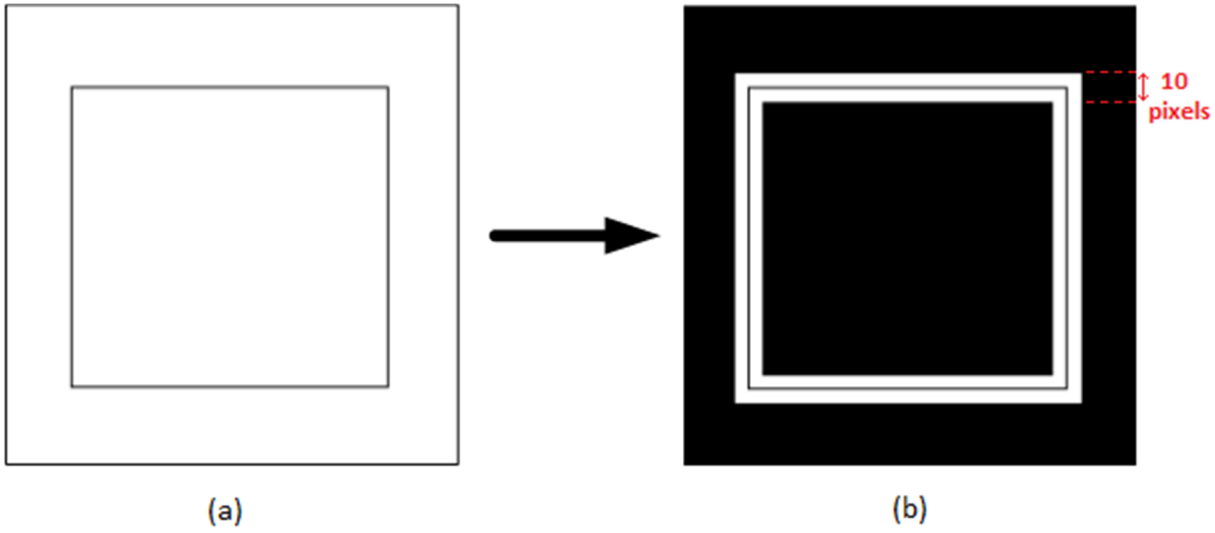

Figure 5.10. Creating the edge band image by choosing a 10 pixel width strip around the edges of a square (a) original image (b) edge band image

For clarifying the TFPR and TFNR, these two factors are calculated in figure 5.11 for the spongy bone. This figure shows a part of the spongy bone edge band. Gray, black, red and white pixels shows the spongy bone, cortical bone, muscle and adipose tissue respectively. Figure 5.11 (a) is the ground trough and (b) is the segmentation result.

The relation between the TFPR, TFNR and accuracy on the edges of the spongy bone are shown in equation 5.4

$$\text{Accuracy} = (1 - (\text{TFPR}+\text{TFNR})) \tag{5.4}$$

For evaluating the average participation time by the operator the program was run ten times with the purpose of segmenting two datasets containing 160 of 256*256 slices to the spongy bone, cortical bone, muscle and adipose tissue. Each time the total cooperation time by the operator is recorded and at the end the average cooperation time by the operator is calculated. For calculating the average participation time for the watershed and active contour methods, 50 slices are chosen from different parts of the datasets, watershed and active contour were applied on each of them separatelyfor segmenting the image to four tissues and the average operator participation time for one slide is calculated for each of the methods. Then, this average participation time (37 second for the watershed and 134 seconds for the active contour) is multiplied by 160 (the total number of slides at each dataset) to calculate the average operator participation time for the whole dataset.

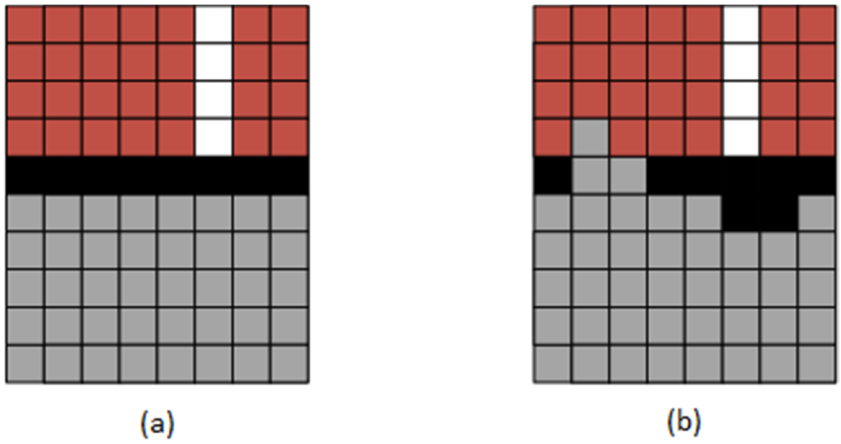

Figure 5.11.A part of the spongy bone edge band. Gray, black, red and white pixels shows the spongy bone, cortical bone, muscle and adipose tissue respectively. (a) ground trough (b) segmentation result. For the spongy bone TFPR = 3/80 = 3.7%, TFNR = 2/80 = 2.5%

For evaluating the accuracy and required time for segmenting the MRI to 4 tissues, by the proposed method the software was tested by using three different datasets and the operator participation was gotten only for the spongy bone segmentation. For calculating all the times the software was run on an Intel Core i7-3.5 GHz processor

5.3.2 Validation Results

In this section, the result of the segmentation using the proposed method is compared with some other available methods, which are used for MRI segmentation. First two semi-automatic segmentation methods (watershed and active contour) and an automatic method (FCM) are applied to two different MRI slices and then two heuristic methods, which are specifically designed for the MRI segmentation, are implemented based on the literature and applied to the same slices. The result of segmentation using the proposed method is finally shown in figure 5.13 (c). Figure 5.12 shows the results of the segmentation on two different slices using the watershed, active contour and FCM methods. The watershed method, which is used here, is the marker-controlled watershed with gradient as the segmentation criterion [159]. For applying the watershed algorithm the relative function in the Matlab image processing toolbox is utilized. As for the active contour the gradient vector fellow (GVF) [157] is used. The m file for the active contour was downloaded from http://www.mathworks.com/matlabcentral/fileexchange/28149-snake---active-contour and the spatial FCM method is implemented using [130].The segmentation results on the same slices using the method proposed by [129], the method proposed by [129] improved with GSFCM and the proposed methods are shown in Figure 5.13.For comparing the results of the proposed method and the method proposed by [129] on the edges, two close views from the extracted spongy bone at the femur's head and acetabulum meeting point is shown in Figure5.14. The edges of the femur's head, acetabulum and the Acetabular notch are clear in Figure5.14 (b). The results clearly show the superiority of the proposed method.

One of the motivations of this work was decreasing the participation time by the operator compare to other semi-automatic methods. For evaluating this in table 5.2 the average participation time at the proposed method is compared with the average participation time at the watershed and active contour. The methods for calculating the average participation time at each method is explained at Section 5.3.1.

The performance comparison results are shown in tables 5.4 to 5.6 for three available datasets. The results show the superiority of the proposed method in any case. However, the proposed method has even better results on the edges compare to the overall result. This is very important because the good extraction of the edges is an important factor in MRI segmentation and most of the available

segmentation methods have problem with this issue. The good performance of the framework on the edge clearly proves the efficiency of the newly proposed DKFCM method which is specifically designed for improving the segmentation quality on the edges.

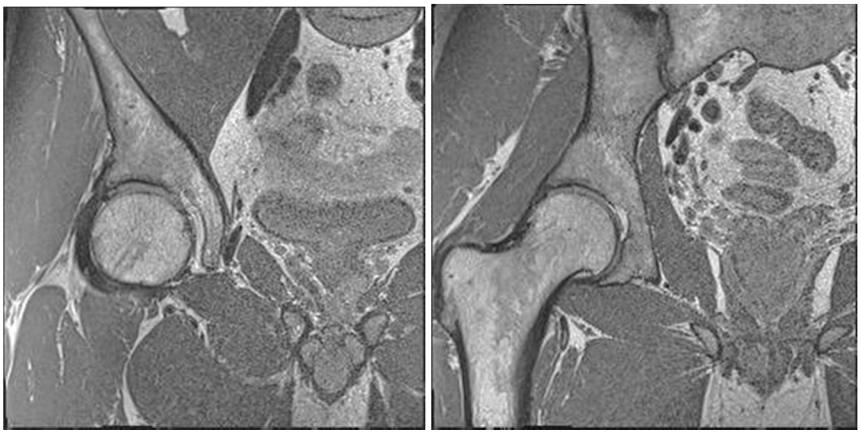

(a)

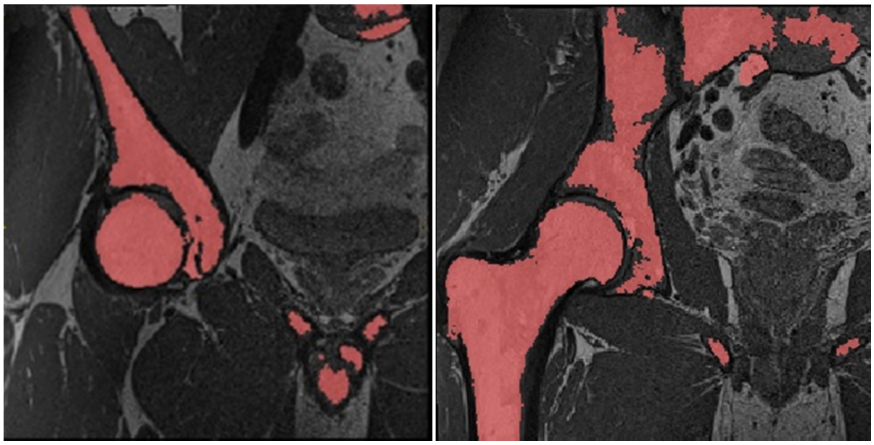

(b)

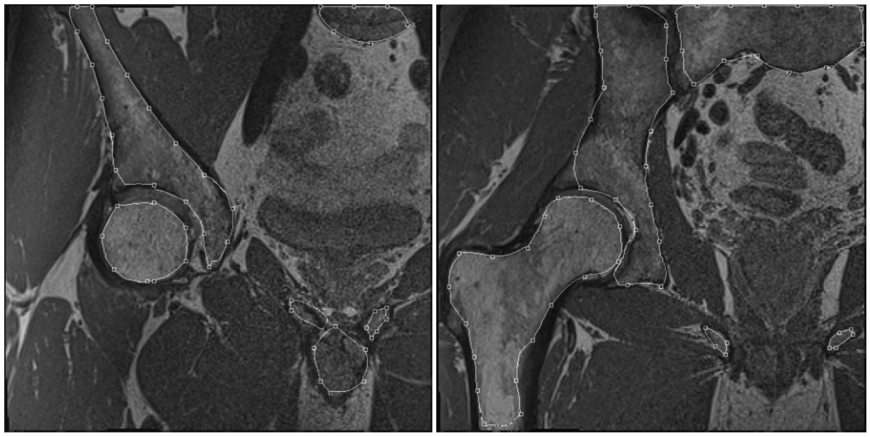

(c)

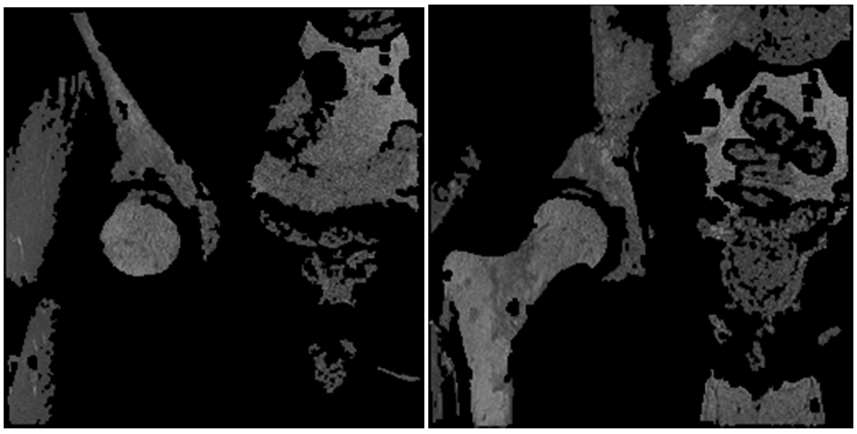

(d)

Figure 5.12. The results of segmentation of the spongy bone on two slices using three segmentation methods (a) Original MRI slices, (b) Watershed segmentation, (c) active contour segmentation (d) FCM segmentation

Table5.2. Comparing the average participation time by the operator in the proposed method with two other semi-automatic methods

Method	**Average participation time by the operator**	**Number of slices segmented by the participation**
Proposed method	43 seconds	160
Watershed	37 seconds	1
Active contour	134 seconds	1

Comparing the segmentation accuracy of the proposed method for three different datasets shows that the quality of the segmentation at dataset 3 is lower than two other datasets which is the result of lower number of slices and higher distance between them, which makes the process of transferring the segmentation to the next slice harder and less accurate.

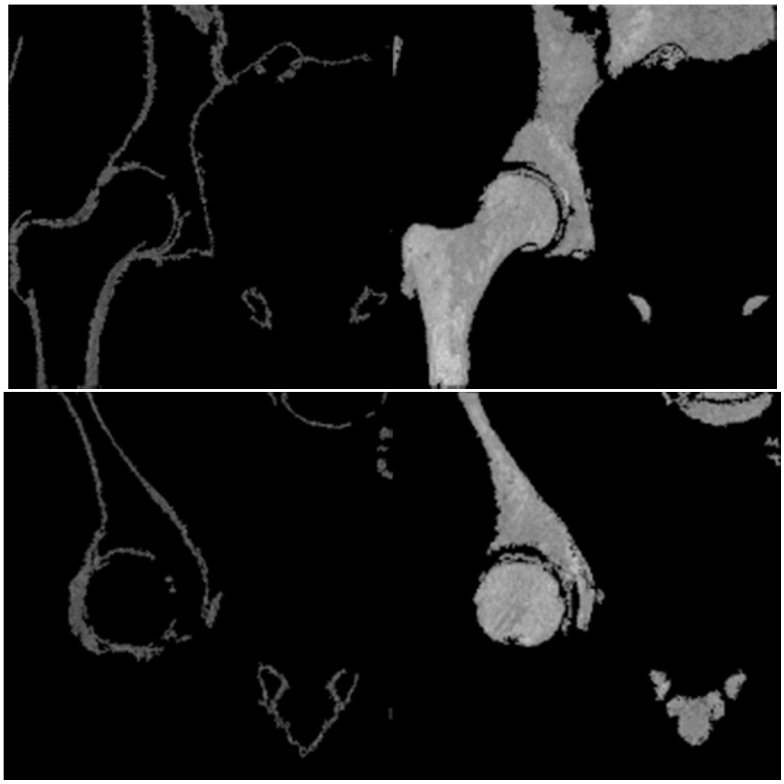

(a)

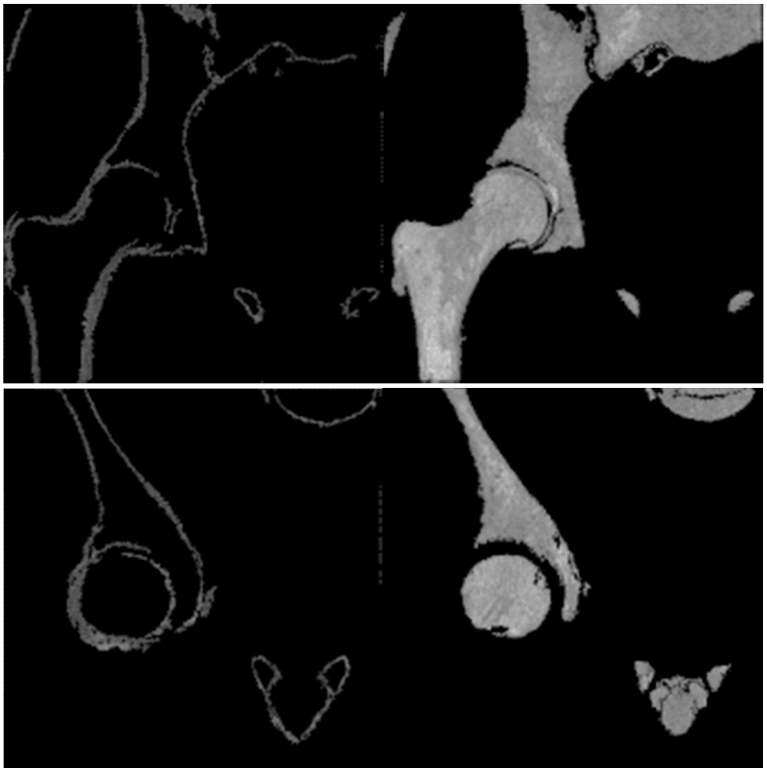

(b)

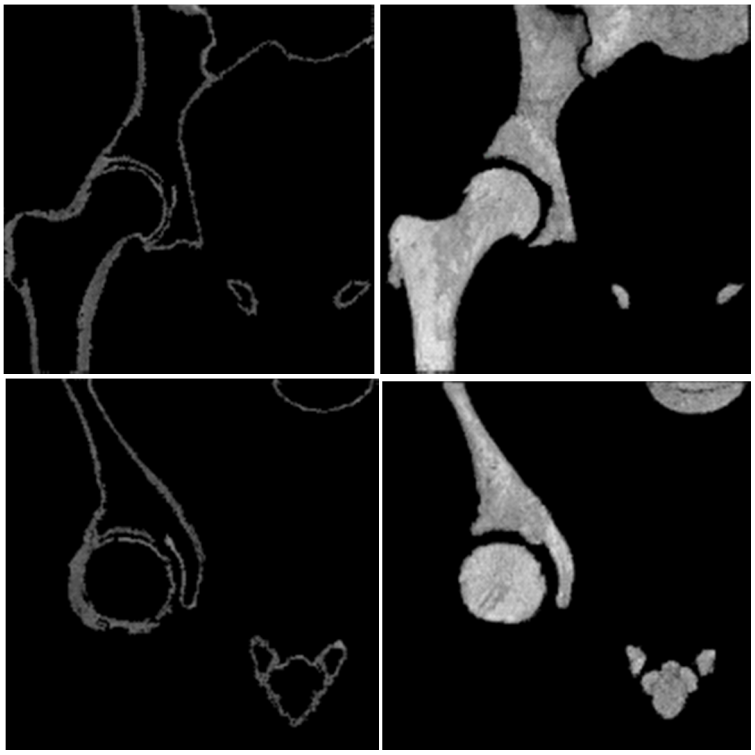

(c)

Figure 5.13. The results of segmentation to spongy bone and cortical bone on two slices (left images are the cortical bone and right images are the spongy bone (a) Ref [129], (b) Ref [129] improved by GSFCM, (c) The proposed framework (dataset 2)

For a better evaluation of the performance on the edges, the total false positive and negative rates are also calculated on the edge band. The method and equations for calculating the total false positive and negative on the edge band as well as the method for choosing the edge band are all explained in Section 5.3.1 (evaluation methods).

As shown in tables 5.3, the total false positive and negative are almost equal for the proposed method while for the method proposed by [129] the total false positive is very bigger, which indicates that relatively there are big portions of other tissue, which are missegmented as the spongy bone. This indicates the balance in segmentation at the proposed segmentation method compare to the two other methods. The big difference of the total false positive and negative ratios at the edge band between the other methods and the proposed method proves the superiority of the proposed method in segmenting the edges, which is resulted from the accurate bounding of the searching area to the edges of the target tissue at the proposed framework.

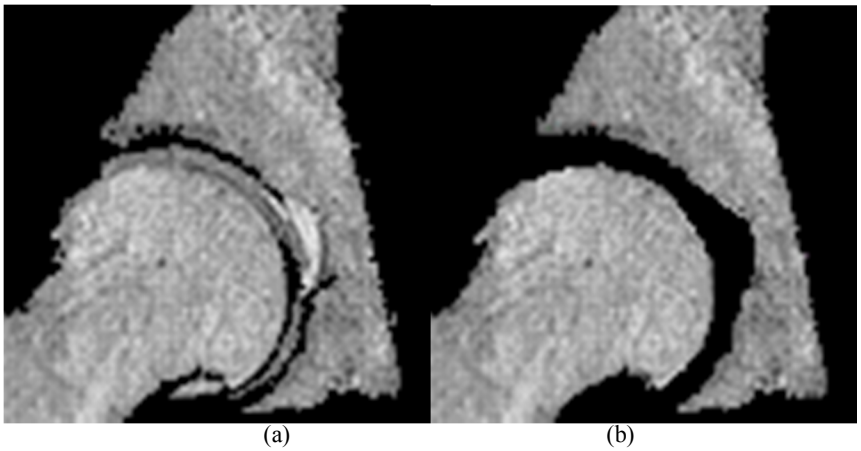

(a) (b)

Figure 5.14. Extracted spongy bone at the femur head and acetabulum meeting point by (a) Ref [129] improved by GSFCM, (b) The proposed framework (dataset 2)

Table 5.3. Comparing the total false positive and negative ratios of the spongy bone at the edge band of the spongy bone in the proposed framework with ref[129] and ref [129] improved with the GSFCM

Error Type	Ref [129]	Ref [129] with GSFCM	Proposed Method
TFPR	19.4%	18.2%	3.6%
TFNR	10.2%	8.7%	4.1%

Table5.4. Comparing the accuracy of segmentation in the proposed framework with Ref[129] and Ref [129] improved with the GSFCM (Dataset 1)

Region	Ref [129]	Ref [129] with GSFCM	Proposed Method
Spongy Bone	89.8%	92.5%	99.2%
Cortical Bone	68.2%	72.7%	92.3%
Muscle	90.1%	93.4%	99.4%
Adipose Tissue	74.6%	78.2%	95.2%
Edges (all tissues)	71.2%	71.8%	92.2%

Table5.5. Comparing the accuracy of segmentation in the proposed framework with Ref[129] and Ref [129] improved with the GSFCM (Dataset 2)

Region	Ref [129]	Ref [129] with GSFCM	Proposed Method
Spongy Bone	90.6%	92.3%	99.5%
Cortical Bone	68%	71.9%	93.1%
Muscle	91.2%	92.8%	99.3%
Adipose Tissue	76.8%	79.4%	94.9%
Edges (all tissues)	72.3%	72.3%	93.4%

Table5.6. Comparing the accuracy of segmentation in the proposed framework with Ref[129] and Ref [129] improved with the GSFCM (Dataset 3)

Region	Ref [129]	Ref [129] with GSFCM	Proposed Method
Spongy Bone	88.3%	91.7%	95.6%
Cortical Bone	66.8%	70.6%	84.7%
Muscle	89.8%	90.5%	94.3%
Adipose Tissue	73.1%	76.8%	88.6%
Edges (all tissues)	68.5%	69.6%	85.1%

The segmentation time for dataset 1, 2 and 3, the average segmentation time per voxel and the average cooperation time by the operator are all listed in table 5.5. Datasets 1, 2 and 3 consist of 10485760, 10485760 and 3686400 voxels respectively. Methods for calculating the times are all explained in Section 5.3.

Table5.7. Time evaluation of the proposed segmentation method

Segmentation time for dataset 1 (software)	495 seconds
Segmentation time for dataset 2 (software)	573 seconds
Segmentation time for dataset 3 (software)	173 seconds
average segmentation time per voxel (software)	53 μ seconds
Average operator participation time	43 seconds

CHAPTER 6

Conclusion and Future Work

A new framework for extracting the spongy bone, cortical bone, muscle and adipose tissue from MRI data is proposed. In this framework multiple heuristic methods are developed for improving the segmentation results compare to the available segmentation methods. This happened by finding the relational position of the tissues, getting the shortest and most effective contribution from the operator, forward and backward transfer of the accurate segmentation on the seed slice to other slices and improving the segmentation quality on the edges which is an important factor in MRI segmentation especially in some applications like detecting the Femoroacetabular impingement (FAI) and designing the implants. The DKFCM method, which is proposed in this thesis and used in the framework, resulted to an accurate segmentation of the tissues and demonstrates superiority over the previous works especially on the edges, which is the main shortcoming of the existing methods. The accuracy of this method on the edges demonstrates the superiority of this method to the available methods especially the model based methods which are not usually capable of giving an accurate segmentation on the edges.

Improving the segmentation result has been one the motivation of this thesis. For evaluating this improvement in the proposed method over the available segmentation methods, which has been used for segmenting the MRI, first, two semi-automatic and an automatic segmentation methods are chosen. Comparing the results of the segmentation by the proposed method with the ones by these three methods clearly shows the superiority of the proposed method in the segmentation. The reason for this superiority is simply because the other methods don't consider the necessary parameters needed for segmenting MRI and the parameters that they are using are not very effective for

segmenting the MRI because of the multiple types of problems on MRI data, which are explained in Chapter one. As an example the Watershed segmentation method uses the topographical parameters which are mainly relies on the gradient. While because of the IIH, PVE and noise it is hard to get enough information for an accurate segmentation from the gradient of MRI. The proposed method on the other hand is using a variety of parameters like the connection between the successive slices in MRI, the relative position of the organs acquired from expert knowledge and a 3D deformable kernel for improving the segmentation as much as possible. For evaluating the participation time by the operator, this time is also measured at the semi-automatic methods and compared with the one at the proposed method. Very small operator participation time at the proposed method compare to the other methods clearly proved the superiority of the proposed method in this case, which is an important factor in making the MRI segmentation more automated, more convenient and less costly. Then, the result of segmentation by two heuristic methods, which are specifically designed for the musculoskeletal segmentation of the MRI, is compared with the proposed method. The comparison shows that however the segmentation quality is better in these two methods but it is still by far less than the proposed method. The large improvement in the result of the total false positive and negative at the segmentation on the edge band by the proposed method over the other methods clearly shows the increasing in the quality of the segmentation on the edge bands, which is one of the motivations of this method. Experimental results of the segmentation and 3D modeling of different organs also have proved the ability of the proposed method in accurate segmentation of the MRI to four tissues (spongy bone, cortical bone, muscle and the adipose tissue) simultaneously.

The biggest problem for the proposed method happens when in some cases two different tissues with the same intensity are connected to each other and there's no visible edge between them. Figure 6.1 shows an example of this problem, happened at dataset number 2. As shown inside the white circle the cortical bone and vein which are connected together both have a same intensity range. In this condition the only feasible way is using expert knowledge about the shape of the organs. For solving this drawback, combining the proposed method with a model based segmentation method can be proposed which can benefit from both, expert knowledge which is embedded in the model and the accuracy of the proposed method on the edges.

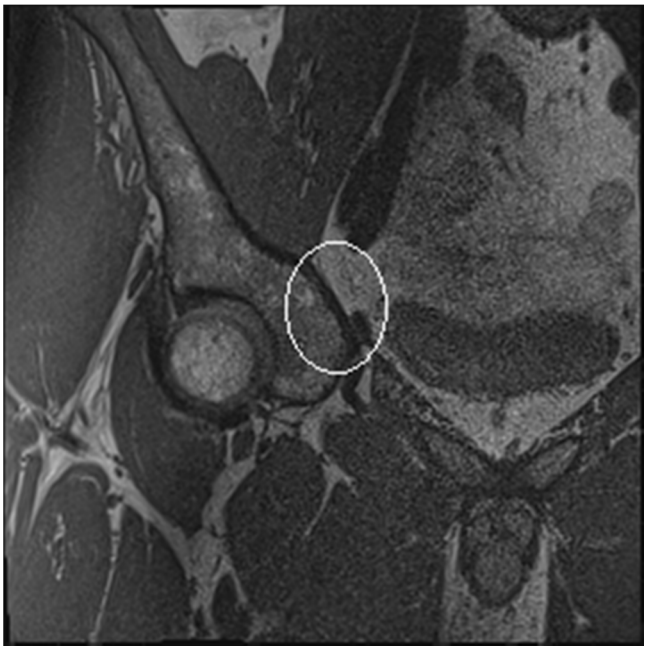

(a)

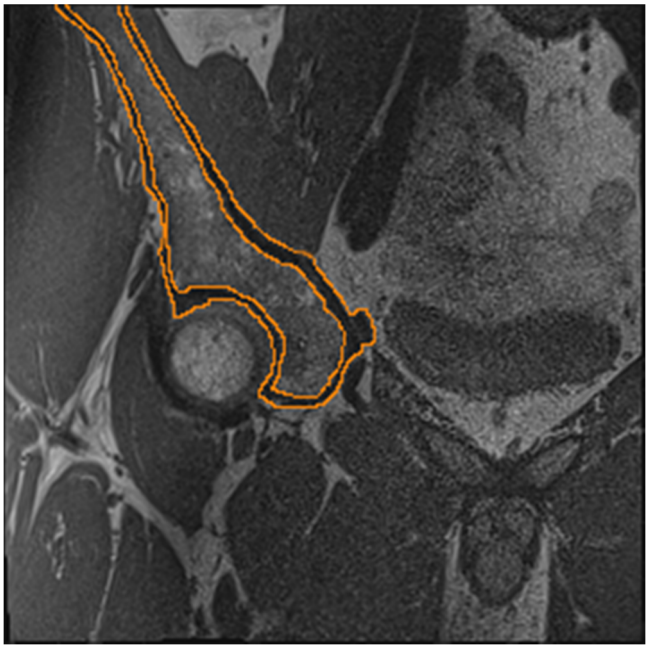

(b)

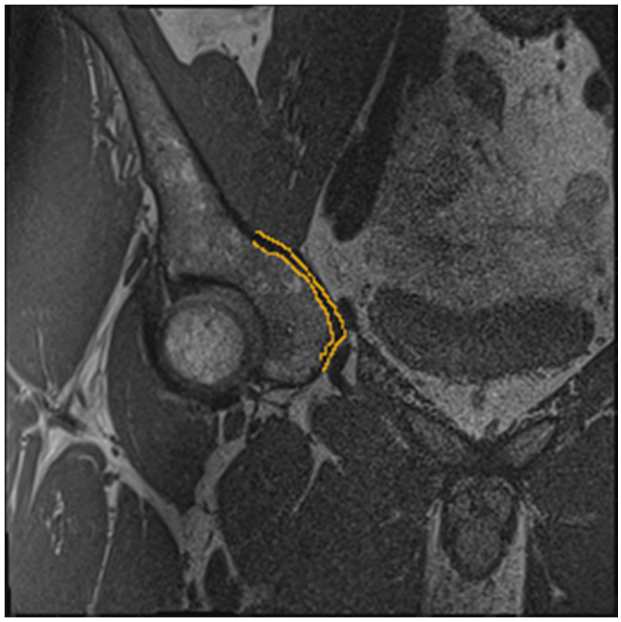

(c)

Figure 6.1 Sample of a segmentation mistake caused by another tissue with the same intensity as the cortical bone, which is connected to the bone (a) the original slice (white circle shows the problem making place) (b) result of the segmentation on the same slice. The target tissue is the cortical bone of the pelvis (dataset 2) (c) the correct segmentation at the problematic area

References

[1] https://www.dynapar.com/Products/Industry_Solutions/Medical_/_Life_Sciences/

[2] G. H. Glover, C. E. Hayes, N. J. Pelc, et al., "Comparison of linear and circular polarization for magnetic resonance imaging," Journal of Magnetic Resonance, vol. 64, no. 2, pp. 255–270, 1985.

[3] G. J. Barker, A. Simmons, S. R. Arridge, and P. S. Tofts, "A simple method for investigating the effects of non-uniformity of radiofrequency transmission and radiofrequency reception in MRI," British Journal of Radiology, vol. 71, no. 841, pp. 59–67, 1998.

[4] A. Simmons, P. S. Tofts, G. J. Barker, and S. R. Arridge, "Sources of intensity non-uniformity in spin echo images at 1.5T" Magnetic Resonance in Medicine, vol. 32, no. 1, pp. 121– 128, 1994.

[5] UrosVovk, FranjoPernu ˇ s, and Bo ˇ stjanLikar*, "A Review of Methods for Correction of Intensity" , IEEE TRANSACTIONS ON MEDICAL IMAGING, VOL. 26, NO. 3, MARCH 2007

[6] R. P. Velthuizen, J. J. Heine, A. B. Cantor, H. Lin, L. M. Fletcher, and L. P. Clarke, "Review and evaluation of MRI nonuniformity corrections for brain tumor response measurements," Med. Phys., vol. 25, pp 1655–1666, 1998.

[7] J. B. Arnold, J. S. Liow, K. A. Schaper, J. J. Stern, J. G. Sled, D. W. Shattuck, A. J. Worth, M. S. Cohen, R. M. Leahy, J. C. Mazziotta, and D. A. Rottenberg, "Qualitative and quantitative evaluation of six al gorithms for correcting intensity nonuniformity effects," Neuroimage, vol. 13, pp. 931–943, 2001.

[8] B. Belaroussi, J. Milles, S. Carme, Y. M. Zhu, and H. Benoit-Cattin, "Intensity non-uniformity correction in MRI: Existing methods and their validation," Med. Image Anal., vol. 10, pp. 234–246, 2006.

[9] http://321gomd.com/hip-flexability/

[10] http://teachmeanatomy.info

[11] http://roccoperez.files.wordpress.com/2012/09/femur.gif

[12]http://teachmeanatomy.info/wp-content/uploads/Anterior-Surface-of-the-Proximal-Portion-of-the-Femur-Bony-Landmarks.jpg

[13] Ganz R, Parvizi J, Beck M, et al. “Femoroacetabular impingement: a cause for osteoarthritis of the hip”ClinOrthopRelat Res 2003.

[14] Beck M, Kalhor M, Leunig M, et al. Hip morphology influences the pattern of damage to the acetabular cartilage. J Bone Joint Surg Br 2005, Vol. 87, No. 7.

[15] Hack K, Di Primio G, Rakhra K, et al. Prevalence of cam-type femoroacetabular impingement morphology in asymptomatic volunteers. J Bone Joint Surg Am 2010, Vol 92, No 4.

[16] Siebenrock KA, Wahab KH, Werlen S, et al. Abnormal extension of the femoral head epiphysis as a cause of cam impingement. Clin.Orthop.Relat. Res. 2004.

[17] Leunig M, Beck M, Kalhor M, et al. “Fibrocystic changes at anterosuperior femoral neck: prevalence in hips with femoroacetabular impingement” Radiology 2005; Vol. 236, No 1.

[18] Anderson LA. “Acetabular cartilage delamination in femoroacetabular impingement risk factors and magnetic resonance imaging diagnosis” J Bone Joint Surg. 2009; Vol. 91, No. 2.

[19] Gosvig KK, Jacobsen S, Sonne-Holm S, et al. “Prevalence of malformations of the hip joint and their relationship to sex, groin pain, and risk of osteoarthritis: a population-based survey” J Bone Joint Surg. 2010

[20] Ganz R, Leunig M, Leunig-Ganz K, et al. “The etiology of osteoarthritis of the hip”,Clin.Orthop. Related Restrictions 2008.

[21]M. Kass, A. Witkin and D. Terzopoulos “Snake: Active contour model”, Int .J.Computer, vol 1, pp.321-331, 1988

[22]Chen yang Xu, Jerry L. Prince “Snakes, Shapes and Gradient vector flow”, IEEE Transaction of Image Processing, Vol. 7, No.3, 1998

[23] Houda Bakir and Maher Charfi, “Automatic Medical Image Segmentation Based on EPGV-Snake,” IEEE Conference on 6th International Multi-Conference on Systems, Signal and Devices (SSD 09), IEEE Press, March 2009, pp.1-5, doi: 10.1109/SSD.2009.4956799.

[24] C. Xu and J.L. Prince, “Snakes, shapes, and gradient vector flow,” IEEE Trans. on Image Processing, vol. 7, March 1998, pp. 359-369, doi:10.1109/83.661186.

[25] Anthony Yezzi, Jr., Member, IEEE, Satyanad Kichenassamy, Arun Kumar, Peter Olver, and Allen Tannenbaum,* Member, IEEE, "A Geometric Snake Model for Segmentation of Medical Imagery", IEEE TRANSACTIONS ON MEDICAL IMAGING, VOL. 16, NO. 2, APRIL 1997

[26] M. Mancas and B. Gosselin, "Towards an automatic tumor segmentation using iterative watersheds," 2004.

[27] S. Salman and A. A. Bahrani, "Segmentation of tumor tissue in gray medical images using watershed transformation method," Computer Science and Applied Mathematics, vol. 2, no. 4, pp. 123-127, 2010.

[28] J. Yan, B. Zhao, L. Wang, A. Zelenetz and L. Schwartz, "Marker-controlled watershed for lymphoma segmentation in sequential CT images," Medical Physics, vol. 33, no. 7, pp. 2452-2460, 2006.

[29] S. Delest, R. Bone and H. Cardot, "Automatically computed markers for the 3D watershed segmentation," 2007.

[30] M. A. Gonzalez and V. Ballarin, "Automatic marker determination algorithm for watershed segmentation using clustering," Latin American applied research, vol. 39, no. 3, 2009.

[31] V. Grau, A. Mewes, M. Alcaniz, R. Kikinis and S. Warfield, "Improved watershed transform for medical image segmentation using prior information," IEEE Transactions on Medical Imaging, vol. 23, no. 4, pp. 447 - 458, 2004.

[32] K. Haris, S. Efstratiadis, N. Maglaveras and A. Katsaggelos, "Hybrid image segmentation using watersheds and fast region merging," IEEE Transactions on Image Processing, vol. 7, no. 12, pp. 1684 - 1699, 1998.

[33] R. Lapeer, A. Tan and A. Aldridge, "Active watersheds: combining 3D watershed segmentation and active contours to extract abdominal organs from MR images," 2002.

[34] Y. Huang and D. Chen, "Watershed segmentation for breast tumor in 2-D sonography," Ultrasound in Medicine & Biology, vol. 30, no. 5, p. 625–632, 2004.

[35] Mehryar Emambakhsh , Mohammad Hossein Sedaaghi, "Automatic MRI Brain Segmentation Using Local Features, Self-Organizing Maps, and Watershed ", 2009 IEEE International Conference

on Signal and Image Processing Applications

[36] Al Attar, M.A. ; Nile Univ., Cairo, Egypt ; Osman, N.F. ; Fahmy, A.S.,” Segmentation of left ventricle in cardiac MRI images using adaptive multi-seeded region growing, 2010 5th Cairo International Biomedical Engineering Conference Cairo, Egypt, December 16-18, 2010

[37] S. Park, J. H. Kim, S. Lee and K. K.G., "Comparative assessment of 3D region growing methods for lung airway segmentation : evaluation with pathological and normal cases," World Congress on Medical Physics and Biomedical Engineering, vol. 14, pp. 2525-2527, 2006.

[38] N. Mešanovic, M. Grgic, H. Huseinagic, M. Maleš, E. Skejic and M. Smajlovic, "Automatic CT image segmentation of the lungs with region growing algorithm," 2011.

[39] K. Chang, H. Zhang, S. Chen and L. Chen, "Automatic colon segmentation using Isolated-connected threshold,"2011.

[40] S. Sivaperumal and M. Sundhararajan, "Brain tumor analysis for MRI image segmentation using seaded region growing and PCNN," International Journal of Electronics, Communication & Instrumentation Engineering Research and Development (IJECIERD), vol. 3, no. 2, pp. 175-182, 2013.

[41] A. Aboaba, S. Hameed, O. Khalifa and A. Abdalla, "Computational hybrid level-set andregion growing techniques: a strategy for 3D fast segmentation of medical images," 2011

[42] E. Zanaty and A. Afifi, "A watershed approach for improving medical image segmentation," Journal of Computer Methods Biomechanical and Biomedical Engineering, 2012.

[43] A. EL Allaoui and M. Nasri, "Threshold optimization by genetic algorithm for segmentation of medical images by region growing," International Journal of Emerging Trends and Technology in Computer Science (IJETTCS), vol. 1, no. 2, pp. 161-166, 2012.

[44] L. Kantorovich, "A new method for solving some classes of extremal problems",Doklady AcadSci USSR, vol. 28, pp. 211-14, 1940.

[45] J. Orlin, "Max flows in O (nm) time or better", 2013.

[46] A. Goldberg and R. Tarjan, "A new approach to the maximum flow problem", 1986.

[47] L. Ford and D. Fulkerson, "Maximal flow through a network", Canadian Journal of Mathematics , vol. 8, p. 399–404, 1956.

[48] Y. Boykov and M. Jolly, "Interactive graph cuts for optimal boundary and region segmentation of objects in N-D images", 2001.

[49] V. Chen and S. Ruan, "Graph cut segmentation technique for MRI brain tumor extraction", Paris, 2010.

[50] I. Despotovic, I. Segers, L. Platisa, E. Vansteenkiste, A. Pizurica, K. Deblaere and W. Philips, "Automatic 3D graph cuts for brain cortex segmentation in patients with focal cortical dysplasia", Boston, 2011.

[51] Y. Boykov and G. Funka-Lea, "Graph cuts and efficient N-D image segmentation", International Journal of Computer Vision, vol. 70, no. 2, pp. 109-131, 2006.

[52] O. Veksler, "Star shape prior for graph-cut image segmentation", Marseille, 2008.

[53] G. Slabaugh and G. Unal, "Graph cuts segmentation using an elliptical shape prior", 2005.

[54] P. Das, O. Vekslera, V. Zavadsky and Y. Boykov, "Semiautomatic segmentation with compact shape prior", Image and Vision Computing, vol. 27, no. 1-2, pp. 206-219, 2009.

[55] D. Freedman and T. Zhang, "Interactive graph cut based segmentation with shape priors", 2005.

[56] D. Grosgeorgea, C. Petitjeana and S. Ruan, "Graph cut segmentation with a statistical shape model in cardiac MRI", Computer Vision and Image Understanding, vol. 117, no. 9, p. 1027–1035, 2013.

[57] Victor Chen, Su Ruan, “Graph cut segmentation technique for MRI brain tumor extraction”, 2010 IEEE

[58] Y. Nakagawa and A. Rosenfeld, "Some experiments on variable thresholding", Pattern Recognition, vol. 11, No. 3, pp. 191–204, 1979.

[59] J. Bernsen, "Dynamic thresholding of grey-level images",8th International Conference on Pattern Recognition, 1986.

[60] C. K. Chow and T. Kaneko, "Automatic boundary detection of the left ventricle from cineangiograms", Computers and Biomedical Research, vol. 16, no. 5, pp. 388-410, 1972.

[61] J. Zhang, C. Yan, C. Chui and S. Ong, "Fast segmentation of bone in CT images using 3D adaptive thresholding", Computers in Biology and Medicine, vol. 40, no. 2, pp. 231236, 2010.

[62] M. Moussallem, P. Valette, A. Traverse-Glehen, C. Houzard, C. Jegou and F. Giammarile, "New strategy for automatic tumor segmentation by adaptive thresholding on PET/CT images", Applied Clinical Medical Physics, vol. 13, no. 5, 2012.

[63] Norhashimah Mohd Saad1, S.A.R. Abu-Bakar2, Sobri Muda3, Musa Mokji, "Segmentation of Brain Lesions in Diffusion weighted MRI using Thresholding Technique", 2011 IEEE International Conference on Signal and Image Processing Applications (ICSIPA2011)

[64] N. Otsu, "A threshold selection method from gray-level histograms", IEEE Transactions on Systems, Man and Cybernetics, vol. 9, no. 1, pp. 62-66, 1979.

[65] P. Kalavathi, "Brain tissue segmentation in MR brain images using multiple Otsu's thresholding technique", 2013.

[66] M. Kass, A. Witkin and D. Terzopoulos, "Snakes: active contour models", International Journal of Computer Vision, vol. 1, no. 4, pp. 321-331, 1988.

[67] D. Terzopoulos and K. Fleischer, "Deformable models", The Visual Computer, vol. 4,pp. 306-331, 1988.

[68] R. Malladi, J. Sethian and B. Vemuri, "Shape modeling with front propagation: a level set approach", IEEE Transactions on Pattern Analysis and Machine Intelligence, vol. 17, no. 2, pp. 158 - 175, 1995.

[69] V. Caselles, R. Kimmel and G. Sapiro, "Geodesic active contours", International Journal of Computer Vision, vol. 22, no. 1, pp. 61 - 79, 1997.

[70] T. McInerney and D. Terzopoulos, "Deformable models in medical image analysis: a survey", Medical Image Analysis, vol. 1, no. 2, p. 91–108, 1996.

[71] S. Osher and N. Paragios, “Geometric level set methods in imaging”, vision, and graphics, 1st ed., Springer, 2003.

[72] K. Cheng, L. Gu, J. Wu, W. Li and J. Xu, "A novel level set based shape prior method for liver segmentation from MRI images", Medical Imaging and Augmented Reality, vol. 5128, pp. 150-159, 2008.

[73] E. Goceri, M. Unlu, C. Guzelis and O. Dicle, "An automatic level set based liver segmentation from MRI data sets", Istanbul, 2012.

[74] Z. Zhou, J. You, P. Heng and D. Xia, "Cardiac MR image segmentation and left ventricle surface reconstruction based on level set method", Studies in Health Technology and Informatics, vol. 111, pp. 629-632, 2005.

[75] K. Fritscher, R. Pilgram and R. Schubert, "Automatic cardiac 4D segmentation using level sets", in Functional Imaging and Modeling of the Heart, vol. 3504, Springer Berlin Heidelberg, 2005, pp. 113-122.

[76] S. Dakua and J. Sahambi, "A level set method for cardiac magnetic resonance image segmentation: an adaptive approach",Kharagpur, 2008.

[77] C. Baillard, P. Hellier and C. Barillot, "Segmentation of brain 3D MR images using level sets and dense registration", Medical Image Analysis, vol. 5, no. 3, p. 185–194, 2001.

[78] O. Colliot, T. Mansi, N. Bernasconi, V. Naessens, D. Klironomos and A. Bernasconi, "Segmentation of focal cortical dysplasia lesions on MRI using level set evolution", Neuro-Image, vol. 32, no. 4, p. 1621–1630, 2006.

[79] A. Bosnjak, G. Montilla, R. Villegas and I. Jara, "3D segmentation with an application of level set-method using MRI volumes for image guided surgery", Lyon, 2007.

[80] D. Rivest-Hénaultr and M. Cheriet, "Unsupervised MRI segmentation of brain tissues using a local linear model and level set", Magnetic Resonance Imaging, vol. 29, no. 2, p. 243–259, 2011.

[81] P. Radeva, J. Serrat and E. Marti, "A snake for model-based segmentation", 1995.

[82] J. Pardoa, D. Cabelloa and J. Herasb, "A snake for model-based segmentation of biomedical images", Pattern Recognition Letters, vol. 18, no. 14, p. 1529–1538, 1997.

[83] C. Chesnaud, P. Refregier and V. Boulet, "Statistical region snake-based segmentation adapted to different physical noise models", IEEE Transactions on Pattern Analysis and Machine Intelligence, vol. 21, no. 11, pp. 1145 - 1157, 1999.

[84] L. Ji and H. Yan, "Robust topology-adaptive snakes for image segmentation", Image and Vision Computing, vol. 20, no. 2, p. 147–164, 2002.

[85] S. Lama and C. Tong, "Enhanced snake algorithm by embedded domain transformation", Pattern Recognition, vol. 39, no. 9, p. 1566–1574, 2006.

[86] O. Colliot, O. Camara and I. Bloch, "Integration of fuzzy spatial relations in deformable models-application to brain MRI segmentation", Pattern Recognition, vol. 39, no. 8, p. 1401–1414, 2006.

[87] I. Dagher and K. El Tom, "Water Balloons: hybrid watershed balloon snake segmentation", Image and Vision Computing, vol. 26, no. 7, p. 905–912, 2008.

[88] Xenia Alb Rosa, M. Figueras, I. Ventura, Karim Lekadir, Alejandro F. Frangi,“conical deformable model for myocardial segmentation inlate-enhanced MRI”, ISBI 2012

[89] T. Cootes, G. Edwards and C. Taylor, "Active appearance models", Freiburg, 1998.

[90] T. Cootes, C. Taylor, D. Cooper and J. Graham, "Active shape models-their training and application", Computer Vision and Image Understanding, vol. 61, no. 1, p. 38–59, 1995.

[91] X. Zhuang, D. Hawkes, W. Crum, R. Boubertakh, S. Uribe, D. Atkinson, P. Batchelor, T. Schaeffter, R. Razavi and D. L. G. Hill, "Robust registration between cardiac MRIimages and atlas for segmentation propagation," San Diego, 2008.

[92] J. Ulén, P. Strandmark and F. Kahl, "Optimization for multi-region segmentation of cardiac MRI", in Statistical Atlases and Computational Models of the Heart, Imaging and Modelling Challenges, Springer Berlin Heidelberg, 2012, pp. 129-138.

[93] A. Gubern-Mérida, M. Kallenberg, R. Martí and N. Karssemeijer, "Multi-class probabilistic atlas-based segmentation method in breast MRI", in Pattern Recognition and Image Analysis, Springer Berlin Heidelberg, 2011, pp. 660-667.

[94] C. Ortiz and A. Martel, "Automatic atlas-based segmentation of the breast in MRI for 3D breast volume computation", Medical Physics, vol. 39, no. 10, pp. 5835-5848, 2012.

[95] S. Bourouis, K. Hamrouni and N. Betrouni, "Automatic MRI brain segmentation with combined atlas-based classification and level-set approach", in Image Analysis and Recognition, Springer Berlin Heidelberg, 2008, pp. 770-778.

[96] A. Fedorov, X. Li, K. Pohl, S. Bouix, M. Styner, M. Addicott, C. Wyatt, D. J.B., W. Wells and R. Kikinis, "Atlas-guided segmentation of vervet monkey brain MRI", The open neuroimaging journal, vol. 5, pp. 186-197, 2011.

[97] J. Morin, C. Desrosiers and L. Duong, "Atlas-based segmentation of brain magnetic resonance imaging using random walks", 2012.

[98] J. Stanier, I. Bloch and M. Goldberg, "Segmentation schemes for knowledge-basedconstruction of individual atlases from slice-type medical images", Newport Beach, 1993.

[99] X. Zhoua, T. Kitagawaa, K. Okuoa, T. Haraa, H. Fujitaa, R. Yokoyamab, M. Kanematsub and H. Hoshib, "Construction of a probabilistic atlas for automated liver segmentation in non-contrast torso CT images", International Congress Series, vol. 1281, p. 1169–1174, 2005.

[100] O. Commowick, V. Grégoire and G. Malandain, "Atlas-based delineation of lymph node levels in head and neck computed tomography images", Radiotherapy and Oncology, Journal of the European Society for Radiotherapy and Oncology, vol. 87, no. 2, pp. 281-289, 2008.

[101] F. Shi, P. Yap, Y. Fan, J. Gilmore, W. Lin and D. Shen, "Construction of multi region multi-reference Atlases for neonatal brain MRI segmentation", NeuroImage,vol.51, no. 2,pp.684-693,2010.

[102] B. Zitová and J. Flusser, "Image registration methods: a survey", Image and Vision Computing, vol. 21, no. 11, p. 977–1000, 2003.

[103] N. Alpert, D. Berdichevsky, Z. Levin, E. Morris and A. Fischman, "Improved methods for image registration", Neuro Image, vol. 3, no. 1, pp. 10-18, 1996.

[104] J. Maintz and M. Viergever, "A survey of medical image registration", Medical Image Analysis, vol. 2, no. 1, pp. 1-36, 1998.

[105] Yongxin Zhou and Jing Bai*, “Atlas-Based Fuzzy Connectedness Segmentation and Intensity Non-uniformity Correction Applied to Brain MRI", IEEE TRANSACTIONS ON BIOMEDICAL ENGINEERING, VOL. 54, NO. 1, JANUARY 2007

[106] M. Ahmed, S. Yamany, N. Mohamed, A. Farag and T. Moriarty, "A modified fuzzy c-means algorithm for bias field estimation and segmentation of MRI data", IEEE Transactions on Medical Imaging, vol. 21, no. 3, pp. 193-199, 2002.

[107] K. Chuang, H. Tzeng, S. Chen, J. Wu and T. Chen, "Fuzzy C-means clustering with spatial information for image segmentation", Computerized Medical Imaging and Graphics, vol. 30, no. 1, pp. 9-15, 2006.

[108] P. Vasuda and S. Satheesh, "Improved fuzzy C-means algorithm for MR brain image segmentation", International Journal on Computer Science and Engineering (IJCSE), vol. 2, no. 5, pp. 1713-1715, 2010.

[109] N. Abdul Khalid, S. Ibrahim and P. Haniff, "MRI brain abnormalities segmentation using K-Nearest Neighbors (k-NN)", International Journal on Computer Science and Engineering (IJCSE), vol. 3, no. 2, pp. 980-990, 2011.

[110]S. Dalmiya, A. Dasgupta and S. KantiDatta, "Application of Wavelet based K-means Algorithm in Mammogram Segmentation", International Journal of Computer Applications, vol. 52, no. 15, pp. 15-19, 2012.

[111] X. Zhang, C. Zhang, W. Tang and Z. Wei, "Medical image segmentation using improved FCM", Science China Information Sciences, vol. 55, no. 5, pp. 1052-1061, 2012.

[112] A. Jain, M. Murty and P. Flynn, "Data clustering: a review", ACM Computing Surveys(CSUR), vol. 31, no. 3, pp. 264-323, 1999.

[113] P. Vijayalakshmi, K. Selvamani and M. Geetha, "Segmentation of brain MRI using Kmeans Clustering algorithm", International Journal Of Engineering Trends and Technology,pp.113-115,2011.

[114] K. Somasundaram, S. Vijayalakshmi and T. Kalaiselvi, "Segmentation of brain MRI using K-means clustering algorithm", International Journal of Computational Intelligence and Informatics, vol. 1, no. 1, pp. 75-79, 2011.

[115]J. C. Bezdek, “Pattern Recognition with Fuzzy Objective Function algorithms”, Plenum Press, 1981.

[116] D. Pham and J. Prince, "An adaptive fuzzy C-means algorithm for image segmentation in the presence of intensity inhomogeneities", Pattern Recognition Letters, vol. 20, no. 1, pp. 57-68, 1999.

[117] D. Wankai, X. Wei, P. Chao and L. Jianguo, "MRI brain tumor segmentation based on improved fuzzy c-means method",Proc SPIE, 2009.

[118] M. Shasidhar, V. Raja and B. Kumar, "MRI brain image segmentation using modified fuzzy C-means clustering algorithm",Katra, Jammu, 2011.

[119] A. Dasgupta, "Demarcation of brain tumor using modified fuzzy C-means", International Journal of Engineering Research and Applications, vol. 2, no. 4, pp. 529-533, 2012.

[120] M. Ahmed, S. Yamany, N. Mohamed, A. Farag and T. Moriarty, "A modified fuzzy c- means algorithm for bias field estimation and segmentation of MRI data”, IEEE Transactions on Medical Imaging, vol. 21, no. 3, pp. 193-199, 2002.

[121] S. Kannan, S. Ramathilagam and R. Pandiyarajan, "Modified bias field fuzzy C-means for effective segmentation of brain MRI", in Transactions on Computational Science VIII, Springer Berlin Heidelberg, 2011, pp. 127-145.

[122] Y. Li and G. Li, "Fast fuzzy C-Means clustering algorithm with spatial constraints for image segmentation”, in Advances in Neural Network Research and Applications, Springer Berlin Heidelberg, 2010, pp. 431-438.

[123] R. Krishnapuram and J. Keller, "The possibilistic C-Means algorithm: insights and recommendations", IEEE Transactions on Fuzzy Sytems, vol. 4, no. 3, pp. 385-393, 1996.

[124] A. Rajendran and R. Dhanasekaran, "Enhanced possibilistic fuzzy C-means algorithm for normal and pathological brain tissue segmentation on magnetic resonance brain image",Arabian Journal for Science and Engineering, vol. 38, no. 9, pp. 2375-2388, 2013.

[125] M. Al-Zoubi, A. Hudaib and B. Al-Shboul, "A fast fuzzy clustering algorithm" International Conference on Artificial Intelligence, Knowledge Engineering and Data Bases, vol. 6, pp. 28-32, 2007.

[126] Ping Wang , A modified FCM algorithm for MRI brain image segmentation, 2008 International Seminar on Future Biomedical Information Engineering

[127] Joachim Pfeil, Werner E.Siebert, "Minimally Invasive Surgery in Total Hip Arthroplasty", ISBN 978-3-642-00897-9, Springer 2010.

[128] Blemker S. Asakawa, D. Asakawa, G. Gold, S. Delp,"Image-based musculoskeletal modeling: applications, advances, and future opportunities", Journal of Magnetic Resonance Imaging, pp. 441–451, 2007.

[129] H. Kang, A. Pinti, L. Vermeiren, A. Taleb Ahmed, X. Zeng, "Tissue classification for MRI of thigh using a modified FCM method", Proceedings of the 29th Annual International Conference of the IEEE pp. 5579- 5584, 2007

[130] Huynh Van Lung, Jong-Myon Kim, "A Generalized Spatial Fuzzy C-Means Algorithm for Medical Image Segmentation", proceedings of the FUZZ-IEEE, pp. 409- 414. 2009

[131] Zhimin WANG, Qing SONG, Yeng Chai SOH and Kang SIM, "A Robust Information Fuzzy Clustering Algorithm for Medical Image Segmentation", IEEE International Conference on Granular Computing, pp. 509-514, 2010

[132] Benjamin Gilles, Nadia Magnenat-Thalmann, "Musculoskeletal MRI segmentation using multi-resolution simplex meshes with medial representations", Medical Image Analysis, vol. 14, pp. 291–302, 2010

[133] Pierre Dodin, Jean-Pierre Pelletier, Johanne Martel-Pelletier, and Francois Abram, " Automatic Human Knee Cartilage Segmentation From 3-D Magnetic Resonance Images", IEEE Transactions on Biomedical Engineering, Vol. 57, No. 11, pp.2699-2711, November 2010

[134] Salma Essafi, G. Langs, J-F. Deux, A. Rahmouni, G. Bassez, N. Paragios, "Wavelet-driven knowledge-based mri calf muscle segmentation", IEEE International Symposium on Biomedical Imaging: From Nano to Macro, pp. 225-228, 2009.

[135] Shan Shen, William Sandham, Malcolm Granat, and Annette Sterr, " MRI Fuzzy Segmentation of Brain Tissue Using Neighborhood Attraction With Neural-Network Optimization", IEEE Transactions On Information Technology In Biomedicine, vol. 9, no. 3, pp. 459-467, Sep. 2005

[136] Tao Song, Mo M. Jamshidi, Roland R. Lee, and Mingxiong Huang, "A Modified Probabilistic Neural Network for Partial Volume Segmentation in Brain MR Image", IEEE Transactions On Neural Networks, vol. 18, no. 5, pp. 1424-1432, Sep. 2007

[137] Sufyan Y. Ababneh, Metin N. Gurcan, "An Automated Content-Based Segmentation Framework: Application to MR Images of Knee for Osteoarthritis Research", IEEE International Conference on Electro/Information Technology (EIT), pp. 1-4, 2010

[138] http://www.hss.edu/hip-pain-center-hip-conditions.asp

[139] Xu, N. ; Bansal, R. ; Ahuja, N. , "Object Segmentation Using Graph Cuts Based Active Contours", Proceedings. 2003 IEEE Computer Society Conference on Computer Vision and Pattern Recognition, pp. 46-53, 2003.

[140] D.Judehemanthl, D.Selvathi and J.Anitha, "Effective Fuzzy Clustering Algorithm for Abnormal MR Brain ImageSegmentation", 2009 IEEE International Advance Computing Conference (IACC 2009)

[141] Jim X. Chen, Harry Wechsler, J. Mark Pullen, Ying Zhu, and Edward B. MacMahon "Knee Surgery Assistance: Patient Model Construction, Motion Simulation, and Biomechanical Visualization", IEEE Transactions On Biomedical Engineering, vol. 48, no. 9, pp. 1042–1052, Sep. 2001.

[142] http://science.howstuffworks.com/mri.htm

[143] http://www.pudendalhope.info

[144] http://gmch.gov.in/e-study/e%20lectures/Anatomy/Gluteal%20region.pdf

[145] M. Taherdangkoo, M. Yazdi, and M. H. Rezvani, " Segmentation of MR Brain Images Using FCM improved by Artificial Bee Colony (ABC) Algorithm", IEEE International Conference on Information Technology and Applications in Biomedicine, pp. 1-5, 2010.

[146] Maureen Zimmerman, Beth Snow, ”An Introduction to Nutrition” v. 1.0, Chapter 9, Lardbucket, December 2012

[147] M. Karnan1, N. Nandha Gopal, "Hybrid Markov Random Field with Parallel Ant Colony Optimization and Fuzzy C Means for MRI Brain Image segmentation", IEEE International Conference on Computational Intelligence and Computing Research, pp. 1-4, 2010.

[148] Jin Liu, Tuan D. Pham, Wei Wen, Perminder S. Sachdev, " Spatially Constrained Fuzzy Hyper-Prototype Clustering with Application to Brain Tissue Segmentation", Proc. IEEE Int. Conf. on Bioinformatics and Biomedicine, pp. 397- 400, 2010.

[149] Albert Huang, Rafeef Abugharbieh, Roger Tam, " A Hybrid Geometric–Statistical Deformable Model for Automated 3-D Segmentation in Brain MRI", IEEE Transactions On Biomedical Engineering, vol. 56, no. 7, pp. 1838-1848, July 2009.

[150] Lara C.V. Harrison, Riku Nikander, MinnaSikio, Tiina Luukkaala, Mika T. Helminen, Pertti Ryymin, Seppo Soimakallio, Hannu J. Eskola, PrasunDastidar and HarriSievanen, "MRI Texture Analysis of Femoral Neck: Detection of Exercise Load-Associated Differences in Trabecular Bone", Journal Of Magnetic Resonance Imaging vol. 34, pp.1359–1366, 2011.

[151] Christopher M. Larson, " Pincer-Type Femoroacetabular Impingement", Operative Techniques in Sports Medicine, vol. 20, pp. 273-280, 2012.

[152] Seyed Mehdi Moghadas, Won-Sook Lee, “A 3D segmentation framework for an accurate extraction of the spongy and cortical bones from the MRI data”, IEEE international conference in bioinformatics and biomedicine, BIBM 2013.

[153] Thomas Sangild Sørensen, Gerald Franz Greil, Ole Kromann Hansen, Jesper Mosegaard,“Surgical simulation – a new tool to evaluate surgical incisions in congenital heart disease”, Journal of Interactive Cardio Vascular and Thoracic Surgery, vol. 5, pp 536-539, 2006.

[154] Dr. Ingeborg van kroonenburgh, Ing. Maikelbeerens, Ing. Carsten engel, Dr. Ir. Peter mercelis, Ivo lambrichts, Jules poukens, “Doctor and engineer creating the future for 3D printed custom implants”, Journal of digital dental news, April 2012.

[155] Christian N. Anderson, Geoffrey M. Riley, Gary E. Gold, Marc R. Safran, “Hip-Femoral Acetabular Impingement”, Clin Sport Med, 2013

[156] Miguel Ángel González Ballester, , Andrew P. Zisserman, Michael Brady “Estimation of the partial volume effect in MRI” Medical Image Analysis, Volume 6, Issue 4, Elsevier, December 2002, Pages 389–405

[157] C. Xu and J.L. Prince, "Gradient Vector Flow Deformable Models", Handbook of Medical Imaging, edited by Isaac Bankman, Academic Press, September 2000.

[158] W. Huda & R. Slone. “Review of Radiologic Physics, 2nd edition”, Lippincott Williams &Wilkins. 2003. Chapter 12 – MagneticResonance

[159] http://www.mathworks.com/help/images/examples/marker-controlled-watershed-segmentation.html?refresh=true

[160] Jerome Schmid and Nadia Magnenat-Thalmann, “MRI Bone Segmentation Using Deformable Models and Shape Priors”, 11th International Conference in Medical Image Computing and Computer-Assisted Intervention (MICCAI) 2008.